AN INVESTIGATION OF THE ROLE OF SHORT WAVES AND WIND DRIFT IN THE ...
BANNER, MICHAEL LESLIE
ProQuest Dissertations and Theses; 1973; ProQuest Dissertations & Theses Global

INFORMATION TO USERS

This material was produced from a microfilm copy of the original document. While the most advanced technological means to photograph and reproduce this document have been used, the quality is heavily dependent upon the quality of the original submitted.

The following explanation of techniques is provided to help you understand markings or patterns which may appear on this reproduction.

1. The sign or "target" for pages apparently lacking from the document photographed is "Missing Page(s)". If it was possible to obtain the missing page(s) or section, they are spliced into the film along with adjacent pages. This may have necessitated cutting thru an image and duplicating adjacent pages to insure you complete continuity.

2. When an image on the film is obliterated with a large round black mark, it is an indication that the photographer suspected that the copy may have moved during exposure and thus cause a blurred image. You will find a good image of the page in the adjacent frame.

3. When a map, drawing or chart, etc., was part of the material being photographed the photographer followed a definite method in "sectioning" the material. It is customary to begin photoing at the upper left hand corner of a large sheet and to continue photoing from left to right in equal sections with a small overlap. If necessary, sectioning is continued again — beginning below the first row and continuing on until complete.

4. The majority of users indicate that the textual content is of greatest value, however, a somewhat higher quality reproduction could be made from "photographs" if essential to the understanding of the dissertation. Silver prints of "photographs" may be ordered at additional charge by writing the Order Department, giving the catalog number, title, author and specific pages you wish reproduced.

5. PLEASE NOTE: Some pages may have indistinct print. Filmed as received.

Xerox University Microfilms
300 North Zeeb Road
Ann Arbor, Michigan 48106

Reproduced with permission of the copyright owner. Further reproduction prohibited without permission.

76-11,201

BANNER, Michael Leslie, 1945-
AN INVESTIGATION OF THE ROLE OF SHORT WAVES AND WIND DRIFT IN THE INTERACTION BETWEEN WIND AND LONG GRAVITY WAVES.

The Johns Hopkins University
Ph.D., 1973
Physical Oceanography

Xerox University Microfilms, Ann Arbor, Michigan 48106

© 1976

MICHAEL LESLIE BANNER

ALL RIGHTS RESERVED

THIS DISSERTATION HAS BEEN MICROFILMED EXACTLY AS RECEIVED.

Reproduced with permission of the copyright owner. Further reproduction prohibited without permission.

AN INVESTIGATION OF THE ROLE OF SHORT WAVES AND WIND DRIFT IN THE INTERACTION BETWEEN WIND AND LONG GRAVITY WAVES

by

Michael L. Banner II

A dissertation submitted to The Johns Hopkins University in conformity with the requirements for the degree of Doctor Of Philosophy.

Baltimore, Maryland

1973

Reproduced with permission of the copyright owner. Further reproduction prohibited without permission.

5/9/78 cs

ABSTRACT

Recent theoretical and experimental investigations have been concerned with the role of short gravity waves and ripples in the coupling between wind and long gravity waves in an effort to determine whether the concomitant occurrence of the small-scale waves is intrumental in the wave generation of long gravity waves.

The present investigation is a combined observational, experimental and theoretical examination of the role of small-scale waves and wind-drift riding on longer gravity waves. The experiments were carried out in a laboratory wind-wave tank. The wind tunnel fan speed was held constant, providing a mean windspeed at the center of the air channel of about 6 m/s. The mechanical wavemaker frequency was also held constant at 1.7 Hz and its stroke was incremented to provide carrier wave slopes (ak) of 0.00, 0.03, 0.06, 0.17 and 0.28. The characteristics of the short wave structure were documented photographically. Measurements were made of the mean wind profile and streamwise pressure gradient and of the wave amplitude at three fetches. The wave amplitude data was processed in the time and frequency domains using phase-averaging and Fourier analysis.

Beyond a certain steepness, the carrier waves were observed to undergo a limiting process not previously described. This is best characterized as a rolling of the crest towards a stagnation point relative to the moving wave. The stagnation point was consistently observed ahead of the crest.

Reproduced with permission of the copyright owner. Further reproduction prohibited without permission.

A mathematical model was derived to explain this breaking phenomenon. Its predictions for the onset of rolling were in close agreement with the experimental observations. The model also yielded qualitative information on the flux of short wave energy with respect to the carrier wave. This result is useful in understanding the previously observed (Mitsuyasu, 1966) phenomenon of the apparent total suppression of natural wind generated gravity wavelets which occurred as the carrier wave steepness was increased beyond a certain limit.

Also included is a comprehensive account of the 'maser' mechanism of wind-wave generation proposed by Longuet-Higgins (1969b), a critical review of a paper by Hasselmann (1971) disclaiming its viability and an alternate analysis of the coupling between a short wave field riding on a long finite amplitude gravity wave. As this analysis does not suffer from certain implicit fundamental assumptions inherent in Hasselmann's analysis, it is felt that it is a significant contribution towards a correct evaluation of the 'maser' mechanism.

Reproduced with permission of the copyright owner. Further reproduction prohibited without permission.

TO JOHN BANNER

with deep affection

Reproduced with permission of the copyright owner. Further reproduction prohibited without permission.

ACKNOWLEDGMENTS

The author gratefully acknowledges the guidance and support of Professor O.M. Phillips with whom it has been a privilege to work. He also wishes to thank Professor Francis Bretherton for his capable guidance especially in the theoretical section.

The author would like to express his appreciation to Bernie Baker and Robert Moog for their excellent job in rebuilding the wind-wave facility. Ron Flower assisted in setting up the wave-measurement system and Jeff Michael repaired the A/D converter at a crucial stage of the investigation. Their assistance is greatly appreciated.

The drafting of figures was most capably done by Dean Pendleton and the arduous task of producing meaningful prints from difficult negatives was efficiently carried out by Mark Metzler, who is also responsible for the reproduction of figures.

Finally, the author feels strongly indebted to Dr. Robert Green of the Department of Mechanics and Material Science for authorizing the use of that department's facilities and equipment and for his willingness to assist.

Reproduced with permission of the copyright owner. Further reproduction prohibited without permission.

TABLE OF CONTENTS

Page

Abstract

Acknowledgments

List of Figures
List of Plates
List of Symbols

§ 1 INTRODUCTION 1

§ 2 SCOPE OF THE INVESTIGATION 10

§ 3 THEORETICAL CONSIDERATIONS 13

§ 4 THE WIND-WAVE FACILITY 47

§ 5 AIRFLOW MEASUREMENTS

Intrumentation and Procedure 50

Results 51

§ 6 WAVE MEASUREMENTS

Instrumentation and Procedure 53

Results 64

§ 7 ANALYSIS OF THE OBSERVED BREAKING PHENOMENON 73

§ 8 COMPARISON BETWEEN THEORY AND OBSERVATION 82

§ 9 CONCLUSIONS 86

Appendix I Transformation from (ξ, η) to (x, z) coordinates 89
Appendix II Curvature in (ξ, η) coordinates 91
Appendix III Error analysis for the phase-averaging computations 93
Appendix IV Listings of computer programs 99

REFERENCES 110

VITA

Reproduced with permission of the copyright owner. Further reproduction prohibited without permission.

LIST OF FIGURES

Figure		Page
1	Model of ripple structure in rest and moving frames.	114
2	Wind-wave facility.	115
3	Absorption of wave groups as detected by wave probes ~ 2 m and ~ 4 m upstream of beach.	116
4	Variation of vertical mean wind velocity profiles and streamwise pressure gradient as a function of wave amplitude.	117
5	Wave probe calibration curve.	118
6	Noise (electronic and computational) spectra.	119
7	Normalized spectral window shape.	120
8	Spectrum for the purely wind-driven situation at the first fetch (4.27 m).	121
9	Spectrum for the purely wind-driven situation at the second fetch (7.32 m).	121
10	Spectrum for the purely wind-driven situation at the third fetch (10.36 m).	121
11	Spectrum and phase-averaged distribution for the case of superposed 1.7 Hz mechanically-generated waves with slope ~ 0.03 at the first fetch (4.27 m).	122

Reproduced with permission of the copyright owner. Further reproduction prohibited without permission.

LIST OF FIGURES (continued)

Figure		Page
12	Spectrum and phase-averaged distributions for the case of superposed 1.7 Hz mechanically-generated waves with slope ~0.03 at the second fetch (7.32 m).	123
13	Spectrum and phase-averaged distributions for the case of superposed 1.7 Hz mechanically-generated waves with slope ~ 0.03 at the third fetch (10.36 m).	124
14	Spectrum and phase-averaged distributions for the case of superposed 1.7 Hz mechanically-generated waves with slope ~ 0.06 at the first fetch (4.27 m).	125
15	Spectrum and phase-averaged distributions for the case of superposed 1.7 Hz mechanically-generated waves with slope ~0.06 at the second fetch (7.32 m).	126
16	Spectrum and phase-averaged distributions for the case of superposed 1.7 Hz mechanically-generated waves with slope ~0.06 at the third fetch (10.36 m).	127
17	Spectrum and phase-averaged distributions for the case of superposed 1.7 Hz mechanically-generated waves with slope ~0.175 at the first fetch (4.27 m).	128
18	Spectrum and phase-averaged distributions for the case of superposed 1.7 Hz mechanically-generated waves with slope ~0.175 at the second fetch (7.32 m).	129
19	Spectrum and phase-averaged distributions for the case of superposed 1.7 Hz mechanically-generated waves with slope ~0.175 at the third fetch (10.36 m).	130
20	Spectrum and phase-averaged distributions for the case of superposed 1.7 Hz mechanically-generated waves with slope ~0.29 at the first fetch (4.27 m).	131

Reproduced with permission of the copyright owner. Further reproduction prohibited without permission.

LIST OF FIGURES (continued)

Figure		Page
21	Spectrum and phase-averaged distributions for the case of superposed 1.7 Hz mechanically-generated waves with slope $\sim$ 0.29 at the second fetch (7.32 m).	132
22	Spectrum and phase-averaged distributions for the case of superposed 1.7 Hz mechanically-generated waves with slope $\sim$ 0.29 at the third fetch (10.36 m).	133
23	Proposed model for rolling-breaking wave.	134

Reproduced with permission of the copyright owner. Further reproduction prohibited without permission.

LIST OF PLATES

Plate		Page
1	Surface structure for purely wind-driven situation at the first fetch (4.27 m).	135
2	Surface structure for purely wind-driven situation at the second fetch (7.32 m).	136
3	Surface structure for purely wind-driven situation at the third fetch (10.36 m).	137
4	Surface structure with superposed 1.7 Hz mechanically-generated waves (slope $\sim$ 0.03) at the first fetch (4.27 m).	138
5	Surface structure with superposed 1.7 Hz mechanically-generated waves (slope $\sim$ 0.03) at the second fetch (7.32 m).	139
6	Surface structure with superposed 1.7 Hz mechanically-generated waves (slope $\sim$ 0.03) at the third fetch (10.36 m).	140
7	Surface structure with superposed 1.7 Hz mechanically-generated waves (slope $\sim$ 0.06) at the first fetch (4.27 m).	141
8	Surface structure with superposed 1.7 Hz mechanically-generated waves (slope $\sim$ 0.06) at the second fetch (7.32 m).	142
9	Surface structure with superposed 1.7 Hz mechanically-generated waves (slope $\sim$ 0.06) at the third fetch (10.36 m).	143

Reproduced with permission of the copyright owner. Further reproduction prohibited without permission.

LIST OF PLATES (continued)

Plate		Page
10	Surface structure with superposed 1.7 Hz mechanically-generated waves (slope ~ 0.175) at the first fetch (4.27 m).	144
11	Surface structure with superposed 1.7 Hz mechanically-generated waves (slope ~ 0.175) at the second fetch (7.32 m).	145
12	Surface structure with superposed 1.7 Hz mechanically-generated waves (slope ~ 0.175) at the third fetch (10.36 m).	146
13	Surface structure with superposed 1.7 Hz mechanically-generated waves (slope ~ 0.29) at the first fetch (4.27 m).	147
14	Surface structure with superposed 1.7 Hz mechanically-generated waves (slope ~ 0.29) at the second fetch (7.32 m).	148
15	Surface structure with superposed 1.7 Hz mechanically-generated waves (slope ~ 0.29) at the third fetch (10.36 m).	149

Reproduced with permission of the copyright owner. Further reproduction prohibited without permission.

LIST OF SYMBOLS

a' amplitude function for sine wave signal

a wave steepness as measured by amplitude x wave number product

A digitized data point with magnitude A at index I

β wave amplitude

B constant in Bernoulli equation

B_w bandwidth of spectral window

c phase speed

C long wave phase speed

c_ϵ short wave energy flux velocity

χ characteristic function for short wave energy flux

cm centimeter

Δp change in p

d air channel half-height

δ frequency deviation

db decibels

E energy density

ϵ short wave length to long wave length ratio

η_o^{sp} wave elevation at which stagnation point occurs

ξ lateral curvilinear coordinate

η vertical curvilinear coordinate

ξ, ζ functions for wave surface

f frequency in hertz

F, G general notation for functions

^oF Fahrenheit degrees

Reproduced with permission of the copyright owner. Further reproduction prohibited without permission.

LIST OF SYMBOLS (continued)

γ surface tension (dimensional)

g gravitational constant (dimensional)

γ^* surface tension (dimensionless)

g^* gravitational constant (dimensionless)

Hz hertz

$\hat{h}(x)$ depth of lower boundary

$h(\xi,\eta)$ local scale factor for curvilinear coordinates (ξ,η)

I index of data point A(I)

ips inches per second

k wave number

K long wave number

κ curvature

λ wavelength

L number of positive zero-crossings in digitized wave record

m meters

mm millimeters

M subrecord length

m/s meters per second

$\bar{n}$ average frequency

n intrinsic frequency

$\hat{n}$ apparent frequency in moving frame

N positive integer

ν_a viscosity of air

ν_w viscosity of water

Reproduced with permission of the copyright owner. Further reproduction prohibited without permission.

LIST OF SYMBOLS (continued)

ω vorticity normal to (ξ, η) plane

Ω long wave frequency

$O(1)$, $o(1)$ standard ordering operations [see e.g. Van Dyke (1964)]

ϕ smoothing function of compact support (in space and time)

p reduced pressure

p^a ambient kinematic pressure on water surface

ψ' stream function

τ number of subrecords of length $\frac{T}{M}$

ρ_a density of air

ρ_w density of water

R wave Reynolds number $\left(= \frac{1}{K\nu_w}\left(\frac{\Omega}{K}\right)\right)$

$S_{\xi\xi}$ radiation stress component (normal)

$S_{\eta\xi}$ radiation stress component (shear)

Θ phase function

θ inclination of mean wave surface to the horizontal

t time

u_i velocity component in an orthogonal coordinate system

u_* shear velocity

U mean velocity tangential to wave surface in $-\xi$ direction

u_d wind drift velocity in moving frame

u_d^* wind drift velocity in rest frame

$'$ means rapidly varying quantity associated with ripple layer variables

Reproduced with permission of the copyright owner. Further reproduction prohibited without permission.

LIST OF SYMBOLS (continued)

$\hat{\ }$	means slowly varying quantity associated with ripple layer variables
$\bar{\ }$	means slowly varying or mean quantity
x	cartesian coordinate (horizontal)
z	cartesian coordinate (vertical)
W	long wave vertical velocity component
$\tilde{\simeq}$	approximately equal to
$_r$	subscript denotes reference quantity

Reproduced with permission of the copyright owner. Further reproduction prohibited without permission.

§1 INTRODUCTION

Associated intimately with naturally observed wind-waves are ripples with length scales ranging from a few centimeters down to fractions of a millimeter. Sometimes these ripples are distributed over the entire surface of the longer gravity waves upon which they are riding; sometimes they are seen to be predominantly localized or trapped on the forward faces of the longer gravity waves. It is with these phenomena that this investigation is concerned.

Rippling effects on longer waves have been studied by several authors in an effort to understand their dynamical significance. Schooley (1958) used high-speed photography to record profiles of wind-created water waves in the capillary-gravity transition region. At sufficiently high windspeeds, ripples (wavelengths $\sim$ 3 mm) travelling at the same speed as longer waves (wavelengths $\sim$ 8 cm) were clearly observed on the forward faces of the latter. The ripple profiles were similar to the profiles predicted for finite amplitude (irrotational) capillary waves by Crapper (1957). Cox (1958) obtained quantitative surface slope data in a pioneering laboratory study, revealing the importance of nonlinear effects for high frequency ripples riding on longer wind-generated gravity wavelets with frequencies around 6.6 Hz. From upwind-downwind surface slope measurements, which resolved ripples with wavelengths down to about 2 mm,

Reproduced with permission of the copyright owner. Further reproduction prohibited without permission.

frequency spectra for the streamwise surface slope component and ripple phase speeds were reported, showing their nonlinear variation with increasing windspeed. The occurrence of ripples trapped on the forward faces of gravity wavelets was observed to become more pronounced with increasing windspeed as the gravity wavelets reached their maximum steepness. Similar observations were recorded for plunger-generated maximally steep gravity wavelets (also with a generated frequency of about 6.6 Hz) except that leading edge rippling was reported in the absence of any wind excitation. As the windspeed was increased, ripples were observed on the rear faces of the gravity wavelets together with the persistent leading face trapping of ripples.

Longuet-Higgins (1963) gave an analysis for the nonlinear transfer of energy from gravity waves to capillary waves in the absence of any wind excitation. The ripple generation was attributed to normal stresses arising from surface tension effects at the sharp crests of the progressive gravity waves as they reached their maximum steepness. The analysis used surface tension as a small perturbation on the basic flow of pure gravity waves of nearly maximum steepness. Small amplitude travelling capillary wave solutions with the same phase speed as the basic gravity wave were sought. The resulting solution represented a ripple upstream of the crest (on the forward face of the gravity wave) with wavenumber given by the classical infinitesimal value and steepness varying as the underlying orbital velocity of the gravity wave.

Reproduced with permission of the copyright owner. Further reproduction prohibited without permission.

The effect of viscocity was also included. Physically, energy was fed into the ripples not only by the surface tension effects at the crest, but also by radiation stresses produced through interaction with the gravity wave and was drained away through viscous dissipation. Crapper (1970) extended the analysis to finite amplitude ripples by considering the finite amplitude capillary wave solution of Crapper (1957) as stationary waves on a slowly-varying running stream and using the method of the averaged Lagrangian to obtain an energy equation for the system. Numerical solutions of the resulting nonlinear ordinary differential equation for the ripple characteristics for various gravity wavelengths and steepnesses were given. These showed the capillary wave steepness distribution and the number of capillary ripples measured from the gravity wave crest as a function of the above parameters. Agreement with Cox's (1958) experimental results for the case of no wind was not conclusive. A significant advantage of Crapper's analysis was that the occurrence of ripples on the rear faces of the gravity waves was allowed. Both analyses predicted the ratio of energy drained from the gravity waves by the ripple generation and subsequent viscous ripple damping to the energy dissipated directly by viscous action over a range of long wave scales and steepnesses. This showed the effectiveness of trapped leading edge ripples in the damping of finite amplitude free gravity waves.

Reproduced with permission of the copyright owner. Further reproduction prohibited without permission.

Another aspect of the rippling phenomenon was discussed recently by McGoldrick (1972) who pointed out that the rippling observed on small progressive gravity waves in the absence of wind could be explained in terms of nearly resonant harmonic nonlinear interactions. He considered the spatial modulation of a single Fourier progressive wave mode by a nonlinear interaction with its n^{th} harmonic for the cases where the dispersion relation yielded free waves and their free n^{th} harmonic that could travel at identical phase speeds. The case of capillary-gravity waves has a dispersion relation satisfying this criterion for some n and McGoldrick was able to demonstrate experimentally the existence of ripples which covered both forward and rear faces of short gravity-waves [of about the same wavelength as were generated by Cox (1958) in the absence of wind]. He also justified the observations by analysing a model equation more amenable to interaction analysis yet which retained the essential features of the water wave equations.

A valuable point brought out by McGoldrick was the relationship between his analysis and that of Longuet-Higgins (1963) and Crapper (1970). With increasing n, the ratio of ripple wavelength to that of the fundamental producing them became increasingly small as $\frac{k(\omega)}{k(n\omega)} = \epsilon = \frac{1}{n}$ In McGoldrick's resonance calculation it was tacitly assumed that the wavelengths (and frequencies) involved were of the same order, resulting in the dependence of the resonance problem on the single small parameter α (the steepness of the fundamental), which was a measure of the nonlinearity produced by

Reproduced with permission of the copyright owner. Further reproduction prohibited without permission.

finite amplitude effects. For large n, ϵ became a second small parameter and the problem now involved two small parameters, α and ϵ . Thus the problem analyzed by McGoldrick was for the case where $\frac{\alpha}{\epsilon} = o(1)^*$ as $\alpha \longrightarrow 0$. The analyses of Longuet-Higgins and of Crapper depended crucially on ϵ being small and held for the case where $\frac{\alpha}{\epsilon} = O(1)^*$ as $\epsilon \longrightarrow 0$. Their analysis broke down for large ϵ , whereas this was precisely when McGoldrick's analysis became valid. Thus the two analysis relate to complementary regions of the (α, ϵ) parameter space for the problem.

Up to this point, the analytical studies which have been reported here were concerned with certain rippling effects on gravity waves; these rippling phenomena are characterized by approximately equal ripple and gravity wave phase speeds. In one situation, maximally steep gravity waves continuously generate trains of leading-edge ripples; these are intimately involved in the dissipation of gravity wave energy. In the other situation there is a transfer of energy from the basic gravity wave to one of its harmonics. This occurs via a nonlinear resonant interaction. Both phenomena have been observed and documented in the absence of wind excitation. Nevertheless, it is important to bear in mind that both mechanisms are potentially operable in the wind-driven situation, which is the focussing point of this investigation.

Over the past fifteen years a few theories have been proposed to account for various stages in the process of wave generation by

---

* The strict mathematical ordering notation is implied here.

Reproduced with permission of the copyright owner. Further reproduction prohibited without permission.

wind [see Miles (1957), Phillips (1957), Miles (1962)]. The physical mechanisms behind these linear theories have been discussed by many authors and will not be reiterated here [see Phillips (1966) for an overview current at the time of its publication]. Subsequent laboratory and field studies have revealed major discrepancies between observations and predictions of the theory relevant to that situation. In particular, with respect to the growth of existing gravity waves, Miles' shear flow theories suffer not only from inability to make predictions consistent with observations [see introduction to Longuet-Higgins (1969b) for details] but also on the marked sensitivity of the theory as to how the wave-induced air-flow perturbations are assumed to interact with the turbulence in the wind field [Davis (1970)]. Motivated by the shortcomings of the shear flow theories, Longuet-Higgins (1969b) described a speculative nonlinear wind-wave generation mechanism (named by him the 'maser' mechanism) in situations where strong interaction occurs between already-established long gravity waves and ripples which cover the entire gravity wave surface. He proposed that the bulk of the momentum available for transfer from the wind to the waves is passed to the ripple field. The ripples are amplified and often caused to break predominantly on the forward faces of the longer gravity waves. This occurs as a consequence of the following:

(a) the distribution of orbital velocities of the long wave field has the kinematic effect of producing local stretching or compression

Reproduced with permission of the copyright owner. Further reproduction prohibited without permission.

of the ripple train depending on which part of the long wave our attention is focussed.

(b) the motion of the long waves results in an accelerating frame for the ripples with gravity effectively reduced at the crests.

(c) flow convergence at the crests and divergence at the troughs of the long waves, causing an interaction through the radiation stresses [see Longuet-Higgins and Stewart (1960)].

This selective breaking process is the basis of the mechanism and potentially provides the momentum and energy supply for the growth of the long waves. Longuet-Higgins also provided order-of-magnitude estimates for long wave growth rates based on the postulated mechanism which compared favorably with the field measurements of growth rates of Barnett and Wilkerson (1967).

Other investigators have demonstrated the potential importance of the microstructure of the water surface in coupling the airflow to the long wave field. Barger et al (1970) studied the effects of an artificial sea slick upon the air-sea interaction process. From their measurements of wave height and fluctuating wind velocity components, the following conclusions were drawn:

(a) the presence of the surface slick damped small surface waves resulting in an increase of wind speed over the slick, a decrease in the profile roughness length and a decrease in energy of the dominant wind-driven sea. The most noteworthy observation, however,

Reproduced with permission of the copyright owner. Further reproduction prohibited without permission.

was the marked reduction in energy of even the lowest frequency components of the wave energy, demonstrating that the slick interfered substantially with the mechanism of generation of wind waves in all regions of the frequency spectrum.

(b) the slick induced an apparent decoupling of the undulating wave surface from the atmosphere as reflected by the atmospheric Reynolds stress spectrum. Before and after the passage of the slick, the atmosphere was found to be strongly influenced by the entire spectrum of the underlying sea surface. This indicated a strong coupling between very different scales of motion and suggested the need for the theoretical models of wind-wave generation to consider the role of the ripples in the process.

(c) the final general conclusion was that before realistic models of the air-sea boundary processes can be constructed, the role of the short waves in the total dynamics must be clearly identified.

To establish the postulated 'maser' mechanism of Longuet-Higgins (1969b) on a firmer basis, a rigorous analysis of the model was clearly needed. Hasselmann (1971) considered the interaction between short gravity waves and larger-scale flows. He claimed that the effect of the wave field on the mean flow could be described by an interaction stress tensor and a surface mass flux. He applied his results to the Longuet-Higgins model and concluded that the work done on the long waves by the interaction stresses was almost exactly balanced by the loss of potential energy arising from the

Reproduced with permission of the copyright owner. Further reproduction prohibited without permission.

surface mass flux. He also asserted that the presence of short gravity waves could only cause damping of the long waves independent of the direction of the wind. However, a careful review of his basic equations revealed that certain fundamental assumptions were implicit in his decomposition of the pressure field and in the method of averaging used. As a result, the analysis ignores terms which appear to be comparable to those retained in arriving at the conclusions. (These matters are taken up in greater detail in the section entitled "Theoretical Considerations"). Consequently, it is felt that the viability of the proposed 'maser' mechanism has not been convincingly disproved. It can then be seen that a well-defined description of the phenomenon based on experimental observations would provide a valuable complement for a correct theory both as a basis for the model initially and then later as a means of testing the predictions of the model. It is the aim of this investigation to make a substantial contribution toward this goal.

Reproduced with permission of the copyright owner. Further reproduction prohibited without permission.

§2 SCOPE OF THE INVESTIGATION

This investigation was initiated to extend our understanding of the interaction between wind and gravity waves and, in particular, the role played by short waves and wind drift. The 'maser' mechanism postulated by Longuet-Higgins (1969b) had suggested that the short wave field plays an active and crucial role in the growth of long waves in some circumstances and their attenuation in others. Some empirical evidence of the strong coupling between the wind and the short wave structure has been found in the field by the substantial modification to both wind and wave fields when a surface slick was introduced to suppress the short wave field [Barger, et al (1970)]. The questions raised by these investigations provided much of the initial motivation for this study.

A series of observations of wind-wave interactions were made in a laboratory wind-wave tank in which the parameters varied were the slope of a mechanically-generated low frequency gravity wave and the wave fetch. For a fixed wind tunnel fan speed, the type of interactions observed ranged from very weak to highly nonlinear. The observations were recorded photographically and quantitatively using wave amplitude sensing probes for the wave field and pitot tube and pressure drop measurements to document the mean flow over the wave field. The wave probe data was analyzed in both the time domain and the frequency domain by phase-averaging and Fourier analysis to express complementary properties of the

Reproduced with permission of the copyright owner. Further reproduction prohibited without permission.

wave field. Along with the carefully documented visualization provided by the surface photography system, this provided an opportunity to examine and analyze certain fundamental aspects of the observed phenomena.

This study begins with a detailed survey of the existing literature concerning rippling effects on basic finite amplitude gravity wave flows, both with and without wind excitation. It then focusses temporarily on the 'maser' mechanism proposed by Longuet-Higgins (1969b) and on a paper by Hasselmann (1971) claiming its non-tenability. An alternate theoretical approach aimed at circumventing the difficulties associated with Hasselmann's approach is given in which the nature of the coupling between the short wave field and the long wave field is established rigorously using an asymptotic slowly varying wavetrain approach. This contribution is a significant step toward an accurate evaluation of the viability of the 'maser' mechanism.

From the observations made when the basic gravity waves were driven by the wind beyond their maximum steepness, a model was developed of the limiting mechanism consistent with these observations and differing from existing accounts of wave breaking. Its quantitative predictions of the onset of breaking agreed well with the observations. This proposed mechanism also sheds some light on the previously reported but unexplained phenomenon in which the finite amplitude low frequency carrier wave of sufficient amplitude results in the almost complete disappearance of the natural wind-

Reproduced with permission of the copyright owner. Further reproduction prohibited without permission.

generated gravity wavelets [Mitsuyasu (1966)]. The investigation concludes with a summary of the contributions made and suggests directions in which this work might proceed.

Reproduced with permission of the copyright owner. Further reproduction prohibited without permission.

§3 THEORETICAL CONSIDERATIONS

In order to investigate the role of ripples in the generation of gravity waves according to the proposed 'maser' mechanism, it seems appropriate to seek a description in which the influence of the ripples is confined to a thin layer at the mean water surface. The effect of the ripples is then interpreted as a modification of the kinematic and dynamic boundary conditions for the long gravity wave field, regarded as the mean flow. The central problem is the coupling between the ripple layer flow and the mean flow. Before these notions are formalized mathematically, the scope, constraints and scalings for the problem are discussed.

As an initial goal, a description of the back interaction of the ripple field on the gravity wave field is sought, given the phasing and duration of the ripples with respect to the gravity waves. The question of the mechanism of ripple regeneration by the wind is considered a separate problem, possibly in the realm of Miles' shear flow theory (1959, 1962b). The phenomenon under investigation is seen to involve a highly nonlinear binary wave system interaction with the following properties:

(a) the characteristic ratio of ripple wavelength to gravity wavelength is very small, as is the corresponding characteristic amplitude ratio. However, the characteristic steepness ratio is of order unity.

(b) the characteristic ripple phase speed is of the same order

Reproduced with permission of the copyright owner. Further reproduction prohibited without permission.

as the maximum orbital velocities associated with the gravity wave field. This permits a strong interaction between the two fields. It is also consistent with the observation that during this particular type of interaction process, the gravity waves are seen to sweep through the ripple field. This occurs because the gravity wave phase speed is significantly higher than the associated orbital speeds (except at the crest of a gravity wave about to break).

It should be stressed that this situation is distinctly different from the case of propagating gravity waves of maximal slope. In the latter, ripples are observed continuously at the forward edge of the crest. This is a situation where the ripple phase speed is of the same order as the gravity wave phase speed. Some very obvious qualitative differences are observable in the surface photographs shown in the section entitled "Wave Measurements" where this matter is taken up in greater depth. It is also apparent that both processes might well be occurring simultaneously and in varying proportions, depending on the wind and wave conditions.

A convenient starting point is to review Hasselmann's (1971) Eulerian analysis of the problem. Hasselmann began with the (dimensional) Navier-Stokes equations, continuity equation and kinematic and dynamic boundary conditions for an inviscid, homogeneous fluid with a free surface:

Reproduced with permission of the copyright owner. Further reproduction prohibited without permission.

$$\frac{\partial u_i}{\partial t} + \frac{\partial}{\partial x_j}(u_i u_j) + \frac{\partial p}{\partial x_i} = 0, \qquad -h \le x_3 \le \xi(x_\alpha, t) \tag{3.1}$$

$$\frac{\partial u_i}{\partial x_i} = 0, \qquad -h \le x_3 \le \xi(x_\alpha, t) \tag{3.2}$$

$$p(\xi) - g\xi = p^a, \qquad x_3 = \xi(x_\alpha, t) \tag{3.3}$$

$$\frac{\partial \xi}{\partial t} + u_\alpha(\xi)\frac{\partial \xi}{\partial x_\alpha} - u_3(\xi) = 0, \qquad x_3 = \xi(x_\alpha, t) \tag{3.4}$$

$$u_\alpha(-\hat{h})\frac{\partial \hat{h}}{\partial x_\alpha} + u_3(-\hat{h}) = 0, \qquad x_3 = -\hat{h}(x_\alpha) \tag{3.5}$$

where p is the kinematic pressure minus the equilibrium pressure $-gx_3$ and

Latin subscripts range over 1 to 3

Greek subscripts range over 1 and 2

"Averaged" equations [equations (6) - (10) in his paper] were obtained from (3.1) - (3.5), using a decomposition consisting of a rapidly oscillating wave field u_i', ξ' superposed on a mean flow $\bar{u}_i, \bar{\xi}$ which as assumed to vary slowly with respect to the horizontal coordinates and time. The mean properties of the wave field and the depth were regarded as slowly varying functions. Means were defined "in the usual manner as horizontal and time averages over

Reproduced with permission of the copyright owner. Further reproduction prohibited without permission.

dimensions intermediate between the periodicities of the wave field and the characteristic scales of the slowly varying field". Also, the mean pressure field was assumed to be decomposable into two components

$$\bar{p} = p^m + p^w$$

where p^m was defined as "the mean pressure in the absence of the wave field, i.e. the pressure as determined from the usual Laplace equation and boundary conditions for the pressure with the fluctuating velocities and surface displacements set to zero". In practice

$p[x_i, \xi(x_i,t), t] - g\xi(x_i,t) = p^a$ was not "averaged" directly to give (8)* but rather (8)* is given as a definition for p^m on the boundary $z = \bar{\xi}(x_i,t)$

i.e. $$p^m(x_i, \bar{\xi}(x_i,t), t) - g\bar{\xi}(x_i,t) \equiv \bar{p}^a \qquad (8)^*$$

and the difference between the "average" of (3.3) and (8)*

i.e. $\overline{p(x_i,\xi(x_i,t),t) - g\xi(x_i,t) = p^a}$ and (8)* was to yield a boundary condition for p^w.

It is demonstrated below that

(1) the averaging process is not exact and involves an implicit approximation.

(2) the decomposition of the mean pressure field is not formally exact and involves an implicit simplifying assuption.

(3) the effects of these assumptions and/or approximations is to cast considerable doubt on the validity of the analysis and its conclusions.

---

* In Hasselmann (1971)

Reproduced with permission of the copyright owner. Further reproduction prohibited without permission.

A mathematical representation of the averaging procedure described and used by Hasselmann (1971) is

$$\overline{f(x_\alpha, x_3, t)} = \int_{-\infty}^{\infty} f(x_\alpha - \chi_\alpha, x_3, t-\tau)\, \phi(\chi_\alpha, \tau)\, d\chi_\alpha\, d\tau$$

where ϕ is a suitably smooth weighting function which vanishes outside the local interval in space and time "intermediate between the periodicities of the wave field and the characteristic scales of the slowly varying field". Also $\int \phi\, d\chi_\alpha d\tau = 1$.

This formal averaging process holds x_3 fixed and thus presents no difficulties in the interior region away from the boundaries. However, for quantities evaluated at the fluctuating surface prior to averaging, considerable care is needed, as the operations of averaging and evaluation at either the instantaneous or the mean surface do not commute in general. Hasselmann (1971) [eqn. 9] claims

$$\frac{\partial \bar{\zeta}}{\partial t} + \bar{u}_\alpha(\bar{\zeta}) \frac{\partial \bar{\zeta}}{\partial x_\alpha} - \bar{u}_3(\bar{\zeta}) = -\frac{\partial}{\partial x_\alpha} \overline{\int_{\zeta}^{\zeta+\zeta'} u_\alpha\, dx_3}$$

to be the average of $\frac{\partial \zeta}{\partial t} + u_\alpha(\zeta) \frac{\partial \zeta}{\partial x_\alpha} - u_3(\zeta) = 0$. It is shown below that this is not exact.

The average of this last equation is given formally by

$$\overline{\frac{\partial \zeta}{\partial t}} + \overline{u_\alpha(\zeta) \frac{\partial \zeta}{\partial x_\alpha}} - \overline{u_3(\zeta)} = 0$$

We have $\overline{\frac{\partial \zeta}{\partial t}} = \frac{\partial}{\partial t} \bar{\zeta}$ by inspection of the definition of the averaging process.

Next we consider the second and third terms. These may be expressed in terms of quantities measured at the mean free surface $x_3 = \bar{\zeta}(x_\alpha, t)$ using the continuity equation as follows

$$\frac{\partial u_\alpha}{\partial x_\alpha} + \frac{\partial u_3}{\partial x_3} = 0$$

Reproduced with permission of the copyright owner. Further reproduction prohibited without permission.

Now integrate from $x_3 = \bar{\zeta}(x_\alpha,t)$ to $x_3 = \zeta(x_\alpha,t)$

giving $$\int_{\bar{\zeta}}^{\zeta} \frac{\partial u_\alpha}{\partial x_\alpha}\, dx_3 + u_3(\zeta) - u_3(\bar{\zeta}) = 0$$

i.e. $$\frac{\partial}{\partial x_\alpha}\int_{\bar{\zeta}}^{\zeta} u_\alpha\, dx_3 - u_\alpha(\zeta)\frac{\partial \zeta}{\partial x_\alpha} + u_\alpha(\bar{\zeta})\frac{\partial \bar{\zeta}}{\partial x_\alpha} + u_3(\zeta) - u_3(\bar{\zeta}) = 0$$

So $$u_\alpha(\zeta)\frac{\partial \zeta}{\partial x_\alpha} - u_3(\zeta) = \frac{\partial}{\partial x_\alpha}\int_{\bar{\zeta}}^{\zeta} u_\alpha\, dx_3 + u_\alpha(\bar{\zeta})\frac{\partial \bar{\zeta}}{\partial x_\alpha} - u_3(\bar{\zeta})$$

Averaging gives $$\overline{u_\alpha(\zeta)\frac{\partial \zeta}{\partial x_\alpha}} - \overline{u_3(\zeta)} = \overline{\frac{\partial}{\partial x_\alpha}\int_{\bar{\zeta}}^{\zeta} u_\alpha\, dx_3} + \overline{u_\alpha(\bar{\zeta})\frac{\partial \bar{\zeta}}{\partial x_\alpha}} - \overline{u_3(\bar{\zeta})}$$

From the definition, $$\overline{\frac{\partial}{\partial x_\alpha}\int_{\bar{\zeta}}^{\zeta} u_\alpha\, dx_3} = \frac{\partial}{\partial x_\alpha}\overline{\int_{\bar{\zeta}}^{\zeta} u_\alpha\, dx_3}$$

However, consider the third term: by definition

$$\overline{u_3(\bar{\zeta})} \equiv \overline{u_3(x_\alpha, \bar{\zeta}(x_\alpha,t), t)} = \int_{-\infty}^{\infty} u_3(x_\alpha - \chi_\alpha, \zeta(x_\alpha-\chi_\alpha, t-\tau), t-\tau)\,\phi(\chi_\alpha,\tau)\, d\chi_\alpha\, d\tau$$

But

$$\bar{u}_3(\bar{\zeta}) = \int_{-\infty}^{\infty} u_3(x_\alpha - \chi_\alpha, \bar{\zeta}(x_\alpha,t), t-\tau)\,\phi(\chi_\alpha,\tau)\, d\chi_\alpha\, d\tau$$

So $\overline{u_3(\bar{\zeta})} \neq \bar{u}_3(\bar{\zeta})$ on account of the (x,t) dependence at $x_3 = \zeta$ and $x_3 = \bar{\zeta}$. Thus averaging and evaluation at the mean (or instantaneous) free surface do not commute. The relationship between the two can be obtained by expanding in a Taylor series as follows:

$$\bar{\zeta}(x_\alpha - \chi_\alpha, t-\tau) = \bar{\zeta}(x_\alpha,t) + \chi_\alpha \bar{\zeta}_{x_\alpha}(x_\alpha,t) + \tau\bar{\zeta}_t(x_\alpha,t) + O(\chi_\alpha^2, \tau^2, \chi_\alpha\tau)$$

$$\therefore \overline{u_3(\bar{\zeta})} = \int_{-\infty}^{\infty} u_3(x_\alpha - \chi_\alpha, \bar{\zeta} + \chi_\alpha\bar{\zeta}_{x_\alpha} + \tau\bar{\zeta}_t + \cdots, t-\tau)\,\phi(\chi_\alpha,\tau)\, d\chi_\alpha\, d\tau$$

Reproduced with permission of the copyright owner. Further reproduction prohibited without permission.

$$= \int_{-\infty}^{\infty} u_3(x_\alpha - \chi_\alpha, \bar{\xi}(x_\alpha,\tau), t)\, \Phi(\chi_\alpha,\tau)\, d\chi_\alpha\, d\tau$$

$$+ \int_{-\infty}^{\infty} \chi_\alpha \frac{\partial u}{\partial \bar{\xi}_{x_\alpha}} (x_\alpha - \chi_\alpha, \bar{\xi}(x_\alpha,t), t-\tau)\, \Phi(\chi_\alpha,\tau)\, d\chi_\alpha\, d\tau$$

$$+ \int_{-\infty}^{\infty} \tau \frac{\partial u}{\partial \bar{\xi}_t} (x_\alpha - \chi_\alpha, \bar{\xi}(x_\alpha,t), t-\tau)\, \Phi(\chi_\alpha,\tau)\, d\chi_\alpha\, d\tau$$

$$+ \cdots\cdots$$

$$= \bar{u}_3(\bar{\xi}) + \int_{-\infty}^{\infty} \chi_\alpha \frac{\partial u}{\partial \bar{\xi}_{x_\alpha}} (x_\alpha - \chi_\alpha, \bar{\xi}(x_\alpha,t), t-\tau)\, \Phi(\chi_\alpha,\tau)\, d\chi_\alpha\, d\tau$$

$$+ \int_{-\infty}^{\infty} \tau \frac{\partial u}{\partial \bar{\xi}_t} (x_\alpha - \chi_\alpha, \bar{\xi}(x_\alpha,t), t-\tau)\, \Phi(\chi_\alpha,\tau)\, d\chi_\alpha\, d\tau$$

$$+ \cdots\cdots$$

The additional terms result from the fact that lines of constant z do not coincide with the mean free surface lines. The magnitude of the error terms will depend on the extent to which the surface $x_3 = \bar{\xi}(x_\alpha,t)$ can be regarded as locally parallel to x_3 = constant. This is clearly a strong assumption, but appears to play an underlying part in Hasselmann's transition from $u_3(\xi)$ via $\overline{u_3(\bar{\xi})}$ to $\bar{u}_3(\bar{\xi})$ in his equation (9). An analogous objection applied in the transition from $\overline{u_\alpha(\xi)\frac{\partial \xi}{\partial x_\alpha}}$ via $\overline{u_\alpha(\bar{\xi})\frac{\partial \bar{\xi}}{\partial x_\alpha}} = \overline{u_\alpha(\bar{\xi})}\frac{\partial \bar{\xi}}{\partial x_\alpha}$ to obtain $\bar{u}_\alpha(\bar{\xi})\frac{\partial \bar{\xi}}{\partial x_\alpha}$. Thus it is claimed that Hasselmann's mean free surface kinematic boundary condition [eqn.(9)] is an approximation with inherent, unknown error. However, it is possible that with a different averaging scheme (e.g. ensemble averaging) this boundary condition could be rendered exact.

Reproduced with permission of the copyright owner. Further reproduction prohibited without permission.

We consider next the more serious problem of the decomposition of the mean pressure $\bar{p}(x_i,t)$ into $\bar{p}^w(x_i,t)$ and $\bar{p}^m(x_i,t)$. This is an algebraically tenable decomposition in the interior of the flow. It is with certain accompanying inconsistencies existing at the instantaneous and mean free surfaces that we are concerned here.

Defining $\bar{p} = \bar{p}^m + \bar{p}^w$ in the interior introduced an indeterminancy into the problem. Hasselmann attempted to decouple the wave induced contribution ($\bar{p}^w$) to the mean pressure from the total mean pressure by asserting that $\bar{p}^m$ was determined from the inhomogeneous Laplace equation

$$\nabla^2 \bar{p}^m = \frac{\partial^2}{\partial x_i \partial x_j}\left(\bar{u}_i \bar{u}_j\right)$$

together with appropriate boundary conditions when the fluctuating velocities and surface displacements had been set equal to zero. The assumed pressure boundary condition was his equation (8). Based on a direct interpretation of this prescription, $\bar{\zeta}$ would obey

$$\frac{\partial \bar{\zeta}}{\partial t} + \bar{u}_\alpha(\bar{\zeta})\frac{\partial \bar{\zeta}}{\partial x_\alpha} - \bar{u}_3(\bar{\zeta}) = 0 \qquad \text{on } x_3 = \bar{\zeta}$$

Having thus determined $\bar{p}^m$, the other component $\bar{p}^w$ was supposedly obtainable from the full field equations for which $\bar{p}^m$ was prescribed, from the full kinematic boundary condition

$$\frac{\partial \bar{\zeta}}{\partial t} + \bar{u}_\alpha(\bar{\zeta})\frac{\partial \bar{\zeta}}{\partial x_\alpha} - \bar{u}_3(\bar{\zeta}) = -\frac{\partial}{\partial x_\alpha}\overline{\int_{\zeta}^{\bar{\zeta}} u_\alpha \, dx_3}$$

and from the difference between $\bar{p}^m - \rho g \bar{\zeta} = \bar{p}^a$ and the average of $p - \rho g \zeta = p^a$.

Reproduced with permission of the copyright owner. Further reproduction prohibited without permission.

Thus an informal use of the superposition principle appears to have been used here. The mean flow contribution to the mean velocity and mean pressure fields were assumed to be calculable a priori in the absence of the short wave field and then the corresponding contributions from the latter were assumed to be determinable from the full equations with the mean field contributions to the overall mean velocity and mean pressure already known.

There are a number of contentious concepts inherent in this method of attack. This approach ignores the modifications to the mean flow itself which are induced by the presence of the short-wave field. p^w, allegedly a property of the short wave field alone, is necessarily determined from the full field equations (with p^m prescribed) and so must involve the entire mean flow field. The prediction that when the fluctuating field is approximately linear, the wave induced mean pressure is obtained as $p^w = -\overline{u_3'^2}$ (p.194) simply does not hold true if there are significant mean vertical accelerations of the fluid near the free surface. This may be seen by going back to the linearized perturbation equations for the waves:

$$\left(\frac{\partial}{\partial t} + \bar{u}_j \frac{\partial}{\partial x_j} \right) u_3' + \frac{\partial p'}{\partial x_3} = - u_j' \frac{\partial \bar{u}_3}{\partial x_j}$$

If we consistently ignore the right hand side, we get, after use of the continuity equation and the kinematic free surface equation for ξ', that

$$\overline{-\xi' \frac{\partial p'}{\partial x_3}} = \overline{u_3'^2}$$

Reproduced with permission of the copyright owner. Further reproduction prohibited without permission.

We now use a Taylor series expansion on the free surface pressure boundary condition

$$p(\xi) - g\xi = p^a$$

We can expand

$$p(x_\alpha, x_3, t) = p(x_\alpha, x_3', t) + (x_3 - x_3')\frac{\partial p}{\partial x_3}(x_\alpha, x_3', t) + \frac{(x_3 - x_3')^2}{2}\frac{\partial^2 p}{\partial x_3^2}(x_\alpha, x_3', t) + \ldots.$$

and choosing

$$x_3 = \xi(x_\alpha, t) = \bar{\xi}(x_\alpha, t) + \xi'(x_\alpha, t)$$

and $x_3' = \bar{\xi}(x_\alpha, t)$ we have that

$$p(x_\alpha, \xi, t) = p(x_\alpha, \bar{\xi}, t) + \xi'\frac{\partial p}{\partial x_3}(x_\alpha, \bar{\xi}, t) + \frac{\xi'^2}{2}\frac{\partial^2 p}{\partial x_3^2}(x_\alpha, \bar{\xi}, t) + \ldots.$$

Now if we assume that $\overline{\phi(\xi)} = \bar{\phi}(\bar{\xi})$ with <u>negligible</u> error, then we average the above equation to obtain:

$$\overline{p(\xi)} = \bar{p}(\bar{\xi}) + \overline{\xi'\frac{\partial p}{\partial x_3}(\bar{\xi})} + \overline{\frac{\xi'^2}{2}\frac{\partial^2 p}{\partial x_3^2}(\bar{\xi})} + \ldots.$$

$$= \bar{p}(\bar{\xi}) + \overline{\xi'\frac{\partial p'}{\partial x_3}(\bar{\xi})} + \bar{\xi}'\frac{\partial \bar{p}}{\partial x_3}(\bar{\xi}) + \frac{1}{2}\overline{\xi'^2\frac{\partial^2 p}{\partial x_3^2}(\bar{\xi})} + \ldots.$$

So we have

$$\bar{p}(\bar{\xi}) + \overline{\xi'\frac{\partial p'}{\partial x_3}(\bar{\xi})} + \frac{1}{2}\overline{\xi'^2}\frac{\partial^2 \bar{p}}{\partial x_3^2}(\bar{\xi}) + \frac{1}{2}\overline{\xi'^2\frac{\partial^2 p'}{\partial x_3^2}(\bar{\xi})} + \ldots - g\bar{\xi} = \bar{p}^a$$

Subtracting $p^m = g\bar{\xi} + \bar{p}^a$ [equation (8)*] we are left with the conclusion that

$$p^w = -\overline{\xi'\frac{\partial p'}{\partial x_3}} - \frac{1}{2}\overline{\xi'^2}\frac{\partial^2 \bar{p}}{\partial x_3^2} - \frac{1}{2}\overline{\xi'^2\frac{\partial^2 p'}{\partial x_3^2}(\bar{\xi})} + \ldots \quad \text{on } x_3 = \bar{\xi}$$

$$= \overline{w'^2} - \frac{1}{2}\overline{\xi'^2}\frac{\partial^2 \bar{p}}{\partial x_3^2} - \frac{1}{2}\overline{\xi'^2\frac{\partial^2 p'}{\partial x_3^2}} + \ldots \quad \text{on } x_3 = \bar{\bar{\xi}}$$

---

* In Hasselmann (1971)

Reproduced with permission of the copyright owner. Further reproduction prohibited without permission.

which shows that ρ^{w} and $\bar{p}$ are intimately connected at $\bar{\zeta}$ and that ρ^{w} is not equal to $\overline{u_3'^2}$ when there exist significant mean accelerations near the mean free surface.

It is felt, therefore, that serious doubts exist as to whether the effect of short waves on a larger scale mean flow can be correctly represented by two terms, a "surface mass flux" and an "interaction stress tensor" which are functions of the short wave field alone. In doing so, certain assumptions and/or approximations are implicitly involved, the order of magnitude of which are unknown. As the effect of the short waves on the mean flow is transmitted via the modification to the mean flow boundary conditions, any assumptions or approximations imposed in the formulation must be considered to be of fundamental importance if a correct set of conclusions is to be derived. At this juncture, it is difficult to evaluate the extent to which Hasselmann's conclusion are in error; however, a different approach is presented now in which these fundamental uncertainties are circumvented.

Even though the rippling phenomenon is frequently three-dimensional in character, it is felt that the fundamental coupling between the ripple flow and the gravity wave flow can be established by considering the simpler case of the following two-dimensional model.

The Navier-Stokes equations for a constant density, two-dimensional fluid flow with a free surface are:

Reproduced with permission of the copyright owner. Further reproduction prohibited without permission.

$$\frac{\partial u}{\partial t} + \frac{\partial}{\partial x}(u^2) + \frac{\partial}{\partial z}(uw) + \frac{\partial p}{\partial x} = \nu_\omega\left(\frac{\partial^2 u}{\partial x^2} + \frac{\partial^2 u}{\partial z^2}\right)$$

$$\frac{\partial w}{\partial t} + \frac{\partial}{\partial x}(uw) + \frac{\partial}{\partial z}(w^2) + \frac{\partial p}{\partial z} = \nu_\omega\left(\frac{\partial^2 w}{\partial x^2} + \frac{\partial^2 w}{\partial z^2}\right)$$

$$\frac{\partial u}{\partial x} + \frac{\partial w}{\partial z} = 0$$

$$\frac{\partial \zeta}{\partial t} + u\frac{\partial \zeta}{\partial x} - w = 0 \qquad \text{on } z = \zeta(x,t)$$

$$p(\zeta) - g\zeta - \frac{\gamma \zeta''}{(1+\zeta'^2)^{3/2}} = p^a \qquad \text{on } z = \zeta(x,t)$$

$$\nu_\omega \frac{\partial u}{\partial z} = u_*^2 \qquad \text{on } z = \zeta(x,t)$$

$$u = w = 0 \quad \text{as} \quad z \to -\infty$$

Here, p is the reduced pressure i.e. the kinematic pressure P/ρ minus the equilibrium pressure $-gz$.

We wish to examine the situation where we have a primary long gravity wave (wavenumber K, amplitude β and frequency Ω) moving in the positive x direction with speed $C = \Omega/K$. We now transform the equations of motion to a frame moving to the right in the positive direction with uniform speed C so that

$$x' = x - Ct$$
$$z' = z$$
$$t' = t$$

gives the transformation from the independent variables in the rest frame to those in the moving frame (denoted by primed variables). Formally, the equations of motion and the boundary conditions remain invariant in form under this transformation, provided that the dynamical variables are now interpreted as <u>relative</u> to the new moving origin. At a given point in space and time, measured by $(\underset{\sim}{x}', t')$ and $(\underset{\sim}{x}, t)$ in the moving and rest frames respectively, the velocities $\underset{\sim}{u}'(\underset{\sim}{x}', t')$ and $\underset{\sim}{u}(\underset{\sim}{x}, t)$ are recorded

Reproduced with permission of the copyright owner. Further reproduction prohibited without permission.

by observers fixed to the respective frames. These two are then related by

$$\underset{\sim}{u}'(\underset{\sim}{x}', t') = \underset{\sim}{u}(\underset{\sim}{x}, t) - \underset{\sim}{C}$$

Now we wish to consider a finite amplitude irrotational gravity wave (Stokes wave) in deep water as the basic flow for this problem. In the moving frame just introduced, the gravity wave profile is stationary. Kinsman (1965, Ch.5.2) gives a detailed discussion of the Stokes wave and shows that the stream function for the deep water Stokes wave is given by

$$\frac{\psi'}{C} = -z' + \beta e^{Kz'} \cos Kx'$$

in a frame translating with uniform velocity C in the positive direction. The free surface, which occurs at $\psi' = 0$, is seen to be given by the implicit relation

$$z' = \beta e^{Kz'} \cos Kx'$$

Kinsman shows further that, correct to the third order in β,

$$z' = \tfrac{1}{2} K\beta^2 + \beta\left(1 + \tfrac{9}{8} K^2\beta^2\right)\cos Kx' + \tfrac{1}{2} K\beta^2 \cos 2Kx' + \tfrac{3}{8} K^2\beta^3 \cos 3Kx'$$

and that this profile is trochoidal to third order. Also, the phase speed is given by

$$C^2 = g/K\left(1 + \beta^2 K^2\right) \qquad \text{to third order.}$$

Higher order expansions in β are possible; Kinsman considers a fourth order expansion and derives corrections to the above expressions. In the present problem, we will use

$$z' = \beta e^{Kz'} \cos Kx'$$

Reproduced with permission of the copyright owner. Further reproduction prohibited without permission.

as the profile of the basic irrotational finite amplitude gravity wave. As will be shown presently, there exists an orthogonal curvilinear transformation to (ξ', η') coordinates in which $\eta' = 0$ corresponds to the surface $z' = \beta e^{Kz'} \cos Kx'$. This greatly facilitates examination of motions occurring in the vicinity of the long wave surface and avoids the difficulties associated with Hasselmann's (1971) analysis.

Before proceeding any further, we make the equations of motion dimensionless using K^{-1} and Ω^{-1} as reference length and time scales. Unprimed variables are used to denote dimensionless variables in the relative (moving) frame.

Let
$$x = Kx' \quad , \quad z = Kz'$$
$$t = \Omega t'$$
$$u = u'/(\Omega/K)$$
$$p = p'/(\Omega/K)^2$$

Then the equations of motion become

$$\frac{\partial u}{\partial t} + \frac{\partial}{\partial x}(u^2) + \frac{\partial}{\partial z}(uw) + \frac{\partial p}{\partial x} = R^{-1}\left(\frac{\partial^2 u}{\partial x^2} + \frac{\partial^2 u}{\partial z^2}\right)$$

Similarly, where $R = \frac{K^{-1}}{\nu_w}\left(\frac{\Omega}{K}\right)$

$$\frac{\partial w}{\partial t} + \frac{\partial}{\partial x}(uw) + \frac{\partial}{\partial z}(w^2) + \frac{\partial p}{\partial z} = R^{-1}\left(\frac{\partial^2 w}{\partial x^2} + \frac{\partial^2 w}{\partial z^2}\right)$$

$$\frac{\partial u}{\partial x} + \frac{\partial w}{\partial z} = 0$$

We had

$$\frac{DF'}{Dt'} = \frac{\partial F'}{\partial t'} + u' \frac{\partial F'}{\partial x'} + w' \frac{\partial F'}{\partial z'} = 0 \qquad \text{at the}$$

free surface $F'(x', z', t') = z' - S'(x', t')$. If the surface $F'(x', z', t') = 0$ transforms to $F(x, z, t) = 0$, then the chain

Reproduced with permission of the copyright owner. Further reproduction prohibited without permission.

rule yields

$$\Omega \frac{\partial F}{\partial t} + K\left(\frac{\Omega}{K}\right) u \frac{\partial F}{\partial x} - K\left(\frac{\Omega}{K}\right) \frac{\partial F}{\partial z} = 0$$

at the free surface. Therefore letting $F(x,z,t) = z - f(x,t)$ we have, at the free surface

$$\frac{\partial f}{\partial t} + u \frac{\partial f}{\partial x} - w = 0$$

as the consistent dimensionless free surface kinematic boundary condition in the moving frame.

Transforming the pressure boundary condition we have

$$\left(\frac{\Omega}{K}\right)^2 p - K^{-1} g z - \gamma \frac{K^2}{K} \frac{f_{xx}}{(1 + \frac{K^2}{K^2} f_x^2)^{3/2}} = \left(\frac{\Omega}{K}\right)^2 p^a$$

i.e.

$$p - \frac{g}{(\Omega^2/K)} z - \frac{\gamma}{(\Omega^2/K^3)} \frac{f_{xx}}{(1 + f_x^2)^{3/2}} = p^a$$

Defining

$$g^* = \frac{g}{(\Omega^2/K)} \sim O(1) \quad , \quad \gamma^* = \frac{\gamma}{(\Omega^2/K^3)} \sim o(1)$$

we have the dimensionless form

$$p - g^* z - \gamma^* \frac{f_{xx}}{(1 + f_x^2)^{3/2}} = p^a \qquad \text{on } z = f(x,t)$$

Finally, the tangential stress condition at the free surface becomes

$$\nu_\omega \frac{\Omega}{K} \cdot \frac{1}{K} \frac{\partial u}{\partial z} = \left(\frac{\Omega}{K}\right)^2 u_*^2$$

i.e.

$$R^{-1} \frac{\partial u}{\partial z} = u_*^2 \qquad \text{on } z = f(x,t)$$

where

$$R = \frac{\left(\frac{\Omega}{K}\right)\left(\frac{1}{K}\right)}{\nu_\omega}$$

We now wish to examine the effect of short wavelength, two-dimensional ripples riding on the long gravity carrier wave. The

Reproduced with permission of the copyright owner. Further reproduction prohibited without permission.

ripples are not necessarily "locked in" with the long wave phase and may move relative to the carrier.

Based on the earlier choice of long wave profile

$$z' = \beta e^{Kz'} \cos Kx'$$

which becomes, in dimensionless form,

$$\frac{z}{K} = \beta e^{K\left(\frac{z}{K}\right)} \cos K\left(\frac{x}{K}\right)$$

or

$$z = a e^{z} \cos x$$

where $a = \beta K$ is the long wave slope.

We transform to the orthogonal curvilinear coordinate system given by

$$\xi = x - a e^{z} \sin x$$
$$\eta = z - a e^{z} \cos x$$

which yields the original surface

$$z = a e^{z} \cos x$$

for $\eta = 0$ where ξ is a coordinate running along the free surface. For large depths $(-z)$, the constant (ξ,η) lines asymptote to constant (x,z) lines.

Using this coordinate system in the relative frame, the ripple field can be readily defined and is amenable to rigorous treatment. As a preliminary, certain fundamental properties of the transformation will be discussed.

The condition for orthogonality is that

$$\xi_x \eta_x + \xi_z \eta_z = 0 \quad \text{(Courant II, p.126)}$$

Here

$$\begin{bmatrix} \xi_x & \eta_x \\ \xi_z & \eta_z \end{bmatrix} = \begin{bmatrix} 1 - a e^{z} \cos x & a e^{z} \sin x \\ -a e^{z} \sin x & 1 - a e^{z} \cos x \end{bmatrix}$$

Reproduced with permission of the copyright owner. Further reproduction prohibited without permission.

and so the orthogonality condition is clearly satisfied. The Jacobian of the transformation is given by

$$J = \begin{vmatrix} \xi_x & \eta_x \\ \xi_z & \eta_z \end{vmatrix} = 1 - 2ae^{z}\cos x + a^2 e^{2z}$$

For values of a of interest in this analysis, namely $0 < a < 0.5$, $J \neq 0$ and the implicit function theorem (Courant II, p.152) guarantees that the original transformation is invertible.

As is shown in Appendix I,

$$x = \xi + ae^{\eta}\sin\xi + a^2 e^{2\eta}\sin 2\xi + O(a^3)$$

$$z = \eta + ae^{\eta}\cos\xi + a^2 e^{2\eta}\cos 2\xi + O(a^3)$$

From these, we have

$$dx = \frac{\partial x}{\partial \xi}d\xi + \frac{\partial x}{\partial \eta}d\eta = (1 + ae^{\eta}\cos\xi + O(a^2))d\xi + (ae^{\eta}\sin\xi + O(a^2))d\eta$$

$$dz = \frac{\partial z}{\partial \xi}d\xi + \frac{\partial z}{\partial \eta}d\eta = (-ae^{\eta}\sin\xi + O(a^2))d\xi + (1 + ae^{\eta}\cos\xi + O(a^2))d\eta$$

$$dx^2 + dz^2 = (1 + 2ae^{\eta}\cos\xi + a^2 e^{2\eta} + O(a^3))(d\xi^2 + d\eta^2)$$

$$= h_1^2 d\xi^2 + h_2^2 d\eta^2$$

$$\therefore h_1 = h_2 = h = (1 + 2ae^{\eta}\cos\xi + a^2 e^{2\eta} + O(a^3))^{1/2}$$

According to Milne-Thomson (Theoretical Hydrodynamics, p.65) the two-dimensional equations of motion in orthogonal curvilinear coordinate systems are given (for $h_1 = h_2 = h$) by the following set of equations. The velocity components (u, w) are now the components in the (ξ, η) directions.

$$\frac{\partial u}{\partial t} + \frac{u}{h}\frac{\partial u}{\partial \xi} + \frac{w}{h}\frac{\partial u}{\partial \eta} + \frac{w}{h^2}\left(u\frac{\partial h}{\partial \eta} - w\frac{\partial h}{\partial \xi}\right) + \frac{1}{h}\frac{\partial p}{\partial \xi}$$

$$= R^{-1}/h^3\left[\frac{\partial^2}{\partial \xi^2}(uh) + \frac{\partial^2}{\partial \eta^2}(uh) + 2\frac{\partial h}{\partial \eta}\left(\frac{\partial}{\partial \xi}(hw) - \frac{\partial}{\partial \eta}(hu)\right)\right]$$

$$\frac{\partial w}{\partial t} + \frac{u}{h}\frac{\partial w}{\partial \xi} + \frac{w}{h}\frac{\partial w}{\partial \eta} + \frac{u}{h^2}\left(w\frac{\partial h}{\partial \xi} - u\frac{\partial h}{\partial \eta}\right) + \frac{1}{h}\frac{\partial p}{\partial \eta}$$

$$= R^{-1}/h^3\left[\frac{\partial^2}{\partial \xi^2}(wh) + \frac{\partial^2}{\partial \eta^2}(wh) + 2\frac{\partial h}{\partial \xi}\left(\frac{\partial}{\partial \eta}(hu) - \frac{\partial}{\partial \xi}(hw)\right)\right]$$

Reproduced with permission of the copyright owner. Further reproduction prohibited without permission.

$$\frac{1}{h^2}\left[\frac{\partial}{\partial\xi}(uh)+\frac{\partial}{\partial\eta}(wh)\right]=0$$

At the free surface $\eta=f(\xi,t)$,

$$\frac{\partial f}{\partial t}+\frac{u}{h}\frac{\partial f}{\partial\xi}-\frac{w}{h}=0 \qquad \text{on } \eta=f(\xi,t)$$

Also, the pressure boundary condition at $\eta=f(\xi,t)$ is given by

$$p-g(\eta+ae^{\eta}\cos\xi+O(a^2))-\frac{\gamma f_{\xi\xi}(1+O(a))}{(1+f_\xi^2)^{3/2}} \qquad \text{on } \eta=f(\xi,t)$$

where the expression for the curvature in (ξ,η) coordinates is derived in Appendix II. Finally, the tangential stress boundary condition is given by

$$R^{-1}\frac{\partial}{\partial\eta}\left(\frac{u}{h}\right)=\omega_*^2 \qquad \text{on } \eta=f(\xi,t)$$

We now examine the dynamics of the ripples riding on the surface of the long gravity wave by considering the influence of the ripples to be confined to a thin layer at the mean (long wave) surface. This allows the techniques of matched asymptotic expansions [see Van Dyke (1964) for a general exposition] to be used to determine the modifications to the mean flow (gravity wave) free surface boundary conditions induced by the ripple layer flow.

We now recall the earlier discussion in the Introduction where it had been postulated that

(a) the characteristic ratio of ripple wavelength to gravity wavelength is assumed to be a very small number, ϵ.

(b) the characteristic ratio of ripple amplitude to gravity wave amplitude is assumed to be very small, at most of order ϵ.

Reproduced with permission of the copyright owner. Further reproduction prohibited without permission.

(c) (a) and (b) then imply that the characteristic ripple and gravity wave slopes are generally of the same order of magnitude, neither necessarily being infinitesimal.

(d) the characteristic ripple phase speed may be of the same order of magnitude as the maximum orbital speeds associated with the gravity wave field.

These specifications provide the orders of magnitudes to be built into the analysis which follows. All variables are made O(1) so that the order of magnitude of each term is reflected by the magnitude of its coefficient.

In modelling the ripple layer, we will assume that slowly varying wavetrain theory [see Whitham (1970)] is applicable. According to this theory, the structure of the ripple layer surface is expressed in terms of an amplitude function which varies significantly only over the long wave scale and a phase function which varies rapidly over the long wave scale. The phase function determines the local dispersion relation for the ripples.

In the ripple layer we will assume that the dynamical variables depend explicitly on:

(a) a magnified "lateral" coordinate $\xi' = \xi/\varepsilon$ over which the ripple phase function experiences O(1) changes in magnitude.

(b) an unstretched "lateral" coordinate $\hat{\xi} = \xi$ over which the ripple amplitude function experiences O(1) changes in magnitude.

(c) a magnified "vertical" coordinate $\eta' = \eta/\varepsilon$ over which the vertical (η) structure of the ripple field possesses O(1) changes

Reproduced with permission of the copyright owner. Further reproduction prohibited without permission.

in magnitude.

No dependence on an unstretched η coordinate is included as the problem has been set up so that the ripple layer exists at the fixed surface $\eta = 0$ ——— the long wave motion is in essence frozen over the depth of the ripple layer.

The temporal dependence of the dynamical variables will now be considered. The ripple structure in the moving frame is shown [see fig. (1)] in relation to the orbital velocity distribution of the long wave and the basic convection velocity induced by the moving frame of reference. These underlying currents and the associated mean pressure are assumed to be constant across the ripple layer and are assumed to be the analytic continuations of the respective interior flow quantities extended above the upper boundary of the interior flow. This is a natural first order approximation enabling calculation of the first order ripple layer flow. This can then be used to calculate the first order modifications to the interior flow. The analytic continuation of the adjusted interior flow forms the revised mean flow for the ripple layer and so on, in principle allowing calculation to any desired order of accuracy. Only the first order corrections to the interior flow will be derived here.

In the relative frame, the amplitude function for the ripple structure is considered to be statistically (or actually) steady in time and will vary over timescales long compared to the long wave period. We denote the slowly varying time variable by

Reproduced with permission of the copyright owner. Further reproduction prohibited without permission.

$\hat{t} = \varepsilon^N t$ where $N > 1$. On the other hand, the local temporal fluctuations in the ripple structure as the ripple train moves past a given long wave phase point ($\hat{\xi}$) occur rapidly compared to the long wave period. To lowest order, this may be seen by remarking that the ripples appear to be moving to the left with the resultant of the convective velocity of the frame to the left and the still-water ripple phase speed to the right (neglecting wind drift). The magnitude of this apparent convective velocity to the left is of the same order or greater than the ripple phase speed in still water for the conditions under which the 'maser' theory might be expected to apply. Thus to lowest order, the apparent ripple frequency observed in the relative frame will be given by the vector difference between these two velocities divided by the ripple wavelength. This simplified argument suffices to justify the assumption of a fast time $t' = t/\varepsilon$.

We now use the independent variables just specified to obtain the dominant equations of motion for the fluctuating ripple layer flow. The dependent variables are rescaled according to the orders of magnitude inferred from the postulated 'maser' mechanism, so that all variables are O(1) and the magnitude of each term is reflected by the order of magnitude of its coefficient. At this point we will ignore viscous effects to concentrate on the inviscid problem. The rapidly fluctuating quantities associated with the ripple motion are then given by

Reproduced with permission of the copyright owner. Further reproduction prohibited without permission.

$$u(\xi,\eta,t) = a u'(\xi',\eta',t',\hat{\xi},\hat{t})$$

$$w(\xi,\eta,t) = a w'(\xi',\eta',t',\hat{\xi},\hat{t})$$

$$p(\xi,\eta,t) = a^2 p'(\xi',\eta',t',\hat{\xi},\hat{t})$$

$$\eta' = a\zeta'(\xi',t',\hat{\xi},\hat{t}) \quad \text{[ripple layer free surface]}$$

These scalings reflect the assumptions that:

(a) the ripple layer velocities are comparable to the long wave phase speed times the long wave slope.

(b) the ripple slopes are of the same order of magnitude as the long wave slopes.

(c) the pressure field is scaled consistently with the velocity field scaling.

(d) the mean currents and pressures not associated with the rapidly varying ripple field have been subtracted out, in accordance with the reasoning given above.

We begin by considering the continuity equation and the kinematic free surface boundary condition in terms of the new independent variables. From the chain rule

$$\frac{\partial}{\partial\xi} \to \frac{1}{\varepsilon}\frac{\partial}{\partial\xi'} + \frac{\partial}{\partial\hat{\xi}} \; ; \qquad \frac{\partial}{\partial\eta} \to \frac{1}{\varepsilon}\frac{\partial}{\partial\eta'} \; ; \; \frac{\partial}{\partial t} \to \frac{1}{\varepsilon}\frac{\partial}{\partial t'} + \varepsilon^N \frac{\partial}{\partial\hat{t}}$$

The continuity equation transforms to

$$\frac{a}{\varepsilon}\frac{\partial}{\partial\xi'}(hu') + a\frac{\partial}{\partial\hat{\xi}}(hu') + \frac{a}{\varepsilon}\frac{\partial}{\partial\eta'}(hw') = 0$$

where

$$h = 1 + ae^{\varepsilon\eta'}\cos\hat{\xi} + O(a^2)$$

Reproduced with permission of the copyright owner. Further reproduction prohibited without permission.

Expanding and multiplying throughout by $\frac{\varepsilon h}{a}$ gives

$$\frac{\partial u'}{\partial \xi'} + \frac{\partial w'}{\partial \eta'} = -\varepsilon \frac{\partial u'}{\partial \hat{\xi}} - \frac{\varepsilon}{h} u' \frac{\partial h}{\partial \hat{\xi}} - \frac{1}{h} w' \frac{\partial h}{\partial \eta'}$$

Now $h = 1 + a e^{\varepsilon \eta'} \cos \hat{\xi} + O(a^2)$ so we have

$$\frac{\partial h}{\partial \xi} = -a e^{\varepsilon \eta'} \sin \hat{\xi} + O(a^2)$$

$$\frac{\partial h}{\partial \eta} = \varepsilon \left(a e^{\varepsilon \eta'} \cos \hat{\xi} + O(a^2) \right)$$

$$\therefore \frac{\partial u'}{\partial \xi'} + \frac{\partial w'}{\partial \eta'} = -\varepsilon \frac{\partial u'}{\partial \hat{\xi}} + \varepsilon a \left(u' \sin \hat{\xi} - w' \cos \hat{\xi} \right) e^{\varepsilon \eta'} + O(a^2 \varepsilon) \quad \ldots.(3.6)$$

We now wish to integrate across the ripple layer down from the free surface to the outer edge of the ripple layer $\eta' \to -\infty$ (where the ripple layer "merges" into the interior flow). Using the formula for differentiating integrals with variable limits, we then have

$$\frac{\partial}{\partial \xi'} \int_{-\infty}^{a\zeta'} u' \, d\eta' - a u'(a\zeta') \frac{\partial \zeta'}{\partial \xi'} + w'(a\zeta') - w'(-\infty)$$

$$= -\varepsilon \frac{\partial}{\partial \hat{\xi}} \int_{-\infty}^{a\zeta'} u' \, d\eta' + \varepsilon a u'(a\zeta') \frac{\partial \zeta'}{\partial \hat{\xi}}$$

$$+ a\varepsilon \sin \hat{\xi} \int_{-\infty}^{a\zeta'} u' e^{\varepsilon \eta'} d\eta' - a\varepsilon \cos \hat{\xi} \int_{-\infty}^{a\zeta'} w' e^{\varepsilon \eta'} d\eta' \quad \ldots.(3.7)$$

We now define averages for the ripple layer as ensemble or probability averages taken at fixed phase points ($\hat{\xi}$) with respect to the long wave and fixed times ($\hat{t}$) with respect to the possible slow development of the long wave. In accordance with the slowly varying wavetrain assumption, the ripples are

Reproduced with permission of the copyright owner. Further reproduction prohibited without permission.

regarded as locally homogeneous. With respect to the "magnified" ripple layer variables ξ' and t', the ripple field is statistically (or actually) stationary so that for any quantity $\gamma(\xi', t', \hat{\xi}, \hat{t})$

$$\overline{\frac{\partial}{\partial \xi'} \gamma(\xi', t', \hat{\xi}, \hat{t})} = \overline{\frac{\partial}{\partial t'} \gamma(\xi', t', \hat{\xi}, \hat{t})} = 0$$

while

$$\overline{\frac{\partial}{\partial \hat{\xi}} \gamma(\xi', t', \xi, \hat{t})} = \frac{\partial}{\partial \xi} \overline{\gamma(\xi', t', \hat{\xi}, \hat{t})}$$

$$\overline{\frac{\partial}{\partial \hat{t}} \gamma(\xi', t', \hat{\xi}, \hat{t})} = \frac{\partial}{\partial \hat{t}} \overline{\gamma(\xi', t', \xi, \hat{t})}$$

The kinematic free surface boundary condition for the ripple surface $\eta' = a\zeta'(\xi', t', \hat{\xi}, \hat{t})$ is given by

$$\frac{\partial \zeta'}{\partial t'} + a\varepsilon^N \frac{\partial \zeta'}{\partial \hat{t}} + \frac{a^2}{\varepsilon h} u'(a\zeta') \frac{\partial \zeta'}{\partial \xi'} + \frac{a^2}{h} u'(a\zeta') \frac{\partial \zeta'}{\partial \hat{\xi}} - a w'(a\zeta') = 0$$

where $h = 1 + a\varepsilon^N \eta' \cos \hat{\xi}$ is evaluated at $\eta' = a\zeta'$

i.e. $$h\varepsilon^{N+1} \frac{\partial \zeta'}{\partial \hat{t}} + h \frac{\partial \zeta'}{\partial t'} + a u'(a\zeta') \frac{\partial \zeta'}{\partial \xi'} + a\varepsilon u'(a\zeta') \frac{\partial \zeta'}{\partial \hat{\xi}} - w'(a\zeta') = 0 \quad \ldots\ldots (3.8)$$

Taking the average as defined above, we have

$$h\varepsilon^{N+1} \frac{\partial \bar{\zeta}'}{\partial \hat{t}} + a \overline{u'(a\zeta') \frac{\partial \zeta'}{\partial \xi'}} - \overline{w'(a\zeta')} = -a\varepsilon \overline{u'(a\zeta') \frac{\partial \zeta'}{\partial \hat{\xi}}}$$

since $\overline{\frac{\partial}{\partial t'}(\zeta')} = 0$

The average of the integrated continuity equation (3.7) gives

$$\overline{\frac{\partial}{\partial \xi'} \int_{-\infty}^{a\zeta'} u' \, d\eta'} - \overline{a u'(a\zeta') \frac{\partial \zeta'}{\partial \xi'}} + \overline{w'(a\zeta')} - \overline{w'(-\infty)}$$

$$= -\varepsilon \frac{\partial}{\partial \hat{\xi}} \overline{\int_{-\infty}^{a\zeta'} u' \, d\eta'} + \varepsilon a \overline{u'(a\zeta') \frac{\partial \zeta'}{\partial \hat{\xi}}}$$

$$+ a\varepsilon \sin\hat{\xi} \overline{\int_{-\infty}^{a\zeta'} u' e^{\varepsilon\eta'} d\eta'} - a\varepsilon \cos\hat{\xi} \overline{\int_{-\infty}^{a\zeta'} w' e^{\varepsilon\eta'} d\eta'}$$

$$+ \ldots .$$

Reproduced with permission of the copyright owner. Further reproduction prohibited without permission.

whence, with (3.8) and the averaging properties specified above we have

$$\overline{w'(\hat{\xi},\hat{t},-\infty)} = \varepsilon \frac{\partial}{\partial \hat{\xi}} \overline{\int_{-\infty}^{a\zeta'} u' d\eta'} + \varepsilon^{N+1} \frac{\partial \bar{\zeta}'}{\partial \hat{t}} - a\varepsilon \sin\hat{\xi} \overline{\int_{-\infty}^{a\zeta'} u' e^{\varepsilon\eta'} d\eta'} + a\varepsilon \cos\hat{\xi} \overline{\int_{-\infty}^{0} \omega' e^{\varepsilon\eta'} d\eta'}$$

so that

$$\overline{w'(\hat{\xi},\hat{t},-\infty)} = \varepsilon \frac{\partial}{\partial \hat{\xi}} \overline{\int_{-\infty}^{a\zeta'} u' d\eta'} + O(a\varepsilon) \quad \ldots. (3.9)$$

where ε is the characteristic wavelength ratio, a is the long wave slope and $0 < \varepsilon < a$.

Thus variations in the ripple structure over the long wave phase induce a "vertical" (η) mean velocity component at the outer edge of the ripple layer proportional to the large-scale "horizontal" (ξ) gradient of the integrated mass flux velocity. Formally, in the asymptotic limit as $\varepsilon \to 0$, this corresponds to a mean velocity component normal to the interior flow boundary $\eta = 0$. Thus the inviscid kinematic boundary condition for the long waves $W(0) = 0$ in the absence of ripples is replaced by the asymptotic result

$$W(\hat{\xi},\hat{t},0) = \varepsilon \frac{\partial}{\partial \hat{\xi}} \overline{\int_{-\infty}^{a\zeta'} u' d\eta'} + O(a\varepsilon) \quad \ldots.(3.10)$$

Next we use the "vertical" (η) momentum equation to determine the modifications to the pressure boundary condition. Beginning with the form appropriate to our frame of reference and to the curvilinear coordinate system i.e.

$$\frac{\partial w}{\partial t} + \frac{u}{h}\frac{\partial w}{\partial \xi} + \frac{w}{h}\frac{\partial w}{\partial \eta} + \frac{1}{h}\frac{\partial p}{\partial \eta} - \frac{u}{h^2}\left(u\frac{\partial h}{\partial \eta} - w\frac{\partial h}{\partial \xi}\right) = 0$$

Reproduced with permission of the copyright owner. Further reproduction prohibited without permission.

we substitute the ripple layer variables to obtain

$$\frac{a}{\varepsilon}\frac{\partial w'}{\partial t'} + a\varepsilon^{\nu}\frac{\partial w'}{\partial \xi'} + \frac{a^2}{\varepsilon}\frac{u'}{h}\frac{\partial w'}{\partial \xi'} + \frac{a^2}{h}u'\frac{\partial w'}{\partial \xi'} + \frac{a^2}{h}w'\frac{\partial w'}{\partial \eta'} + \frac{1}{\varepsilon}\frac{a^2}{h}\frac{\partial p'}{\partial \eta'}$$

$$= \frac{a^2 u'}{h^2}\left(u'\frac{\partial h}{\partial \eta'} - w'\frac{\partial h}{\partial \xi'}\right)$$

Multiplying throughout by $\varepsilon h/a$ we have

$$h\frac{\partial w'}{\partial t'} + au'\frac{\partial w'}{\partial \xi'} + aw'\frac{\partial w'}{\partial \eta'} + a\frac{\partial p'}{\partial \eta'} = -a\varepsilon u'\frac{\partial w'}{\partial \xi'} - h\varepsilon^{\nu}\frac{\partial \zeta'}{\partial t'} + O(a^2\varepsilon)$$

From the continuity equation (3.6) derived earlier, we had

$$\frac{\partial u'}{\partial \xi'} = -\frac{\partial w'}{\partial \eta'} - \varepsilon\frac{\partial u'}{\partial \xi'} + O(a\varepsilon)$$

We rewrite the left hand side of the momentum equation in the form

$$h\frac{\partial w'}{\partial t'} + a\frac{\partial}{\partial \xi'}(w'u') - aw'\frac{\partial u'}{\partial \xi'} + a\frac{\partial}{\partial \eta'}\left(\frac{w'^2}{2}\right) + a\frac{\partial p'}{\partial \eta'} = -a\varepsilon u'\frac{\partial w'}{\partial \xi'} + O(a^2\varepsilon)$$

which becomes, on using (3.6) to replace $\frac{\partial u'}{\partial \xi'}$:

$$h\frac{\partial w'}{\partial t'} + a\frac{\partial}{\partial \xi'}(w'u') + a\frac{\partial}{\partial \eta'}(w'^2) + a\frac{\partial p'}{\partial \eta'}$$

$$= -a\varepsilon u'\frac{\partial w'}{\partial \xi'} - a\varepsilon w'\frac{\partial u'}{\partial \xi'} + O(a^2\varepsilon)$$

$$= -a\varepsilon\frac{\partial}{\partial \xi'}(u'w') + O(a^2\varepsilon) \qquad \ldots.(3.11)$$

We now wish to integrate from $\eta' = -\infty$ to $\eta' = a\zeta'$ and use the formula for differentiating integrals with variable limits to obtain quantities involving derivatives of integrals of ripple layer variables. However, we first note that the first term in (3.11)

Reproduced with permission of the copyright owner. Further reproduction prohibited without permission.

$$\int_{-\infty}^{a\zeta'} h \frac{\partial w'}{\partial t'} d\eta' = \int_{-\infty}^{a\zeta'} \frac{\partial}{\partial t'}(hw')\, d\eta' \qquad (h = 1 + a e^{\varepsilon\eta'}\cos\hat{\xi} \neq h(t))$$

$$= \frac{\partial}{\partial t'} \int_{-\infty}^{a\zeta'} hw'\, d\eta' - a(hw')|_{a\zeta'} \frac{\partial \zeta'}{\partial t'}$$

So we have

$$\frac{\partial}{\partial t'} \int_{-\infty}^{a\zeta'} hw'\, d\eta' - a(hw')|_{a\zeta'} \frac{\partial \zeta'}{\partial t'} + a \frac{\partial}{\partial \xi'} \int_{-\infty}^{a\zeta'} w'u'\, d\eta' - a^2 w'(a\zeta') u'(a\zeta') \frac{\partial \zeta'}{\partial \xi'}$$

$$+ a w'^2(a\zeta') - a w'^2(-\infty) + a p'(a\zeta') - a p'(-\infty) = -a\varepsilon \frac{\partial}{\partial \hat{\xi}} \int_{-\infty}^{a\zeta'} u'w'\, d\eta' + a^2\varepsilon\, u'(a\zeta) w'(a\zeta') \frac{\partial \zeta'}{\partial \xi'} + O(a^2\varepsilon)$$

i.e. $$\frac{\partial}{\partial t'} \int_{-\infty}^{a\zeta'} hw'\, d\eta' + a \frac{\partial}{\partial \xi'} \int_{-\infty}^{a\zeta'} w'u'\, d\eta' + a p'(a\zeta') - a p'(-\infty) - a w'^2(-\infty)$$

$$+ a w'(a\zeta') \left\{ h|_{a\zeta'} \frac{\partial \zeta'}{\partial t'} + a u'(a\zeta') \frac{\partial \zeta'}{\partial \xi'} + a\varepsilon u'(a\zeta') \frac{\partial \zeta'}{\partial \hat{\xi}} - w'(a\zeta') \right\}$$

$$= -a\varepsilon \frac{\partial}{\partial \hat{\xi}} \int_{-\infty}^{a\zeta'} u'w'\, d\eta' + O(a^2\varepsilon)$$

But the term in parentheses vanishes by (3.8) [the higher order time derivative was discarded earlier]. So we are left with the result

$$\frac{\partial}{\partial t'} \int_{-\infty}^{a\zeta'} w'\, d\eta' + a \frac{\partial}{\partial \xi'} \int_{-\infty}^{a\zeta'} w'u'\, d\eta' + a p'(a\zeta') - a p'(-\infty) - a w'^2(-\infty)$$

$$= -a\varepsilon \frac{\partial}{\partial \hat{\xi}} \int_{-\infty}^{a\zeta'} u'w'\, d\eta' + O(a^2\varepsilon)$$

Taking the average as specified earlier, we have that

$$\overline{p'(-\infty)} = \overline{p'(a\zeta')} - \overline{w'^2(-\infty)} + \varepsilon \frac{\partial}{\partial \hat{\xi}} \overline{\int_{-\infty}^{a\zeta'} u'w'\, d\eta'} + O(a\varepsilon) \qquad \ldots.(3.12)$$

But the fluctuations in w' vanish as $\eta' \to -\infty$, so that by (3.10)

$$\overline{w'^2(-\infty)} \sim (\overline{w'})^2 \sim O(\varepsilon^2) \qquad \ldots..(3.13)$$

Reproduced with permission of the copyright owner. Further reproduction prohibited without permission.

We now recall the dimensionless pressure boundary condition derived earlier for general (ξ, η) coordinates

$$P(\eta) - g(\eta + ae^{\eta}\cos\xi + O(a^2)) - \frac{\gamma\, \zeta_{\xi\xi}(1+O(a))}{(1+\zeta_\xi^2)^{3/2}} = p^a \quad \text{on} \quad \eta = \zeta(\xi,t)$$

We recall that g, γ were made dimensionless using the long wave frequency and wave number as the basis for the reference time and length scales. This choice of scalings rendered

$g = O(1)$ and $\gamma = o(1)$.

In terms of the ripple layer variables, this transforms as follows:

$$p(\zeta) \longrightarrow a^2 p'(a\zeta')$$

$$\eta \longrightarrow \varepsilon\eta'$$

$$\therefore \quad \zeta(\xi,t) \longrightarrow a\varepsilon\zeta'(\xi',t',\hat{\xi},\hat{t})$$

i.e. $$\eta = \zeta \longrightarrow \eta' = a\zeta'$$

So
$$\zeta_\xi \longrightarrow a\zeta'_{\xi'} + \varepsilon a\zeta'_{\hat{\xi}}$$

$$\zeta_{\xi\xi} \longrightarrow \frac{a}{\varepsilon}\zeta'_{\xi'\xi'} + \varepsilon a\zeta'_{\hat{\xi}\hat{\xi}}$$

Hence the transformed pressure boundary condition in the ripple layer is

$$a^2 p'(a\zeta') = g(\varepsilon\eta' + ae^{\varepsilon\eta'}\cos\hat{\xi} + O(a^2)) + \gamma\left(\frac{\frac{a}{\varepsilon}\zeta'_{\xi'\xi'} + \varepsilon a\zeta'_{\hat{\xi}\hat{\xi}} + O(a^2\varepsilon)}{\{1+(a\zeta'_{\xi'} + \varepsilon a\zeta'_{\hat{\xi}})^2\}^{3/2}}\right) + a^2 p^a \quad \text{on} \quad \eta' = a\zeta'$$

Reproduced with permission of the copyright owner. Further reproduction prohibited without permission.

So we have

$$a^2 p'(a\zeta') = g\{\varepsilon a\zeta' + a\varepsilon^2 a\zeta' \cos\hat{\xi} + O(a^3)\} + \gamma\frac{a}{\varepsilon}\{\zeta_{\xi'\xi'} + \varepsilon^2\zeta_{\xi\xi} + O(a\varepsilon^2)\} + a^2 p^a$$

$$= g\{\varepsilon a\zeta' + a\cos\hat{\xi} + a^2\varepsilon\zeta'\cos\hat{\xi} + O(a^3)\}$$

$$+ \frac{\gamma a}{\varepsilon}\{\zeta_{\xi'\xi'} + \varepsilon^2\zeta'_{\hat{\xi}\hat{\xi}} + O(a\varepsilon^2)\}(1 + O(a^2)) + a^2 p^a$$

The second term on the right hand side, $ga\cos\hat{\xi}$ and p^a are not associated with the fluctuating short wave flow and will be subtracted out. Then before we take the average of both sides to obtain $\overline{p'(a\zeta')}$, we note that if gravity and surface tension are to be of comparable importance for the short waves, then we must have

$$\varepsilon a g \sim \gamma\frac{a}{\varepsilon}$$

i.e.
$$\gamma \sim \varepsilon^2 g = O(\varepsilon^2)$$

i.e. the surface tension parameter must be considered an $O(\varepsilon^2)$ quantity. Now proceeding to take the average of the pressure condition equation above (having subtracted out the terms p^a and $ga\cos\hat{\xi}$) we obtain

$$a^2\overline{p'(a\zeta')} = g\{\varepsilon a\overline{\zeta'} + a^2\varepsilon\,\overline{\zeta'\cos\hat{\xi}} + \varepsilon^2\frac{a^3}{2}\overline{\zeta'^2\cos\hat{\xi}} + O(\varepsilon^3 a^4)\}$$

$$+ \gamma\frac{a}{\varepsilon}\{\overline{\zeta}_{\xi'\xi'} + \varepsilon^2\overline{\zeta}_{\xi\xi} + O(a\varepsilon^2)\}$$

Since $\overline{\zeta'} = \overline{\zeta}_{\xi\xi'} = 0$ we have the result that

$$a^2\overline{p'(a\zeta')} = a^3\varepsilon g\,\overline{\zeta'^2\cos\hat{\xi}} + \gamma\varepsilon a\overline{\zeta}_{\xi\xi}$$

+ higher order terms

Reproduced with permission of the copyright owner. Further reproduction prohibited without permission.

i.e. $$\overline{p'(a\varsigma')} = O(a\varepsilon) \qquad \ldots\ldots (3.14)$$

Hence the final result for the mean pressure difference induced by the short wave field is given by using (3.13) and (3.14) in (3.12) yielding

$$\overline{p'(-\infty)} = \varepsilon \frac{\partial}{\partial \hat{\xi}} \overline{\int_{-\infty}^{a\varsigma'} u'w' \, d\eta'} + O(a\varepsilon) \qquad \ldots\ldots (3.15)$$

Consequently, the mean surface pressure acting on the long waves is given by the tangential gradient of the integrated flux of the vertical momentum associated with the ripple field.

Finally, we apply the same procedure to the transverse (ξ) momentum equation

$$\frac{\partial v}{\partial t} + \frac{u}{h}\frac{\partial v}{\partial \xi} + \frac{w}{h}\frac{\partial v}{\partial \eta} + \frac{1}{h}\frac{\partial p}{\partial \xi} + \frac{vw}{h^2}\left(u\frac{\partial h}{\partial \eta} - w\frac{\partial h}{\partial \xi}\right) = 0.$$

Substituting the ripple layer variables, we obtain

$$\frac{a}{\varepsilon}\frac{\partial v'}{\partial t'} + a\varepsilon^{\nu}\frac{\partial v'}{\partial \hat{t}} + \frac{a}{\varepsilon h}u'\frac{\partial v'}{\partial \xi'} + \frac{a^2}{h}\frac{\partial v'}{\partial \hat{\xi}} + \frac{a^2}{\varepsilon h}w'\frac{\partial v'}{\partial \eta'} + \frac{a^2}{\varepsilon h}\frac{\partial p'}{\partial \xi'} + \frac{a^2}{h}\frac{\partial p'}{\partial \hat{\xi}}$$
$$= \frac{a^2}{h^2}w'\left(w'\frac{\partial h}{\partial \xi'} - \frac{u'}{\varepsilon}\frac{\partial h}{\partial \eta'}\right)$$

Multiplying throughout by $\frac{\varepsilon h}{a}$ we have

$$h\frac{\partial v'}{\partial t'} + au'\frac{\partial v'}{\partial \xi'} + aw'\frac{\partial v'}{\partial \eta'} + a\frac{\partial p'}{\partial \xi'} = -a\varepsilon u'\frac{\partial v'}{\partial \xi'} - a\varepsilon\frac{\partial p'}{\partial \hat{\xi}} + O(a^2) \ldots \qquad (3.16)$$

From the continuity equation (3.6) we had

$$\frac{\partial w'}{\partial \eta'} = -\frac{\partial u'}{\partial \xi'} - \varepsilon\frac{\partial u'}{\partial \hat{\xi}} + O(a\varepsilon) \qquad \ldots. (3.6)$$

Reproduced with permission of the copyright owner. Further reproduction prohibited without permission.

Rewriting (3.16) as

$$h\frac{\partial u'}{\partial t'} + a\frac{\partial}{\partial \xi'}\left(\frac{u'^2}{2}\right) + a\frac{\partial}{\partial \eta'}(v'w') - aw'\frac{\partial w'}{\partial \eta'} + a\frac{\partial p'}{\partial \xi'}$$
$$= -a\varepsilon w'\frac{\partial u'}{\partial \hat{\xi}} - a\varepsilon\frac{\partial p'}{\partial \hat{\xi}} + O(a^2\varepsilon)$$

and using (3.6) we obtain

$$h\frac{\partial u'}{\partial t'} + a\frac{\partial}{\partial \xi'}(u'^2) + a\frac{\partial}{\partial \eta'}(u'w') + a\frac{\partial p'}{\partial \xi'}$$
$$= -a\varepsilon\frac{\partial p'}{\partial \hat{\xi}} - a\varepsilon w'\frac{\partial u'}{\partial \hat{\xi}} - a\varepsilon w'\frac{\partial u'}{\partial \hat{\xi}} + O(a^2\varepsilon).$$
$$= -a\varepsilon\frac{\partial}{\partial \hat{\xi}}[p + u'^2] + O(a^2\varepsilon)$$

....(3.17)

Now integrate from $\eta' = -\infty$ to $\eta' = a\xi'$ and use the formula for differentiating integrals with variable limits to obtain quantities involving derivatives of integrals of the ripple layer variables. We first note that

$$\int_{-\infty}^{a\xi'} h\frac{\partial u'}{\partial t'}\,d\eta' = \frac{\partial}{\partial t'}\int_{-\infty}^{a\xi'} hu'\,d\eta' - a(hu')|_{a\xi'}\frac{\partial \xi'}{\partial t'}$$

So we have

$$\frac{\partial}{\partial t'}\int_{-\infty}^{a\xi'} hu'\,d\eta' - a(hu')|_{a\xi'}\frac{\partial \xi'}{\partial t'} + a\frac{\partial}{\partial \xi'}\int_{-\infty}^{a\xi'} u'^2\,d\eta' - a^2u'^2(a\xi')\frac{\partial \xi'}{\partial \xi'}$$
$$+ au'(a\xi')w'(a\xi') - au'(-\infty)w'(-\infty) + a\frac{\partial}{\partial \xi'}\int p'\,d\eta' - a^2p'(a\xi')\frac{\partial \xi'}{\partial \xi'}$$
$$= -a\varepsilon\frac{\partial}{\partial \hat{\xi}}\int_{-\infty}^{a\xi'}(p' + u'^2)\,d\eta' + a^2\varepsilon p'(a\xi')\frac{\partial \xi'}{\partial \hat{\xi}} + a^2\varepsilon u'^2(a\xi')\frac{\partial \xi'}{\partial \hat{\xi}} + O(a^2\varepsilon)$$

i.e.

$$\frac{\partial}{\partial t'}\int_{-\infty}^{a\xi'} hu'\,d\eta' + a\frac{\partial}{\partial \xi'}\int_{-\infty}^{a\xi'}(u'^2 + p')\,d\eta' + a^2p'(a\xi')\frac{\partial \xi'}{\partial \xi'} - au'(-\infty)w'(-\infty)$$
$$- u'(a\xi')\left\{h|_{a\xi'}\frac{\partial \xi'}{\partial t'} + au'(a\xi')\frac{\partial \xi'}{\partial \xi'} + \varepsilon au'(a\xi')\frac{\partial \xi'}{\partial \xi'} - w'(a\xi')\right\}$$
$$= -a\varepsilon\frac{\partial}{\partial \xi}\int_{-\infty}^{a\xi'}(p' + u'^2)\,d\eta' + O(a^2\varepsilon)$$

Reproduced with permission of the copyright owner. Further reproduction prohibited without permission.

But the term in parentheses { } vanishes by (3.8) [the higher order time derivative was discarded earlier]. So we are left with the result

$$\frac{\partial}{\partial t'}\int_{-\infty}^{a\zeta'} u'\,d\eta' + a\frac{\partial}{\partial \xi'}\int_{-\infty}^{a\zeta'}(u'^2+p')\,d\eta' + a^2 p'(a\zeta')\frac{\partial \zeta'}{\partial \xi'} - a u'(-\infty)w'(-\infty)$$
$$= -a\varepsilon\frac{\partial}{\partial \xi}\int_{-\infty}^{a\zeta'}(p'+w'^2)\,d\eta' + O(a^2\varepsilon)$$

Taking the average as specified earlier, we have that

$$\overline{a^2 p'(a\zeta')\frac{\partial \zeta'}{\partial \xi'}} - \overline{a u'(-\infty)w'(-\infty)} = -a\varepsilon\frac{\partial}{\partial \hat{\xi}}\overline{\int_{-\infty}^{a\zeta'}(p'+w'^2)\,d\eta'} + O(a^2\varepsilon)$$

From the discussion on p. 41, we have

$$\overline{a^2 p'(a\zeta')\frac{\partial \zeta'}{\partial \xi'}} = g\overline{\left\{\varepsilon a\zeta'\frac{\partial \zeta'}{\partial \xi'} + a^2\varepsilon\zeta'\frac{\partial \zeta'}{\partial \xi'}\cos\hat{\xi} + O(a^2\varepsilon^2)\right\}}$$
$$+ \gamma\frac{a}{\varepsilon}\overline{\left\{\zeta'_{\xi'\xi'}\frac{\partial \zeta'}{\partial \xi'} + O(\varepsilon^2)\right\}\left\{1 + a^2\zeta'^2_{\xi'} + O(a^2\varepsilon)\right\}^{-3/2}}$$

Now $\overline{\zeta'\frac{\partial \zeta'}{\partial \xi'}} = \overline{\frac{\partial}{\partial \xi'}\left(\frac{\zeta'^2}{2}\right)} = 0$

$\overline{\zeta_{\xi'\xi'}\zeta_{\xi'}} = \overline{\frac{\partial}{\partial \xi'}\left(\frac{\zeta'^2_{\xi'}}{2}\right)} = 0$

$$\therefore \overline{a^2 p'(a\zeta')\frac{\partial \zeta'}{\partial \xi'}} = O(\varepsilon^2 a^3, \varepsilon^3 a)$$

Hence we have the result

$$\overline{u'(-\infty)w'(-\infty)} = \varepsilon\frac{\partial}{\partial \xi}\overline{\int_{-\infty}^{a\zeta'}(p'+w'^2)\,d\eta'} + O(a\varepsilon) \quad \ldots. (3.18)$$

Noting that p' is the reduced kinematic pressure $P/\rho + gz$ we see that the right hand sides of equations (3.15) and (3.18) coincide to $O(a\varepsilon)$ with the ripple layer "radiation stress" components {($S_{\xi'\eta'}$, $S_{\xi'\xi'}$) respectively} defined by Longuet-Higgins

Reproduced with permission of the copyright owner. Further reproduction prohibited without permission.

and Stewart (1964). In this paper it is also shown that for small amplitude waves on deep water,

$$S_{x'y'} = 0$$

$$S_{x'x'} = E\left(\frac{1+3s}{2(1+s)}\right) \qquad \text{where} \quad s = \frac{\gamma k^2}{\rho g} \quad \text{reflects}$$

the relative importance of the capillary restoring force. γ is the surface tension and E is the energy density of the waves, given by

$$E = \tfrac{1}{2}\rho g a^2\left(1 + \frac{\gamma k^2}{\rho g}\right)$$

Thus to first order, the ripple layer transmits its dynamical influence through the tangential stress $\overline{u'(-\infty)\,w'(-\infty)}$ which is given by the tangential gradient of the normal radiation stress component $S_{x'x'}$ muliplied by the wavelength ratio ϵ. The normal stress $\overline{p'(-\infty)}$ vanishes to $O(\epsilon)$ and thus has a negligible role in the momentum transfer, under the assumption of small amplitude ripples.

Longuet-Higgins (1969a) has shown that a variable tangential stress in phase with the wave elevation is dynamically equivalent to a normal stress in phase with the wave slope. Thus the mean momentum flux to the long wave is given by the correlation between the induced ripple layer shear stress and the long wave elevation. It will be non-zero if these two quantities are in phase. The mean rate of working by the tangential stresses on the waves is given by the correlation between the induced ripple layer shear stress and the tangential component of the orbital velocity at the

Reproduced with permission of the copyright owner. Further reproduction prohibited without permission.

surface of the long wave. This will also be non-zero if the tangential stress is in phase with the long wave elevation.

The relation between these results and the observations and measurements given in §6 is discussed in §8.

Reproduced with permission of the copyright owner. Further reproduction prohibited without permission.

§ 4 THE WIND-WAVE FACILITY

The wind-wave facility consisted of a wind tunnel coupled to a wave tank [see fig. (2)]. The wind tunnel comprised a filter-covered air intake, an axial blower, an expansion section, a right-angle bend with turning vanes, a settling chamber, an 8:1 vertical contraction and a transition section coupling the tunnel to the air channel above the water surface of the wave tank. Built by Schwarz (1957), the wind tunnel was modified by Kennedy (1965), Hires (1968) and Wilson (1972). To reduce the wall jets induced by the contraction and to vigorously initiate turbulent boundary layers, Wilson attached three rows of coiled springs to both the roof and floor of the transition section just after the contraction. This provided a fully-developed turbulent channel flow in the absence of water waves at a distance of 72 channel heights from the contraction exit. For further details, the above references should be consulted.

To maintain steady mean wind conditions in the working section of the air channel of the wave tank, it was necessary to regulate the speed of the fan. The fan speed was sensed by an electromagnetic pickup and was regulated manually to $\pm$ 1.5% of the desired level by adjusting the armature and field resistances of the d.c. fan motor. The humidity of the air remained between 70 and 80 percent relative humidity. The temperature of the air stayed within the range 68.1°F to 68.8°F. It was sensed by a thermometer mounted in the airflow

Reproduced with permission of the copyright owner. Further reproduction prohibited without permission.

at the working section.

The geometry and dimensions of the wave tank used in these experiments are also shown in fig. (2). It had the same nominal size as that used by Wilson (1972) but was of necessity rebuilt due to its poor state of repair. The walls and floor of the tank were made of plate glass .25 inches and .75 inches thick respectively. The joints were sealed with RTV 108 silicone rubber (G.E.) and the glass panels were isolated from the steel framework by .125 inches thick hard neoprene rubber strips. The roof over the air channel was the set of plexiglas plates used by Wilson (1972). The wave generator was positioned 91 cm from the upwind end of the tank. It consisted of a fabricated flexible plate clamped at the bottom of the tank. Its stiffness increased with depth in three steps, so that most of the flexure occurred near the surface of the water. The plate was driven by the mechanism used by Wilson (1972) modified to provide an increased stroke capability of up to 25 cm. The wave generating system was capable of producing a coherent train of finite amplitude gravity waves of up to nearly maximum steepness over the frequency range of 1.5 Hz to 2.2 Hz. The frequency of the driving mechanism was monitored by a photocell which registered the frequency of light interruptions induced by a rotating aperture disk attached to the drive shaft. With this system, a preset wavemaker frequency could be maintained within $\pm$ 0.2%. Absorbing beaches were installed at both ends of the tank. The upwind beach was present to prevent water from sloshing into the wind tunnel and

Reproduced with permission of the copyright owner. Further reproduction prohibited without permission.

to allow the wavemaker to operate more efficiently. The downwind beach was built and used by Wilson (1972). It appeared to be very effective over the range of wave conditions encountered in this investigation. Wave probe records showing the absorption of groups of different frequency waves are shown in fig. (3). A transitional flat plate, extending from the outlet of the wind tunnel over the upwind beach and wave generator, provided a smoother entry flow for the wind. Surface layer contaminates were removed efficiently using a surface skimmer installed at the downwind beach. Prior to any experimental run, the wind was turned on, blowing the surface film downwind. The skimmer was turned on and fresh water was added to compensate for that removed by the skimmer.

Reproduced with permission of the copyright owner. Further reproduction prohibited without permission.

§5 AIRFLOW MEASUREMENTS

Intrumentation and Procedure

In the introduction it was pointed out that the postulated 'maser' mechanism of Longuet-Higgins (1969b) is, at least to a first approximation, insensitive to the structure of the airflow above the water waves. The primary role of the wind is to continuously regenerate small scale waves over the entire long gravity wave surface. The mechanism by which this occurs is a separate problem as was pointed out in the introduction. Hence for this investigation only a very limited survey of the airflow was undertaken, mainly for the purpose of establishing reference wind conditions. Only two airflow characteristics were measured. These were:

(a) the vertical profile of the mean windspeed above the water surface and its variation as a function of the steepness of the mechanically-generated gravity waves.

(b) the mean streamwise pressure gradient and its variation as a function of the steepness of the mechanically-generated gravity waves.

The above measurements were made using a micromanometer (Flow Corp. Model MMZ) in conjunction with a pitot-static tube (3 mm diameter) for (a) and with static pressure taps in the tunnel roof spanning the working fetch of the tank for (b).

For fully developed ideal two-dimensional channel flow, Laufer (1951) showed that the shear velocity is given by

$$u_* = \left\{ \frac{d}{\rho_a} \frac{dp}{dx} \right\}^{1/2}$$

where d is the air channel half-height. This predicts equal top and

Reproduced with permission of the copyright owner. Further reproduction prohibited without permission.

bottom shear stress for a channel with rigid upper and lower boundaries. Wilson (1972) showed that this formula provided close (5%) agreement with u_* values obtained from X-meter hot-wire anemometer measurements of Reynolds stress for the centerline mean windspeeds of 1.12 m/sec and 1.84 m/sec and small amplitude waves ($a \sim .03$) generated in his experiments. For the purposes of the present investigation this method sufficed to provide a very approximate estimate of u_*. However the mean velocity and pressure drop measurements did serve to indicate the gross modifications to the wind field induced by changing the wave height.

Results

The mean velocity profiles were measured at a station 7.77 m downwind from the wavemaker. The wind tunnel fan speed was kept constant within $\pm$ 1.5%. The wavemaker frequency was maintained at 1.70 Hz $\pm$ .5%. The effect of wave amplitude on the mean velocity profile can be seen in fig. (4). It was observed that the mean velocity field was affected significantly by the introduction of mechanically-generated waves. The presence of the smallest amplitude mechanical wave caused the mean velocity to increase slightly from the water surface to the center of the wind channel. The larger amplitude mechanically-generated waves caused an overall reduction in the mean velocity field. This effect was most severe for the breaking waves.

The streamwise pressure drop first decreased and then increased markedly with the amplitude of the mechanical waves. This is shown

Reproduced with permission of the copyright owner. Further reproduction prohibited without permission.

in the inset in fig. (4). The wave drag changed significantly as the wave height was varied. Even though the wind tunnel fan was maintained at the same speed ($\pm$ 1.5%) for all the runs, each wave amplitude induced a different pressure drop causing the fan to adjust its mass and momentum flow rate. These produced the observed modifications to the mean wind field. Where the pressure drop rose above the value for purely wind-driven waves, the mean velocity profile decreased and vice versa. The measured values of the pressure drop and the associated shear velocity estimates are given in the table below.

CHARACTERISTIC * AMPLITUDE OF MECHANICALLY-GENERATED WAVES (cm)	$\frac{\Delta p}{\Delta x}$ dynes/cm^3 ($\pm$ 0.5%)	u_* cm/sec
0	0.1200	31.7
0.35	0.1065	30.4
0.53	0.1105	29.8
1.50	0.1280	31.9
2.65	0.2070	41.6

* this is based on the phase averaged mean wave profile computed from the wave records (see the section on "Wave Measurements" for details) and is given by the height of the crest above the mean water level.

Reproduced with permission of the copyright owner. Further reproduction prohibited without permission.

§ 6 WAVE MEASUREMENTS

Intrumentation and Procedure

Measurements of water wave amplitude were made with a set of three impedance-type immersed cylinder wave probes. The probes were arrayed along the centerline of the tank at fetches of 4.27 m, 7.32 m and 10.36 m from the wavemaker. The wave probes used in this investigation were a slightly modified version of those used and described by Wilson (1972). The only revision was a larger-scale sensing element (0.81 mm diameter hypodermic needle) suitable for the higher waves of the present study. This necessitated changing the value of a resistor in the sensing circuitry to reduce the vastly increased signal levels to suitably low levels. Full details of the probe circuitry are given by Flower (1973a).

Prior to their use in the wave measurements, the probes were calibrated statically. The probe outputs were fed into differential amplifiers where the probe d.c. offset was nulled out. The signals were then amplified further and filtered by 100 Hz, 36 db/octave Butterworth filters to remove high frequency noise amplified from the probe circuitry. The output voltage was then recorded for known increments in the depth of immersion over a range of 5 cm, the gain having been set approximately at about 1 volt/cm. A typical calibration curve is shown in fig. (5). The slight nonlinearity apparent in the response was a loading effect on the probe sensing circuitry due to the revised sensor. For the data processing it was decided to approximate the nonlinearity with three linear

Reproduced with permission of the copyright owner. Further reproduction prohibited without permission.

segments which can be seen [fig. (5)] to provide a very close approximation to the actual calibration data.

Consideration was also given to the dynamic response of the probes, especially to the possible modifications to the dynamic response that might occur for the higher frequency waves on account of the presence of a large scale, lower frequency wave. To check for the presence of such spurious effects, a Scotch yoke mechanism which converts rotary motion into true linear sinusoidal motion was used to oscillate one of the probes over a range of approximately 1.25 cm at a frequency of 3.25 Hz (which was the upper frequency attainable with this Scotch yoke mechanism). For each of the following tests, the probe output was fed into a band-pass filter (Dytronics Model 720) set on 3.25 Hz with high selectivity (bandwidth is $\pm$ 2.3% to the 3 db points and then 33 db rejection of the second harmonic and 38 db rejection of the third harmonic) and the output was recorded on a strip-chart recorder:

(a) the probe was oscillated in the manner specified above in still water.

(b) the probe was stationary and detected a train of steep 1.64 Hz gravity waves (2 cm amplitude).

(c) the probe was oscillated as in (a) in the presence of the lower frequency gravity wave described in (b).

Apart from a slight amplitude modulation, traceable to the residual output at 3.25 Hz from (b), the signals in (a) and in (c) showed similar amplitudes indicating that no detectable dynamic

Reproduced with permission of the copyright owner. Further reproduction prohibited without permission.

amplitude attenuation was occurring up to 3.25 Hz. The procedure was repeated for another gravity wave frequency (1.75 Hz) with the same conclusion. In the absence of a convenient method of oscillating the probe at higher frequencies, it was assumed that the amplitudes would be sensed without serious attenuation up to at least 5 Hz.

The actual wave amplitude measurements were motivated in several ways. Visual observations of the wind-driven water surface for a steady windspeed of about 6 m/sec showed definite changes in the wind-wave structure as a function of the steepness of a mechanically-generated, low frequency ($\sim$1.7 Hz) gravity wave train disturbance. As a consequence of the limited streamwise extent of the experimental situation, there was also a strong qualitative variation of the above phenomenon with distance from the wavemaker. Amongst the major effects observed was an apparent attenuation of those wave frequencies corresponding to wind-driven waves as the slope of the mechanical waves was increased. For the case of mechanical waves with slopes of about 0.27, the wind-wave scales appeared to be entirely absent. Furthermore, the character of the ripple structure also changed noticeably from a situation where the dominant role of the ripples was in the leading-edge dissipation mechanism to a role where the long waves were sweeping through the ripple field, interacting strongly at the crests and weakly in the troughs of the gravity waves. Other observations were made about the onset of breaking of the

Reproduced with permission of the copyright owner. Further reproduction prohibited without permission.

long gravity waves as their steepness reached the limiting value. It appeared as though a stagnation point occurred on the forward face just below the crest of a wave immediately prior to and during the initial moments of the breaking process. To effectively document such observations as the above, a system relating surface photographs to the long wave phase was developed. This will be described presently.

The wave probe outputs from the nulling, amplifying and filtering stages were recorded on a Honeywell 5600 FM tape recorder operated at 60 ips. The data collected consisted of six 10 minute records comprising wind-waves, wind-waves in the presence of four different slopes of mechanically-generated 1.7 Hz waves, and a noise record. The fanspeed was maintained at a constant reference value (within $\pm$ 1.5%) for all runs. The mechanical wavemaker was set at 1.7 Hz and was kept with $\pm$ 0.2% during the data collection runs. Prior to collecting each record, calibration data consisting of references voltages of + 1.00, 0.0, -1.0 volts generated by the tape recorder were recorded on each channel. This provided a very accurate means of calibrating the record-playback system gain. The accuracy obtained using this procedure was better than one percent.

Data Reduction

After the data collection, the analog tapes were replayed and visually monitored by storage oscilloscope and/or strip chart recorder both in real time and with a time compression of 64 (replay

Reproduced with permission of the copyright owner. Further reproduction prohibited without permission.

speed of 15/15 ips). Segments of records were then selected for processing.

After this preliminary editing process, data reduction was done digitally. The data was played into the analog-to-digital converter in real time. A-D conversion was performed with a modular A-D converter (Raytheon MADC 10-04-08 Miniverter) which was controlled by a home-built driver, providing a choice of sampling frequencies, record lengths and number of inputs. In these experiments, the length of each data series was 12,000 words and the sampling frequency was 48.00 samples per second per probe. Each sampled data point was converted into a 9-binary-bit number, providing a range-to-resolution ratio 512:1. The least count (approx. 20 mv/count) provided resolutions of better than 0.2 mm for the amplitude displacements based on the static calibrations. The home-built driver then fed the digitized wave signals to an incremental magnetic tape recorder (Kennedy 1400) using a computer-compatible 7-track format, one track being parity. Pairs of 9-bit numbers were recorded on tape as a sequence of three 6-bit characters. A computer program (WT-A) was then used to unpack the data tapes and convert each 9-bit number into standard 36-bit format. In the same program, frequency distribution tables were computed for the voltage values and first-differences of voltage values for each time series selected for processing from each record. This program also created an output tape containing the unpacked wave amplitude time series. This, together with limits for the values of voltages

Reproduced with permission of the copyright owner. Further reproduction prohibited without permission.

and first-differences of voltages inferred from the printed output of the previous program and the voltage-to-displacement calibrations for each data series, was sent through the second preliminary computer program (WT-B). In this program the voltage counts were converted to displacement counts using the piecewise linear calibration curve data to correct the nonlinearity of the probes. Extreme values of either data values or first differences of data values according to the preset limits were detected; if the number of consecutive gliches was two or less, then these values were replaced by linearity interpolating between the preceding and ensuing "good" values. This was sufficient to handle 100 percent of the gliches detected. If more than two consecutive gliches had occurred, a message would have been printed out and processing discontinued for that record. An output tape was created for all records (other than those with discontinued processing) and was used as input to the third program (WT-CC).

In WT-CC, the data series for each probe had its mean and linear trend removed. An output tape with this data was created for use as input to the spectral analysis program WT-FFT. WT-CC then made an analysis of the zero-crossings of each data series. The zero-crossings were detected according to whether a given data point A(K) was within a preset amplitude range about zero. A given zero consisted of searching for a set of such points so that the difference in the indices between the last member of the set and the first member of the next set of zero-crossings exceeded a

Reproduced with permission of the copyright owner. Further reproduction prohibited without permission.

preset value. Any given set of indices satisfying the above criteria formed a composite zero. Their indices were averaged arithmetically to obtain a characteristic zero-crossing index. These were then analyzed as belonging to positive-going, negative-going or indefinite categories by checking the amplitude of the data one point preceding and one point following a given set of data points comprising a composite zero-crossing. The set of positive-going zero-crossings was used to compute the number of complete long wave cycles, the average interval between the positive zeroes, the percent deviations of the individual intervals between positive zeroes from the average interval. A phase-averaging scheme using the positive-going zero-crossings as origin and the average interval as the range was then used to compute:

(a) the mean (phase-averaged) long wave profile.

(b) the mean (phase-averaged) variance of the wave record from this mean long wave as a function of the long wave phase.

In the actual data reduction, the sample rate (48.00 samples per second per probe) and record length (12,000 words per probe) provided 250 seconds of real-time data capability for each probe. For the 1.7 Hz mechanically-generated gravity waves, this provided an ensemble of 425 waves and a cycling interval of 28 points per wave. From on-line computer plots of the first and last 100 points of each data series for each probe, appropriate choices were made for the amplitude and indicial limits for the zero-crossing determination. These plots also served to confirm the validity of the zero-crossing

Reproduced with permission of the copyright owner. Further reproduction prohibited without permission.

detection program. The phase-averaged, mean long wave profile and the distribution of the phase-averaged variance of the deviations of the individual waves from the mean long wave were plotted by a Calcomp plotter using the Johns Hopkins University Computing Center library subroutine QDPLOT.

After these plots were obtained, it was observed that the distributions of phase-averaged squared deviations of the individual waves from the computed mean long wave showed consistently low values at zero phase (defined by the first positive-going zero-crossing of the mean long wave) relative to the last phase point. Under ideal circumstances, it does not seem reasonable to expect a discontinuity in the phase-averaged squared deviation function at the ends of the phase interval. It was suspected that the method of phase-averaging used might have introduced a bias at the ends of the phase interval. An analysis of the potential errors involved in the phase-averaging procedure is given in Appendix III. The corrections indicated by this analysis are discussed in the next section where the results of the wave measurements are presented.

The output tape created prior to the zero-crossing and phase-averaging analysis formed the input data to the Fast Fourier transform program WT-FFT which computed spectra for the various data series. The data selected for processing was assumed to have negligible energy content (apart from electronics noise) beyond 20 Hz on account of the natural attentuation of the phenemenon and of the probe response (due to dynamic meniscus effects). It

Reproduced with permission of the copyright owner. Further reproduction prohibited without permission.

was felt therefore that the salient features of the high energy, low frequency (<5 Hz) region of the spectrum would be negligibly distorted by folding back of energy beyond 24 Hz due to aliasing caused by undersampling. Earlier trial runs using 36 db/octave 8 Hz filters prior to digitizing at 32 Hz confirmed the validity of the above procedure in defining the spectral characteristics below 5 Hz. Thus for the spectra reported in this investigation, a sampling frequency of 48 Hz was used for each data series.

In WT-FFT, the FFT2 library subroutine was used to perform the Fourier transforms. Being especially fast on transforming 2^N data points (for positive integers N), each data series was divided into eleven subrecords of 1024 data words, thereby utilizing 11,264 of the available 12,000 words of data. Each 1024 word subrecord yeilded 513 (complex) Fourier amplitudes for the frequency range 0.00 - 24.00 Hz. The eleven sets of spectral estimates were averaged, yielding a smoothed spectrum. According to Jenkins and Watts (1968, Ch.6.3) this technique of spectral smoothing is equivalent to convolving the sampled spectrum estimator with the spectral window

$$W(\S) = M \left\{ \frac{\sin(\pi \S M)}{\pi \S M} \right\}^2$$

where the record of total length T has been subdivided into r equal subrecords of length M. For the present analysis, T = 234.7 secs, r = 11 and so M = 21.33 seconds. Also f is the frequency in Hz. This spectral window has a bandwidth (defined as the separation between the first zeroes on either side of the main lobe of the

Reproduced with permission of the copyright owner. Further reproduction prohibited without permission.

window) given by

$$B_{\omega} = 2/M = 0.0938 \text{ Hz}$$

and yields a variance associated with the spectral estimates equal to $0.667\frac{M}{T} = 0.0606$ of the variance of the sampled spectrum. The number of degrees of freedom is 33. The bias associated with this window depends on the nature of the shape of the spectrum and the sample size; it was not estimated explicitly. However, since further smoothing of the spectrum by averaging over triads of adjacent estimates yielded spectra with the same qualitative features, it appeared that the bias was not important. Averaging over triads of adjacent estimates served to reduce the variance by a further factor of 3 and increase the degrees of freedom correspondingly at the expense of a decreased bandwidth of 0.28 Hz. This computation was performed for the four mechanical wave records, the wind-wave record and the noise record. In addition, the effect of the spectral window in shaping the measured spectra was determined computationally by running the spectral analysis on a pure sinusoid of unity mean squared amplitude and with a frequency set mid-way between the resolution points of the frequency axis. The function used was

$$A(I) = \sqrt{2}\sin\left[2\pi \times \frac{1.71}{48.0} \times (I-1)\right], \quad I = 1,11264$$

All spectra were plotted using a logarithmic scale over 8 decades in the mean squared amplitude and over a linear frequency scale using the off-line Calcomp plotter programed by QDPLOT.

To complement the numerical data, a comprehensive photographic

Reproduced with permission of the copyright owner. Further reproduction prohibited without permission.

documentation of the various wave surface conditions was undertaken. A centimeter scale was aligned in the streamwise direction at a height of 4.5 cm above the mean water level in the absence of waves. A 35 mm S.L.R. camera with a 50 mm lens was mounted at a height of 95 cm above the mean water level. A wave probe was installed at the same fetch (within $\sim$ 1 mm) as the center of the viewing screen of the camera. An electronic strobe unit was positioned both upstream and downstream of the camera. It was used to momentarily illuminate the water surface by bouncing the light off the matte white ceiling of the laboratory. A photo-transistor circuit was used to register the firing of the strobe as a 2 volt pulse. The pulse and wave probe data were recorded on the tape recorder at 60 ips and played back at 15/16 ips, providing a clear indication of the large scale gravity wave phase at which the camera stopped the motion. Although useful primarily for the larger amplitude mechanical wave situations, this data was recorded and is shown for all the published photographs. About 10 frames were shot at each station of the five wave conditions studied in this investigation. The orientation of the strobe was varied slightly during each sequence of frames and its position was changed from upstream to downstream for half the number of pictures shot of any wave situation at each fetch. Combined documentation showing the surface photograph and the epoch-marked wave probe trace is presented for each wave condition.

Reproduced with permission of the copyright owner. Further reproduction prohibited without permission.

Results

The visual observations as recorded by the system of surface photography complemented the wave spectra and the distributions of phase-averaged mean long wave and mean-squared deviations from the mean long wave. It was anticipated that each of these descriptions could be combined to permit a clearer perception of the dynamical processes involved in this wind-wave interaction study. Before discussing the results specific to each wind-wave situation studied, a few preliminary remarks about the data will be given.

The noise spectra given in fig. (6) show the combined electronics noise and computational noise for each channel. However, wave probe calibration errors are not represented in these curves. It is estimated that for any point on the calibration curve, the amplitude error amounted to less that $\pm$ 1 percent of the total amplitude range over which the probe was calibrated, i.e. amplitude could be resolved to $\pm$ 0.5 mm. The noise introduced by dynamic maniscus effects on the probe could not be estimated over the full frequency range of the probe but was shown to be negligible at 3.25 Hz (see previous section in this chapter for details).

The spectral window shape, shown in fig. (7), was computed for a sine wave with unity variance whose frequency was set to fall half-way between two frequency abscissae selected by the spectral analysis routine. In particular, the high frequency end

Reproduced with permission of the copyright owner. Further reproduction prohibited without permission.

of all the wave spectra clearly show the influence of the window.

The significant data, lying in the range 1 - 8 Hz, was negligibly affected by the noise, being 4 decades down from the spectral peak and 2 decades down at 8 Hz for the worst case (record 9, probe 1). The high frequency spikes appearing in the noise data correlate with those in the lower amplitude wave spectra and are therefore to be disregarded. Many of the similarities and differences between the various flow situations are well represented in the spectra and will be discussed presently.

The phase-averaged computations were fairly successful in determining the phase-averaged mean wave profile. The calculations of phase-averaged mean squared devations from the mean profile were somewhat less reliable due to an apparent bias introduced by the phase-averaging procedure used. This matter is taken up in detail in Appendix III.However, these phase-averaged characteristics did show clear and fetch-consistent trends which differed substantially among the various situations investigated. It was also reassuring that the computed mean wave profiles were consistent with individual waves from their ensemble both in amplitude and shape and also that the variance obtained by integrating under the spectra.

(a) Purely wind-generated waves - no mechanical waves.

The steady state wave surface consisted of a fetch-dependent short gravity carrier wave with strong leading-edge rippling which

Reproduced with permission of the copyright owner. Further reproduction prohibited without permission.

moved with the carrier waves. The appearance and relative local amplitude structure of the water surface are shown in plates 1, 2 and 3. (For this and all subsequent references to the plates, triads of plate numbers are arranged in order of increasing fetch). It can be seen from the spectra in figs. (8), (9) and (10) that the spectral peak for the gravity wave components of the wind-generated wave field is fairly broad-band. Also the spectral peak shows a definite shift to lower frequencies with increasing fetch. This is discernable in plates 1, 2 and 3. This is characteristic of an active wind-generated wave field where wave components with frequencies less than those at the spectral peak are unsaturated and are still growing. Given an unlimited fetch, this will continue to progress to lower frequencies and longer wavelengths. In the wave tank, the finite fetch was the limiting factor.

(b) Mechanically-generated waves with 0.30 cm amplitude.

The addition of mechanically-generated waves with a slope (α) of 0.03 and frequency 1.7 Hz appeared to result in a linear superposition of the wind-wave field and the mechanical wave field at all fetches. This can be seen in plates 4, 5 and 6. This quantitative observation was confirmed by comparing the spectra for this situation figs. (11), (12) and (13) with those of the purely wind-driven situation. The spectral peaks of the wind-generated components were marginally reduced from those determined

Reproduced with permission of the copyright owner. Further reproduction prohibited without permission.

in the absence of the carrier wave. The phase-averaged mean wave profile showed serious departures from the sinusoidal shape of the carrier wave. However, the distribution of zero-crossings was highly erratic and spread over many intervals. It could not be expected, then, that the method of phase-averaging used in this study could yield reliable results for this case, so no further discussion of the phase-averaged distributions will be undertaken for this condition.

(c) Mechanically-generated waves with 0.5 cm amplitude.

Increasing the amplitude of the mechanical waves to 0.53 cm produced a wave slope of about 0.06 for the carrier wave. The appearance of the surface resembled that of the smaller slope situation with respect to the continued presence of the wind driven gravity wavelets (see plates 7, 8 and 9). The spectra for this situation, figs. (14), (15) and (16), confirmed this fact, also indicating the presence of a small second harmonic of the carrier wave. It is also apparent, especially from the spectrum for the first probe [fig.(14)] that the wind-generated components have been attenuated and smeared over a wider frequency band. This indicates slightly nonlinear interaction and is probably due to the deformation of the gravity wavelets by the orbital velocity field of the carrier waves. With increasing fetch, the wind-wave spectral peak shifts to lower frequencies around the second harmonic of the carrier and the effect is masked.

Reproduced with permission of the copyright owner. Further reproduction prohibited without permission.

The phase-averaged mean wave profiles were almost sinusoidal. The mean deviation distributions had large offsets at the end of the phase interval, indicating a significant bias. However, if the type of correction derived in Appendix III is applied qualitatively, it may be seen that there is a consistent peaking in each distribution at the crest and a nodal region towards the trough. This is consistent with the results of Longuet-Higgins and Stewart (1960) who showed that short gravity waves, when superposed on much longer gravity waves tend to become both shorter and steeper at the crests of the carrier waves, and corresponding lower and longer in the troughs. It was also observed that the level of the mean squared deviation distribution increased systematically with fetch and that the pressure drop in the airflow assumed its lowest value in this situation.

(d) Mechanically-generated waves with 1.5 cm amplitude.

Here the slope of the carrier wave jumped to around 0.175, indicating a fairly steep finite amplitude mean wave profile. There was a definite growth of the carrier wave with fetch; the slopes ranged from 0.16 to 0.20 over the working fetch. The airflow pressure drop was comparable with that for the purely wind-driven case. The wave field in this situation contrasted in a number of ways from the previous cases. The most impressive difference was the apparent absence of the gravity wind-wave scales. As a result, the short wave structure possessed an entirely different character,

Reproduced with permission of the copyright owner. Further reproduction prohibited without permission.

shown vividly by comparing plates 10, 11 and 12 with any of the previous plates. The short wave structure changed from strong leading-edge rippling travelling with the gravity wavelets (as seen in the previous smaller slope situations) to a structure in which the long waves were seen to sweep through the short wave field. This resulted in a strong compression of the short waves on the forward face of the carrier. The rear face was only sparsely covered with short waves. The spectra confirmed the absence of the wind-generated gravity wavelet scales [figs. (17), (18) and (19)] and indicate merely the presence of several of the harmonics of the basic carrier wave. There is no evidence of a fetch-dependent broadening of the frequency band associated with this carrier wave.

We now turn to the phase-averaged data also shown in figs. (17), (18), and (19). These distributions were judged to be relatively free of bias for this realization, as indicated by the approximately equal values of the mean squared deviation distribution at the ends of the phase interval. The mean wave distribution showed the characteristic asymmetric profile associated with finite amplitude gravity waves. The distributions of mean squared deviations indicated a shift of the peak at the wave crest at the first fetch to a bimodal peaking on the forward and rear faces at the downstream fetches. The structure of the water surface shown in plates 10, 11 and 12 reveals an interesting concentration point near the crest where a local discontinuity is forming. This probably arises from

Reproduced with permission of the copyright owner. Further reproduction prohibited without permission.

the strong ripple-carrier interaction which occurs in the vicinity of the crest. A very significant feature of the long wave structure is the lack of sharpness at the individual crests (evident in the traces below the photographs in plates 10, 11 and 12). Hence this is not simply a case of limiting through leading-edge ripple generation. At this point it is expedient to postpone further discussion of these phenomena until the last situation has been reported.

(e) Mechanically-generated waves with 2.5 cm amplitude.

The carrier wave amplitude, increased further, produced a wave train whose mean slope ranged from 0.28 at the first fetch, up to 0.303 and down to 0.285 at the third fetch. The character of the flow differed markedly between the first and last fetches, however. The structure at the upstream fetch (see plate 13) was qualitatively similar to that of the previous (a = .175) situation; however the leading edge compression of short waves seems to have been more severe. The wave crests remained rounded and the long waves were observed to be sweeping through the short wave field, with groups of ripples moving along with the crest momentarily and then falling behind.

With increasing fetch, an intermittent amplitude limiting mechanism began to occur. By the third fetch, this process was going on continuously. This type of limiting mechanism might

Reproduced with permission of the copyright owner. Further reproduction prohibited without permission.

best be characterized as a rolling of the crests towards a point of relative stagnation which was observed just ahead of the carrier wave crest. At this stagnation point, the carrier phase speed is matched by the velocity of the surface flow arising from the orbital motion and the wind drift. Associated with this type of structure must be a detached streamline which extends from the stagnation point into the interior of the wave. It separates the fluid involved in the rolling motion from the ambient wave motion, as is shown in fig. (23) which indicates the proposed rolling layer structure. The flow above the detached streamline is highly turbulent and entrains air as it develops, often causing sporadic bubbling. This is observed in plate 15. However, bubbling is not an essential part of the mechanism.

Turning to the measurements shown in figs. (20), (21) and (22), we again observe the total absence of wind-wave gravity wavelet scales, the presence of even higher harmonics of the carrier and also a broadening with fetch of the frequency band about the fundamental peak of the carrier. The phase-averaged mean wave profiles appear to have been reliably extracted and indicate an even greater profile asymmetry than the previous situation. The mean wave grew with fetch initially, then was attenuated, clearly a result of the breaking process. The distributions of mean squared deviations indicated a slightly higher bias than the previous case. Nevertheless, a large peaking of this distribution occurred on the rear face of the carrier and this trend persisted with fetch.

Reproduced with permission of the copyright owner. Further reproduction prohibited without permission.

A second, somewhat smaller peak on the forward face grew with fetch to exceed the rear face peak at the third fetch. The overall energy represented by the mean squared deviations also appeared to grow considerably with fetch.

The next chapter presents a development of a model aimed at explaining the onset of the rolling-breaking phenomenon. Several of the other observations made in situations prior to the wave-breaking can also be accounted for by the predictions of the model.

Reproduced with permission of the copyright owner. Further reproduction prohibited without permission.

§ 7 ANALYSIS OF THE OBSERVED BREAKING PHENOMENON

Consider a slowly varying wavetrain

$$\zeta = Re\left\{\hat{a}(x,t)\, e^{i\epsilon^{-1}\hat{\theta}(x,t)}\right\} \qquad (Re = \text{real part})$$

in which $\hat{a}(x,t)$ is the local amplitude and $\hat{\theta}(x,t)$ the phase function. The local wave number and frequency are defined as

$$\underset{\sim}{k} = \nabla\hat{\theta} \qquad \text{and} \qquad \nu = -\frac{\partial\hat{\theta}}{\partial t} \qquad \text{so that}$$

$$\frac{\partial \underset{\sim}{k}}{\partial t} + \nabla\nu = 0$$

We now transform this equation into our moving frame, translating the frame of reference to the right with the long wave phase speed C. In terms of the curvilinear coordinate system where the mean wave is given by $\eta = 0$, the above conservation law preserves its form provided the dependent variables are interpreted as relative to the moving frame of reference. The transformation follows analogously to that given earlier for the equations of motion and will not be reiterated here. The result obtained for the wavenumber component k in the "lateral" (ξ) direction is

$$\frac{\partial k}{\partial t} + \frac{1}{k}\frac{\partial \hat{\nu}}{\partial \xi} = 0 \qquad \ldots\ (7.1)$$

where $\hat{\nu}$ is the number of wave crests passing a given point fixed in the moving frame of reference. We also have

$$\hat{\nu} = \nu + k\,u(\xi) \qquad \ldots\ (7.2)$$

Reproduced with permission of the copyright owner. Further reproduction prohibited without permission.

where ν is the intrinsic frequency and $k u(\xi)$ is the apparent frequency if the wavetrain is being convected past the fixed point (in the moving frame) with the mean velocity $u(\xi)$. Here $u(\xi)$ is the total tangential velocity in the moving frame and is the resultant of the wind drift velocity, the tangential component of the orbital velocity and the velocity component locally parallel to the surface $\eta = 0$ induced by the translation of the frame of reference. Thus we have

$$u(\xi) = u_d^* + u_o^* - C\cos\Theta \qquad \ldots. (7.3)$$

where u_d^* is the drift velocity (assumed constant) in the rest frame and u_o^* is the tangential component of the orbital velocity also measured in the rest frame. C is the translational velocity of the frame and has a component $C\cos\Theta$ along the surface, where Θ is the relative inclination of the surface $\eta = 0$ to the surface $z = 0$. We note further that for this problem, u is always negative except at any stagnation points. Hence we let

$$U(\xi) = -u(\xi) > 0 \qquad \ldots. (7.4)$$

= speed to the left in the moving frame.

At a fixed phase point in the reference frame, the wave number is assumed to be quasi-stationary in <u>time</u> varying only over timescales which are large compared with the long wave period. Hence the conservation law (7.1) reduces to

$$\frac{\partial \hat{n}}{\partial \xi} = 0$$

$$\text{or } \hat{n} = \text{constant} \qquad \ldots. (7.5)$$

Reproduced with permission of the copyright owner. Further reproduction prohibited without permission.

The intrinsic frequency in the moving frame is given by

$$n = kc \qquad \ldots\ldots (7.6)$$

where k, c are the wave number and phase speed measured in the moving frame. k is taken positive in the positive x direction. Combining (7.2), (7.5) and (7.6) yields:

$$\begin{aligned} \hat{n} &= kU - n \\ &= kU - kc \\ &= \text{constant} \end{aligned} \qquad \ldots\ldots (7.7)$$

This expresses the fact that the apparent frequency is always positive in the moving frame i.e. the waves appear to be swept to the left in the moving frame.

We now evaluate this constant at a convenient phase point on the long wave - that point where the tangential component of the orbital velocity in the rest frame vanishes and which is a point of convergence of the streamlines. This locates the reference point x_r on the forward face of the long wave crest. Thus from (7.3) and (7.4) :

$$U_r \equiv -u(x_r) = -(u_d - C\cos\theta_r) \qquad \ldots\ldots (7.8)$$

Thus U_r = constant, > 0 for cases of physical interest in this study.

From (7.7) we have

$$k(U-c) = k_r(U_r - c_r) \quad , \qquad \ldots\ldots (7.9)$$

where k_r, c_r are the wave number and phase velocity of the short

Reproduced with permission of the copyright owner. Further reproduction prohibited without permission.

waves in the moving frame. Assuming that gravity is the predominant short wave restoring force, k, k_r, c, c_r are related through the dispersion relation for gravity waves

$$\frac{k_r}{k} = \frac{c^2}{c_r^2}$$

Using this result in (7.9) gives

$$\begin{aligned} u - c &= \left(\frac{c}{c_r}\right)^2 (u_r - c_r) \\ &= c_r \left(\frac{c}{c_r}\right)^2 \left(\frac{u_r}{c_r} - 1\right) \end{aligned}$$

Rearranging, we obtain

$$\left(\frac{u_r}{c_r} - 1\right)\left(\frac{c}{c_r}\right)^2 + \frac{c}{c_r} - \frac{u_r}{c_r} = 0 \qquad \ldots\ (7.10)$$

which has the solutions

$$\frac{c}{c_r} = \frac{-1 \pm \sqrt{1 + 4\frac{u(s)}{c_r}\left(\frac{u_r}{c_r} - 1\right)}}{2\left(\frac{u_r}{c_r} - 1\right)} \qquad \ldots\ (7.11)$$

where all coefficients are positive.

To decide which root is physically meaningful, we note that when $u = u_r$, $c = c_r$ from (7.9). Thus in (7.11) we see that

$$\begin{aligned} \sqrt{1 + 4\frac{u}{c_r}\left(\frac{u_r}{c_r} - 1\right)} &= \sqrt{1 + 4\frac{u_r}{c_r}\left(\frac{u_r}{c_r} - 1\right)} \\ &= \sqrt{1 - 4\frac{u_r}{c_r} + 4\left(\frac{u_r}{c_r}\right)^2} \\ &= 2\frac{u_r}{c_r} - 1 \end{aligned}$$

Reproduced with permission of the copyright owner. Further reproduction prohibited without permission.

Hence we adopt the positive root

$$\frac{c}{c_r} = \frac{-1 + \sqrt{1 + 4\frac{u(\xi)}{c_r}\left(\frac{u_r}{c_r} - 1\right)}}{2\left(\frac{u_r}{c_r} - 1\right)} \quad \ldots\ldots (7.12)$$

Also, we note that as $u(\xi) \to 0$, $\frac{c}{c_r} \to 0$ so that $k/k_r \to 0$ which is not realistic for gravity waves. Therefore such a stagnation point is singular in this respect and what follows holds strictly only in the vicinity of such a stagnation point.

The energy flux velocity for the short waves in the moving frame is given by

$$c_e(\xi) = c_g - u(\xi) \qquad \text{to the right}$$

$$= \tfrac{1}{2}c - u(\xi)$$

$$= \frac{-c_r + c_r\sqrt{1 + 4\frac{u(\xi)}{c_r}\left(\frac{u_r}{c_r} - 1\right)} - 4u(\xi)\left(\frac{u_r}{c_r} - 1\right)}{4\left(\frac{u_r}{c_r} - 1\right)}$$

$$= \frac{c_r}{4\left(\frac{u_r}{c_r} - 1\right)}\left\{-1 + \sqrt{1 + \chi} - \chi\right\} \quad \ldots\ldots (7.13)$$

where $\chi = 4\frac{u(\xi)}{c_r}\left(\frac{u_r}{c_r} - 1\right)$

Thus the distribution of $c_e(\xi)$ is determined by the function

$$\sqrt{1+\chi} - \chi - 1 \qquad \text{where } \chi = 4\frac{u(\xi)}{c_r}\left(\frac{u_r}{c_r} - 1\right)$$

which is shown in the diagram below. Note that the sign of is determined by the sign of $u(\xi)$.

Reproduced with permission of the copyright owner. Further reproduction prohibited without permission.

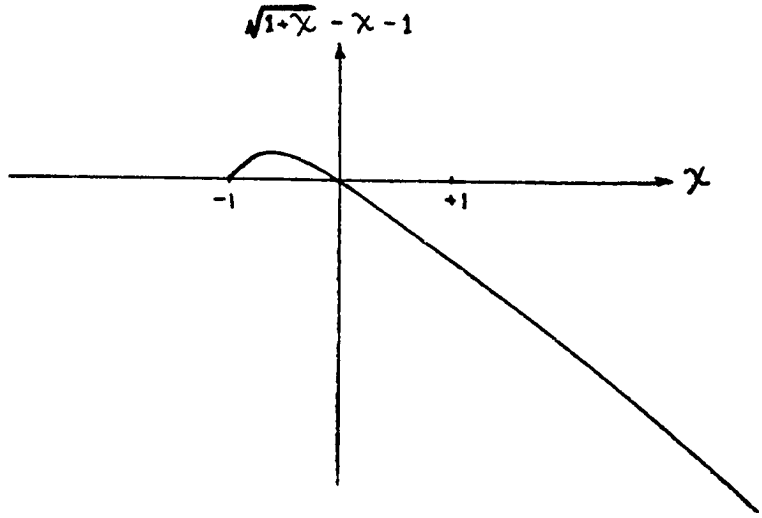

Thus

(a) if $\chi > 0$ everywhere, the short wave energy flux is always in the negative ξ direction.

(b) if χ changes sign and has a negative region ($0 > \chi > -1$), then the short wave energy flux reverses relative to the long wave profile and is in the positive ξ direction.

(c) $\chi < 0$ implies the existence of a stagnation point, which is an energy sink by (a) and (b).

We now examine the dynamics at the long wave surface to see under what conditions such stagnation points will occur.

The action of the wind stress on the water surface produces, besides the short waves, a wind drift confined to a thin surface region [see, for example, Wu (1968)]. Associated with the wind drift is a vorticity distribution $\omega(\eta)$ in the cross-wind direction normal to the wind stress. If the distribution of wind drift is

Reproduced with permission of the copyright owner. Further reproduction prohibited without permission.

denoted by $u_d(\eta)$ in the moving frame then the vorticity $\omega(\eta)$ is given by

$$\omega(\eta) = \frac{1}{h} \frac{\partial}{\partial \eta} (h u_d)$$

Ignoring viscous effects, the vorticity in the surface layer is conserved. Neglecting the variations in the depth of the wind drift layer, we have

$$u_d(0) = \int_{-\infty}^{0} \frac{1}{h} \frac{\partial}{\partial \eta} (h u_d)\, d\eta \qquad = \text{constant along } \eta = 0$$

For the two dimensional long gravity wave flow which is quasi-steady in the moving frame, the dimensional form of Bernoulli's equation along the surface $\eta = 0$ by

$$\underset{\sim}{\omega} \times \underset{\sim}{u} + \nabla\left(P/\rho + \tfrac{1}{2} u^2(\xi) + g z\right) = 0 \quad , \text{ the } \xi \text{ component}$$

of which is

$$\frac{1}{h} \left\{ \frac{\partial}{\partial \xi} \left[P/\rho + \tfrac{1}{2} u^2 + g \eta_0(\xi) \right] \right\} = 0$$

since $\omega \times u$ is normal to $\eta = 0$. Here $\eta = \eta_0(\xi)$ is the free surface elevation above $z = 0$. We will also neglect the effects of the short waves on the pressure and velocity. (It was established in §3 that in the absence of wind drift, the pressure and velocity modifications were $O(\epsilon)$ where ϵ is the wavelength ratio between the short and long waves, assumed very small here).

Hence we assume P/ρ = constant on $\eta = 0$ and we have

$$\tfrac{1}{2} u^2 + g \eta_0(\xi) = B \text{ , constant.} \qquad \ldots\ (7.14)$$

To evaluate B, we average spatially over a wavelength of the long wave to obtain

Reproduced with permission of the copyright owner. Further reproduction prohibited without permission.

$$B = \tfrac{1}{2}\,\overline{u^2(\xi)} \qquad \ldots\ (7.15)$$

We now calculate $u(\xi)$ in order to evaluate B

$$\overline{u^2} = \overline{\{C\cos\theta - u_d - u_o\}^2} \qquad \text{where } u_o = \text{orbital speed}$$

$$= \overline{\{(C-u_d) - (1-\cos\theta)C - u_o\}^2}$$

$$= (C-u_d)^2 + \overline{(1-\cos\theta)^2}C^2 + \overline{u_o^2} - 2(C-u_d)\overline{(1-\cos\theta)}C$$
$$- 2(C-u_d)\overline{u_o} - 2\overline{u_o(1-\cos\theta)}C$$

In this equation, we note that $|\theta| < \frac{\pi}{6}$ and so $1-\cos\theta \sim \theta^2/2$ is small. Also the mean value of the orbital velocity and the correlation between the orbital velocity and θ^2 are also very small. Hence we have

$$\overline{u^2(\xi)} \simeq (C-u_d)^2 + \overline{u_o^2}$$

Thus in (7.14) we see that a stagnation point occurs when $u = 0$ i.e. when $\eta_o = \eta_o^{SP}$ where

$$\eta_o^{SP} = \frac{(C-u_d)^2 + \overline{u_o^2}}{2g} \qquad \ldots\ (7.16)$$

We note that as the magnitude of the surface current u_d increases, η_o^{SP} decreases. For a fixed wave height, there are two points which can then satisfy (7.16). They are situated on either side of the crest. Before proceeding to relate these results to the observations and measurements reported earlier, it is interesting to make the following comparison: in purely irrotational flow, with no surface wind drift, the expression (7.16) above gives an approximation to the limiting height of water waves with a sharp

Reproduced with permission of the copyright owner. Further reproduction prohibited without permission.

crest subtending 120° at the apex on which is a stagnation point

$$\eta_0^{SP} \simeq \frac{C^2 + \overline{u_0^2}}{2g}$$

The orbital velocity has a sharp maximum of C at the wave crest and a minimum in the troughs; the distribution over the long wave phase is not sinusoidal. An estimate of $\overline{u_0^2}$ based on the results of Michell (1893) is

$$\overline{u_0^2} \simeq 0.22\, C^2 \quad (\pm 10\%)$$

$$\eta_0^{SP} \simeq 0.61\,(1.20)\frac{\lambda}{2\pi} = 1.17\,\lambda \quad (\pm 10\%)$$

as the phase speed for the maximum height wave is given by

$$C^2 \simeq 1.2\, g/k$$

In comparison, the maximum height-mean level distance calculated by Michell (1893) for the Stokes wave of maximum steepness is $\sim 0.123\,\lambda$. This shows that our estimate (7.16) is not unreasonable and predicts breaking before the limiting height for the Stokes wave of maximum steepness is attained.

In the following chapter, these predictions are compared both quantitatively and qualitatively with the observations reported in §6.

Reproduced with permission of the copyright owner. Further reproduction prohibited without permission.

§ 8 COMPARISON OF THEORY AND OBSERVATION

We will begin by examining the predictions of the previous chapter. It was found that the wave amplitude necessary for a stagnation point to occur was given by (7.16) as

$$\eta_o^{SP} = \frac{(C - u_d)^2 + \overline{u_o^2}}{2g}$$

Wu (1968) found that $u_d \sim 0.04\, U_\infty$ where U_∞ is the wind speed at the channel center line. For this investigation, U = 6.5 m/sec and so $u_d \sim 26$ cm/sec. We will take C, $\overline{u_o^2}$ based on the infinitesimal amplitude values to obtain an initial estimate for η_o^{SP} and then reiterate if necessary. The phase speed corresponding to a 1.7 Hz wave is 91.8 cm/sec . We will assume that for small amplitude waves, $\overline{u_o^2}$ is negligibly small, being proportional to the square of the slope.

Hence

$$\eta_o^{SP} \sim \frac{(92 - 26)^2}{2 \times 980} \sim 2.2 \text{ cm}$$

This value has an associated slope given by

$$a = \frac{2\pi}{54} \times 22 = 0.26$$

necessitating a revision of the initial estimate. For $a = 0.26$, $c^2 = 92\,[1 + (0.26)^2] = 92^2(1.068)$ giving $C \sim 95.8$ cm/sec. Also, we will assume $\overline{u_o^2} \sim 0.05\, C^2$. Thus we have

$$\eta_o^{SP} \sim \frac{(96 - 26)^2 + 425}{2 \times 980} \approx 2.7 \text{ cm}$$

Reproduced with permission of the copyright owner. Further reproduction prohibited without permission.

This adjusted value coincides very closely to the amplitude recorded at the second station for the steepest wave in this study (Record 5). At this station, sporadic rolling-breaking was observed; by the third station, this process was occuring continuously. The qualitative differences may be seen in plates 14 and 15. Thus the quantitative agreement between theory and observations is very close. We now examine the distributions of phase-averaged deviations to see if they show trends consistent with the energy-flux notions also derived in the previous chapter.

For records 4 and 5 (slopes ~ 0.175 and ~ 0.28) a strongly bimodal distribution of mean squared deviations about the crest was observed [figs. (17) - (22)]. The leading peak was seen to increase with fetch in each record. It was mentioned in §7 that there exists the possibility of two stagnation points which can satisfy (7.16), one on the forward face and on the rear face of the crest. This appears to be consistent with the observed distributions, as it was also shown that a stagnation point is a local energy sink. This might also account for the disappearance of the natural wind-generated gravity wavelets. With the onset of stagnation points, the energy is effectively trapped at one location (at least) on each long wave length. Thus there is insufficient fetch over which the gravity wavelets may develop.

We now turn to the question of the viability of the 'maser' theory in terms of how the measurements relate to the theory developed in §3.

Reproduced with permission of the copyright owner. Further reproduction prohibited without permission.

It is felt that the experimental situation most closely approaching the model was in record 4. The plates relevant to this situation [plates (10, 11, and 12)] indicate strong ripple compression on the forward face with some ripple breaking at the crest. The rear face shows less compression, fewer ripples and indicates generally less ripple activity.

From the point of view of the dynamical coupling between the ripple layer and the long wave, it was shown in §3 that the gradient of the mean squared deviations should have a significant component in phase with the wave elevation if the ripple layer is to be of dynamical significance. Turning to figs. (17), (18) and (19), it can be seen that the long waves did grow significantly over the fetch spanned by the three probes. By differentiating the distribution of phase-averaged squared deviations, considerable variation is seen in the degree of correlation between the elevation and the gradient of the distribution over the wave fetch. The correlation is low at the first fetch, high at the second fetch and moderately high at the third fetch. Thus there is qualitative evidence that the ripple layer is dynamically significant. However, it is felt that the precision of the mean squared deviations is not high enough for a quantitative assessment at this time. It is also felt that a necessary prerequisite to any quantitative investigation is the derivation of the energy balance for the ripple layer, as Hasselmann (1971) has suggested that the potential energy changes experienced by the ripples cancel out the work done by his version

Reproduced with permission of the copyright owner. Further reproduction prohibited without permission.

of the mechanism discussed in §3. Thus an extension of the results of §3 to include the energy balance for the ripple layer should be completed prior to any detailed experimentation.

Some implications of the rolling-breaking mechanism (shown in fig. 23) will now be given.

The importance of the formation of stagnation points and the subsequent amplitude limitation through rolling-breaking lies in the fact that this will often occur prior to limiting through the formation of sharp crests and the attendant leading-edge ripple generation [Longuet-Higgins (1963), Crapper (1970)].

It is well known that a wavy interface between two fluids increases the flux of heat across the interface. This was shown for laminar wave motion by O'Brien (1967). He considered the transport of heat across a liquid layer supporting a finite amplitude Gerstner wave. It would be of great interest to examine this problem in the context of the rolling-breaking wave, as the existence of a periodic turbulent patch provides a mechanism for increased transport from the surface to the interior of the liquid layer.

Reproduced with permission of the copyright owner. Further reproduction prohibited without permission.

§9 CONCLUSIONS

This investigation has been aimed at contributing to a better understanding of the role of short waves and ripples and of wind drift on the dynamics of longer finite amplitude gravity waves.

According to the 'maser' mechanism of wind wave generation proposed by Longuet-Higgins (1969b), the ripples and short waves play a central role in the wind-wave interaction process. A theoretical analysis of this model by Hasselmann (1971) claiming that the 'maser' mechanism was not viable was analyzed in detail. Hasselmann's analysis was found to be unconvincing because of implicit fundamental assumptions whose consequences were not estimated. An alternate analysis which circumvents these difficulties has been presented in which the coupling between the ripple (and short wave) layer and the interior long wave flow is established. It was found that if viscous effects and wind drift are ignored, then the modifications to the long wave field are expressible as changes to the long wave free surface boundary conditions. In a frame moving with the long wave, it was found that at any given long wave phase point:

(a) the modification to the normal velocity boundary condition for the long wave is given by the product of the short to long wavelength ratio ε and the tangential gradient of integrated tangential ripple velocity across the ripple layer.

Reproduced with permission of the copyright owner. Further reproduction prohibited without permission.

(b) the modification to the pressure boundary condition for the long wave is given by the product of the characteristic short to long wavelength ratio ε and the tangential gradient of the shear radiation stress of the ripple layer. Furthermore, the ripple layer exerts a tangential stress at the long wave boundary given by the product of ε and the tangential gradient of the normal radiation stress of the ripple layer.

For small amplitude ripples, the tangential stress was found to be the dominant term in the coupling between the long wave and the ripple layer dynamics. It was concluded that an examination of the energy balance for the ripple layer was necessary in order to correctly assess the viability of the 'maser' mechanism. However, preliminary experimental evidence in support of a significant dynamic coupling was encouraging.

Another important aspect of the effects of short waves and wind drift on fairly steep, long gravity waves was observed and described. It involves a previously unreported rolling-breaking mechanism which will often occur prior to the usual form of amplitude-limiting associated with the development of sharp crests [Longuet-Higgins (1963), Crapper (1970)]. An analysis of the mechanism leading up to the breaking is given and its predictions were found to be in close agreement with measurements and observations reported in this study. The model is also able to account qualitatively for some of the subsidiary observations. An important consequence of the mechanism is that it provides source of increased

Reproduced with permission of the copyright owner. Further reproduction prohibited without permission.

transport from the surface to the interior of a fluid. An extension of the work of O'Brien (1967) on the increased heat flux through a laminar wavy liquid layer is suggested in this context.

Reproduced with permission of the copyright owner. Further reproduction prohibited without permission.

APPENDIX I

INVERSION OF THE TRANSFORMATION BETWEEN (ξ, η) AND (x, z) COORDINATES.

Given the orthogonal transformation of coordinates

$$\xi = x - a e^{z} \sin x \qquad \ldots\ \text{I.1}$$

$$\eta = z - a e^{z} \cos x \qquad \ldots\ \text{I.2}$$

we wish to obtain x, z as functions of ξ and η. From the reasoning given in the text, the existence of the inverse is guaranteed for the values of a (the long wave slope parameter) relevant to this problem. Hence we seek an inversion in terms of power series in a as follows:

Let $x = x_0(\xi,\eta) + a\, x_1(\xi,\eta) + a^2 x_2(\xi,\eta) + O(a^3)$

$z = z_0(\xi,\eta) + a\, z_1(\xi,\eta) + a^2 z_2(\xi,\eta) + O(a^3)$

Then we begin by calculating

$$e^{z}(\cos x + i \sin x) = e^{z_0} e^{a z_1} e^{a^2 z_2} \cdots \left[e^{i x_0} e^{i a x_1} e^{i a^2 x_2} \cdots \right]$$

$$= e^{z_0} e^{i x_0} \left\{ \left[1 + a z_1 + \tfrac{a^2}{2} z_1^2 + \cdots \right] \left[1 + a^2 z_2 + \cdots \right] \left[1 + O(a^3) \right] \cdots \right\}$$

$$\times \left\{ \left[1 + i a x_1 - \tfrac{a^2}{2} x_1^2 \right] \left[1 + i a^2 x_2 + \cdots \right] \left[1 + O(a^3) \right] \left[1 \cdots \right] \cdots \right\}$$

$$= e^{z_0} e^{i x_0} \left\{ 1 + a z_1 + a^2 \left[z_1^2/2 + z_2 \right] + O(a^3) \right\} \left\{ 1 + i a x_1 + a^2 \left(i x_2 - \tfrac{x_1^2}{2} \right) + O(a^3) \right\}$$

$$= e^{z_0} (\cos x_0 + i \sin x_0) \left\{ 1 + a(z_1 + i x_1) + a^2 \left[\left(\tfrac{z_1^2}{2} + z_2 - \tfrac{x_1^2}{2} \right) + i (x_1 z_1 + x_2) \right] + O(a^3) \right\}$$

$$= e^{z_0} \cos x_0 \left\{ 1 + a z_1 + a^2 \left(\tfrac{z_1^2}{2} + z_2 - \tfrac{x_1^2}{2} \right) + O(a^3) \right\} + e^{z_0} \sin x_0 \left\{ -a x_1 - a^2 (x_1 z_1 + x_2) + O(a^3) \right\}$$

$$+ i\, e^{z_0} \cos x_0 \left\{ a x_1 + a^2 (x_1 z_1 + x_2) + O(a^3) \right\} + i\, e^{z_0} \sin x_0 \left\{ 1 + a z_1 + a^2 \left(\tfrac{z_1^2}{2} + z_2 - \tfrac{x_1^2}{2} \right) + O(a^3) \right\}$$

Reproduced with permission of the copyright owner. Further reproduction prohibited without permission.

Equating real and imaginary parts

$$e^{z}\sin x = e^{z_0}\cos x_0\left[ax_1 + O(a^2)\right] + e^{z_0}\sin x_0\left[1 + az_1 + O(a^2)\right]$$

$$e^{z}\cos x = e^{z_0}\cos x_0\left[1 + az_1 + O(a^2)\right] - e^{z_0}\sin x_0\left[ax_1 + O(a^2)\right]$$

Using these results in I.1 and I.2 we have

$$\xi = (x_0 + ax_1 + a^2x_2 + O(a^3)) - e^{z_0}\cos x_0\left[a^2x_1 + O(a^3)\right] - e^{z_0}\sin x_0\left[a + a^2z_1 + O(a^3)\right]$$

$$= x_0 + a(x_1 - e^{z_0}\sin x_0) - a^2(x_2 - x_1e^{z_0}\cos x_0 - z_1e^{z_0}\sin x_0) + O(a^3) \quad \ldots\ \text{I.3}$$

$$\eta = (z_0 + az_1 + a^2z_2 + O(a^3)) - e^{z_0}\cos x_0\left[a^2z_1 + O(a^3)\right] + e^{z_0}\sin x_0\left[a^2x_1 + O(a^3)\right]$$

$$= z_0 + a(z_1 - e^{z_0}\cos x_0) + a^2(z_2 - z_1e^{z_0}\cos x_0 + x_1e^{z_0}\sin x_0) + O(a^3)$$

$\ldots\ \text{I.4}$

Hence equating powers of a in I.3 and I.4 we have

a^0: $\quad \xi = x_0 \quad , \quad \eta = z_0$

a^1: $\quad 0 = x_1 - e^{z_0}\sin x_0 \longrightarrow x_1 = e^{\eta}\sin\xi$

$\quad 0 = z_1 - e^{z_0}\cos x_0 \longrightarrow z_1 = e^{\eta}\cos\xi$

a^2: $\quad 0 = x_2 - x_1e^{z_0}\cos x_0 - z_1e^{z_0}\sin x_0$

$\longrightarrow x_2 = e^{2\eta}\sin\xi\cos\xi + e^{2\eta}\cos\xi\sin\xi$

$\therefore x_2 = e^{2\eta}\sin 2\xi$

$0 = z_2 - z_1e^{z_0}\cos x_0 + x_1e^{z_0}\sin x_0$

$\longrightarrow z_2 = e^{2\eta}\cos\xi\cos\xi - e^{2\eta}\sin\xi\sin\xi$

$\therefore z_2 = e^{2\eta}\cos 2\xi$

Thus we have

$$x = \xi + ae^{\eta}\sin\xi + a^2e^{2\eta}\sin 2\xi + O(a^3)$$

$$z = \eta + ae^{\eta}\cos\xi + a^2e^{2\eta}\cos 2\xi + O(a^3)$$

which is the desired result. This can in principle be extended to any order in a.

Reproduced with permission of the copyright owner. Further reproduction prohibited without permission.

APPENDIX II

DERIVATION OF THE CURVATURE IN THE (ξ, η) FRAME.

In Cartesian coordinates, the expression for the curvature κ of the two-dimensional curve $F(x,z) = 0$ is given by (Courant Vol.II, p.125)

$$\kappa = \frac{F_{xx}F_z^2 - 2F_{xz}F_xF_z + F_{zz}F_x^2}{(F_x^2 + F_z^2)^{3/2}} \quad \ldots\ldots \text{II.1}$$

Transforming to the (ξ,η) coordinate system, let $F(x,z) = 0$ transform to $G(\xi,\eta)=0$. Then we use the properties of the transformation given in the text (p.28) to derive the corresponding expression for the curvature in the (ξ,η) frame.

Now
$$F_x = G_\xi \xi_x + G_\eta \eta_x$$
$$F_{xx} = G_{\xi\xi}\xi_x^2 + G_\xi \xi_{xx} + G_{\eta\eta}\eta_x^2 + G_\eta \eta_{xx}$$
$$F_z = G_\xi \xi_z + G_\eta \eta_z$$
$$F_{zz} = G_{\xi\xi}\xi_z^2 + G_\xi \xi_{zz} + G_{\eta\eta}\eta_z^2 + G_\eta \eta_{zz}$$
$$F_{xz} = G_{\xi\xi}\xi_x\xi_z + G_\xi \xi_{xz} + G_{\eta\eta}\eta_x\eta_z + G_\eta \eta_{xz}$$

Also
$$\xi_x = \eta_z = 1 - ae^z\cos x \sim 1 - ae^\eta \cos\xi + O(a^2)$$
$$\xi_z = -\eta_x = -ae^z \sin x \sim -ae^\eta \sin\xi + O(a^2)$$
$$\xi_{xx} = \eta_{xz} = ae^z \sin x \sim ae^\eta \sin\xi + O(a^2)$$
$$\xi_{zz} = -\eta_{xz} = -ae^z \sin x \sim -ae^\eta \sin\xi + O(a^2)$$

$$\therefore F_x = G_\xi(1 - ae^\eta\cos\xi + O(a^2)) + G_\eta(ae^\eta \sin\xi + O(a^2))$$
$$= G_\xi - ae^\eta(G_\xi \cos\xi - G_\eta \sin\xi) + O(a^2).$$

Reproduced with permission of the copyright owner. Further reproduction prohibited without permission.

$$F_{xx} = G_{\xi\xi}(1-2ae^{\eta}\cos\xi+O(a^2)) + G_{\xi}(ae^{\eta}\sin\xi)+G_{\eta\eta}(O(a^2)) - G_{\eta}(ae^{\eta}\cos\xi)$$

$$= G_{\xi\xi} + ae^{\eta}(-2G_{\xi\xi}\cos\xi + G_{\xi}\sin\xi - G_{\eta}\cos\xi) + O(a^2)$$

Also we have

$$F_{z} = -G_{\xi}\, ae^{\eta}\sin\xi + G_{\eta}(1-ae^{\eta}\cos\xi) + O(a^2)$$

$$= G_{\eta} - ae^{\eta}(G_{\xi}\sin\xi + G_{\eta}\cos\xi) + O(a^2)$$

$$F_{zz} = G_{\xi\xi}(O(a^2)) + G_{\xi}(-ae^{\eta}\sin\xi) + G_{\eta\eta}(1-2ae^{\eta}\cos\xi) + G_{\eta}(-ae^{\eta}\cos\xi) + O(a^2)$$

$$= G_{\eta\eta} - ae^{\eta}(G_{\xi}\sin\xi + 2G_{\eta\eta}\cos\xi + G_{\eta}\cos\xi) + O(a^2)$$

$$F_{xz} = G_{\xi\xi}(-ae^{\eta}\sin\xi) + G_{\xi}(-ae^{\eta}\cos\xi) + G_{\eta\eta}(ae^{\eta}\sin\xi) + G_{\eta}(ae^{\eta}\sin\xi) + O(a^2)$$

$$= ae^{\eta}(G_{\eta\eta}\sin\xi + G_{\eta}\sin\xi - G_{\xi\xi}\sin\xi - G_{\xi}\cos\xi) + O(a^2)$$

We now substitute these expressions into the expression for the curvature given above (II.1). Using straightforward algebra, it is readily shown that

$$K = \frac{G_{\xi\xi}G_{\eta}^2 + G_{\eta\eta}G_{\xi}^2 + O(a)}{\{G_{\xi}^2 + G_{\eta}^2 - 2ae^{\eta}[G_{\xi}^2+G_{\eta}^2]\cos\xi + O(a^2)\}^{3/2}}$$

Now set $G(\xi,\eta) = f(\xi) - \eta$ and we have

$$K = \frac{f_{\xi\xi}(-1)^2 + 0\cdot f_{\xi}^2 + O(a)}{\{f_{\xi}^2 + (-1)^2 - 2ae^{\eta}(f_{\xi}^2+1)\cos\xi + O(a^2)\}^{3/2}}$$

$$= \frac{f_{\xi\xi}(1+O(a))}{(1+f_{\xi}^2)^{3/2}}$$

Moreover, this relation holds at each instant if f is also a function of time.

Reproduced with permission of the copyright owner. Further reproduction prohibited without permission.

APPENDIX III

ERROR ANALYSIS FOR THE PHASE-AVERAGING COMPUTATIONS

The method of phase-averaging the wave probe data involved several computational stages. A searching routine located sets of data points [A(I)] lying within a preset amplitude band about zero and having an indicial (I) separation less than a preset value. The indices I_i belonging to a given set of data points satisfying the above criteria were averaged arithmetically to give the mean location for that zero-crossing. This was rounded-off to the nearest integer value. We denote this set of N indices of rounded-off averaged zero-crossings by $[I_j^o\ ,\ j = 1, N]$. The next phase of the routine was to classify the zero-crossings as positive, negative or indefinite according to the value of the data point before and after each group of points contributing to a given averaged zero-crossing. The set of positive averaged zero-crossings determined the number of complete wave cycles (L), beginning at the first positive zero index I_i^{op} mean difference between the indices of the consecutive positive zeroes I_k^{op} was calculated and rounded-off to provide an integral number (INT) of indices which made up the phase points for the averaged wave.

The phase-averaging procedure then computed

$$\overline{A}_k = \left\{ \sum_{i=1}^{L} A(I_i^{op} + k)/L \right\} \qquad \text{for } k = 1, \text{INT}$$

and

$$\overline{D_k^2} = \left\{ \sum_{i=1}^{L} A^2(I_i^{op} + k)/L \right\} \qquad \text{for } k = 1, \text{INT}$$

Reproduced with permission of the copyright owner. Further reproduction prohibited without permission.

That is, the positive-going averaged zero-crossings formed the set of initial phase points.

It can be seen from the diagram below that unless the phase interval matches the difference between consecutive positive zeroes, then the distribution of the phase-averaged deviation will not return to a value approaching that at the initial phase point and the distribution will be biased accordingly. For the mean phase-averaged profile, this effect should be minimal provided the intervals between consecutive zero-crossings have a symmetrical frequency distribution about the mean interval. We are therefore concerned primarily with the estimation of the bias associated with the distribution of squared deviations from the mean wave.

----- phase-averaged mean wave profile; ——— actual wave profile

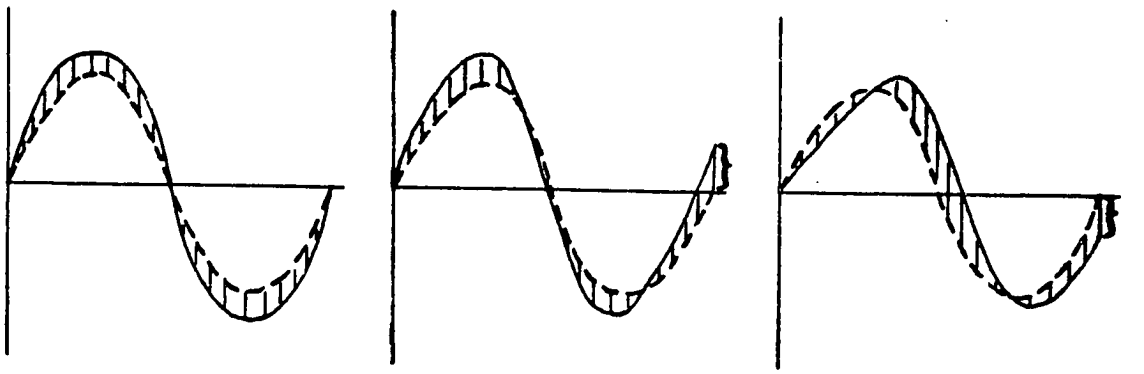

(a) frequency matches that of mean wave

(b) frequency greater than that of mean wave

(c) frequency less than that of mean wave

Let

$$\bar{\gamma} = a' \sin \bar{n} t \,, \qquad 0 < t < 2\pi/\bar{n}$$

be the computed phase-averaged mean wave profile (transformed into real time). Also let the profile for any single realization in the

Reproduced with permission of the copyright owner. Further reproduction prohibited without permission.

in the ensemble be given by

$$\gamma = (a' + \varepsilon) \sin (\bar{n} + \delta)t$$

ε is a random variable denoting the amplitude deviation, assumed small and δ is a random variable denoting the frequency deviation also assumed small.

If the frequency shift induced by δ were zero, we would obtain the correct phase averaged squared deviation distribution:

$$\overline{(\gamma - \bar{\gamma})^2} = \overline{[(a' + \varepsilon) \sin \bar{n}t - a' \sin \bar{n}t]^2} = \overline{\varepsilon^2} \sin^2 \bar{n}t$$

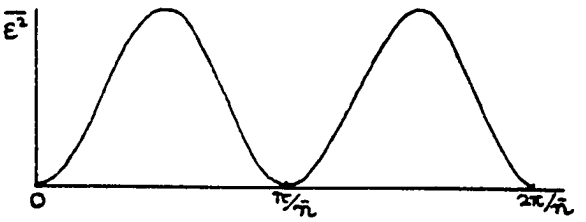

We wish to determine the bias induced by a non-zero δ. The computed phase-averaged, mean squared deviation distribution is given by

$$\begin{aligned}
\overline{(\gamma - \bar{\gamma})^2} &= \overline{[(a'+\varepsilon)\sin(\bar{n}+\delta)t - a'\sin \bar{n}t]^2} \\
&= \overline{[a'\sin(\bar{n}+\delta)t + \varepsilon \sin(\bar{n}+\delta)t - a'\sin \bar{n}t]^2} \\
&= \overline{\left[a' \sin \bar{n}t + (a'\cos \bar{n}t)\delta t + \varepsilon \sin \bar{n}t - a'\sin \bar{n}t\right]^2} + O(\delta^2, \varepsilon\delta, \varepsilon^2) \\
&= a'^2 \overline{\delta^2} t^2 \cos^2 \bar{n}t + 2a' \overline{\delta\varepsilon} \cos \bar{n}t \sin \bar{n}t + \overline{\varepsilon^2} \sin^2 \bar{n}t
\end{aligned}$$

Hence the distribution of the bias is given by

$$a'^2 \overline{\delta^2} t^2 \cos^2 \bar{n}t + a' \overline{\delta\varepsilon}\, t \sin 2\bar{n}t \quad \ldots\ldots \text{III.1}$$

To see whether this is a realistic estimator of the observed bias, we will examine one of the wave probe records. Using this

Reproduced with permission of the copyright owner. Further reproduction prohibited without permission.

formula it should be possible to make a first order correction towards reducing the large offset at the end of the phase interval.

We will examine the results of the three probes of record 5, the largest amplitude mechanically-generated wave situation reported in this investigation. In each case, the mean amplitude a' is taken as the amplitude of a sinusoid with the same variance. $\overline{\epsilon^2}$ is estimated from the crest values of the computed phase-averaged mean squared deviations. (According to expression III.1, the bias is expected to be least over the initial phase points. This implies that the crest values are not likely to be seriously in error). Also, the bias at the end of the phase interval depends linearly on the correlation $\overline{\delta\epsilon}$ between the amplitude and frequency deviations. For lack of direct evidence, we will assume that the long wave energy per cycle is conserved approximately. This implies that if the frequency is reduced, then the amplitude increases and vice versa. Thus we will assume

$$\frac{\overline{\delta\epsilon}}{(\overline{\delta^2})^{1/2}(\overline{\epsilon^2})^{1/2}} = -m \qquad , \qquad 0 \leq m < 1$$

We will use $m = 0.3$ to provide an initial estimate for the bias; m can be revised subsequently if the end bias is not well estimated. Finally, $\overline{\delta^2}$ is estimated from the computer output which listed the indices of the positive averaged zero-crossings and the deviations from the mean interval of the differences between consecutive positive zero-crossings.

Reproduced with permission of the copyright owner. Further reproduction prohibited without permission.

From the computer output, the following data has been calculated for record 5:

PROBE	a' cm	a'^2 cm^2	$\overline{\varepsilon^2}$ cm^2	$\overline{\delta^2}$ Hz^2	$[\overline{\delta^2}.\overline{\varepsilon^2}]^{\frac{1}{2}}$ cm. Hz
1	1.48	2.22	0.025	0.0010	.0050
2	1.62	2.60	0.05	0.0018	.0095
3	1.53	2.34	0.12	0.0028	.0183

The bias for the distributions is then given by

PROBE

1 $0.0022\ t^2 \cos^2 1.7t - 0.0074mt \sin 3.4t, \quad 0 \leq t \leq 3.69$

2 $0.0047\ t^2 \cos^2 1.7t - 0.0154mt \sin 3.4t, \quad 0 \leq t \leq 3.69$

3 $0.0066\ t^2 \cos^2 1.7t - 0.028mt \sin 3.4t, \quad 0 \leq t \leq 3.69$

These distributions are shown in the diagrams below. The two components of each bias expression are shown separately. It should be noted that the correlation coefficient is highly uncertain and our selected value of -0.3 might well range anywhere from $0 \leq m < 1$. The other component, ($\propto \overline{\delta^2}$) has been determined quantitatively from the data and is far more accurately determined.

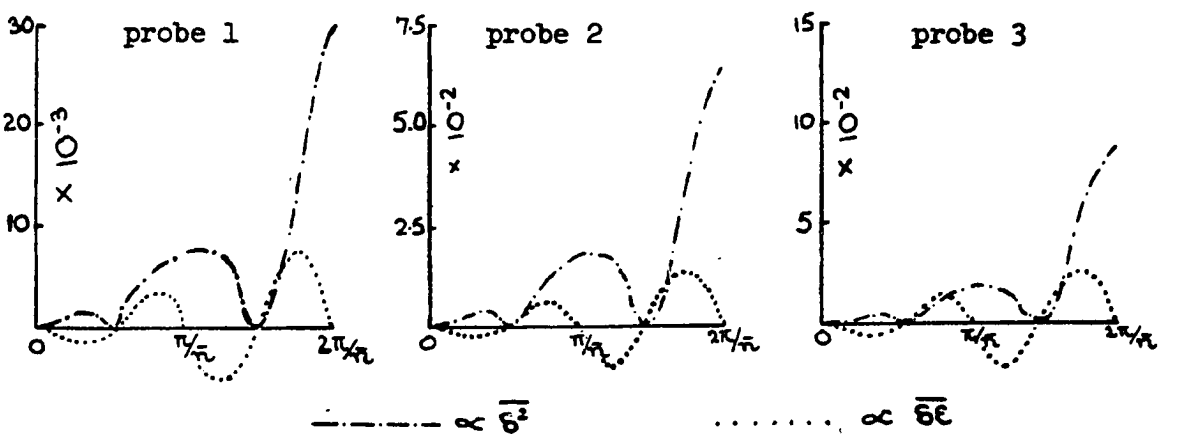

Reproduced with permission of the copyright owner. Further reproduction prohibited without permission.

By comparing these correction curves with the actual distributions given in figs. (20), (21) and (22), it can be seen that the positive offset at the end of the phase interval is well accounted for by the deterministic component ($\propto \overline{\delta^2}$) of the bias. It is also apparent that the first half of the phase interval is fairly free of bias for all but the largest values of m.

Another effect contributing to the measured mean squared deviation distributions was the fluctuations in amplitude and frequency introduced by the mechanical wavemaking system. The extent to which this affected the measured distributions was assessed in the absence of wind. The typical normalized root mean squared amplitude and frequency [$\frac{(\overline{\epsilon^2})^{1/2}}{a'}$, $\frac{(\overline{\delta^2})^{1/2}}{\pi}$] were determined for the long wave slope situations where $a = 0.16$ and $a = 0.28$ (a uniform probability density was assumed for ϵ and for δ).

For $a = 0.16$ $\left(\frac{[\overline{\epsilon^2}]^{1/2}}{a'}\right) \sim .007$; $\left(\frac{(\overline{\delta^2})^{1/2}}{a'}\right) \sim .015$

$a = 0.28$ $\left(\frac{[\epsilon^2]^{1/2}}{a'}\right) \sim .013$; $\left(\frac{(\overline{\delta^2})^{1/2}}{a'}\right) \sim .015$

Comparing these with the measured levels of mean squared deviations shown in figs. (17), (18), (19) and (20), (21), (22), it can be seen that the contribution due to the "noise" inherent in the wavemaking system is small.

It is felt therefore that the above provides a realistic first order correction scheme for the mean squared deviation distributions.

Reproduced with permission of the copyright owner. Further reproduction prohibited without permission.

APPENDIX IV

LISTINGS OF COMPUTER PROGRAMS USED IN THIS INVESTIGATION.

```
C     WAVE TANK PROJECT ---FIRST PROGRAM --- WT-A --- JUNE 72
C
C     THIS IS THE FIRST PROGRAM IN THE SLOPE METER LAB STUDY SERIES.
C
C     USE WT-B AFTER THIS PROGRAM TO CORRECT DATA FOR DIGITIZATION
C     ERRORS.
C
C     THIS PROGRAM UNPACKS THE CONDENSED-BINARY DATA TAPES FROM THE A/D
C     CONVERTER AND KENNEDY TAPE RECORDER SYSTEM. IT THEN PREPARES (FOR
C     EACH PROBE OF EACH RECORD) A TABLE SHOWING THE FREQUENCY-
C     DISTRIBUTION OF THE OCCURRENCE OF COUNTS OVER THE INTERVAL
C     FROM -256 TO +255 AND A TABLE SHOWING THE FREQ. DISTRIBUTION OF
C     THE FIRST DIFFERENCES BETWEEN COUNTS OVER 0 TO 511
C
C     NOREC = NUMBER OF RECORDS TO BE PROCESSED.
C     NOREC MUST NOT EXCEED 99.
C     IDEN = IDENTIFICATION LABEL --- INCLUDE DATE, ETC.
C
C     PROBE(I) = NAME  CODE FOR THE I-TH PROBE.
C     X(I),Y(I) = X,Y COORDINATES FOR THE I-TH. PROBE
C     X (FEET) INCREASES DOWNWIND ALONG TANK AXIS.
C     Y (INCHES) INCREASES ACROSS TANK TO LEFT , LOOKING DOWNWIND.
C
C     NOPRB = NUMBER OF PROBES .
C     LENREC = 12000,24000, OR 36000 --- THE NUMBER OF DATA POINTS IN
C     A COMBINED RECORD.
C     LENREC/NOPRB = THE NUMBER OF POINTS IN A PROBE RECORD.
C
C     WARNING --- IF NOPRB = 1, LENREC MUST NOT = 24000 OR 36000.
C     WARNING --- IF NOPRB = 2, LENREC MUST NOT = 36000.
C
C     SPLFRQ = FREQUENCY (HZ) AT WHICH A PROBE IS SAMPLED BY A/D
C     CONVERTER.
C
C     WIND = WIND SPEED (M/SEC) DURING EXPERIMENT.
C     WAVE = FREQUENCY (HZ) OF WAVES GENERATED MECHANICALLY DURING
C     EXPERIMENT.
C
C     NIX NOT = 0 MEANS DISCARD THE RECORD WITH NO PROCESSING IN WT-A
C     NIX = 0 MEANS PROCESS THE RECORD NORMALLY.
C
C     N1 NOT = 0 MEANS DISCARD THE RECORD AFTER PREPARING THE FREQUENCY
C     DISTRIBUTION TABLES.
C     N1 = 0 MEANS PROCESS THE RECORD NORMALLY.
C
C     NDUP = THE NUMBER OF RECORDS FOLLOWING WHICH HAVE SAME INPUT DATA.
C
C      NOTE --- EACH RECORD NEEDS A CARD WITH PROCESSING INFORMATION
C
C     NDUP REPEATS THE CARD FOR EACH SUBSEQUENT RECORD WITH THE
C     SAME PROCESSING INFORMATION.
C
C

      DIMENSION IDEN(12),M(12000)        ,IS(512),PROBE(5),X(5),Y(5),
```

Reproduced with permission of the copyright owner. Further reproduction prohibited without permission.

```
      1 DATA(9100),KIS(512)
        REWIND 9
        REWIND 10
        NDUP = 0
        READ (5,10) NOREC,IDEN
   10 FORMAT (I2,12A6)
        READ (5,36) (PROBE(I),X(I),Y(I),I=1,5)
   36 FORMAT (A6,2F8.3)
        WRITE(10) NOREC,IDEN
        DO 7777 KR=1,NOREC
        IF(NDUP.LE.0) GO TO 34
        NDUP=NDUP-1
        GO TO 35
   34   READ (5,30) NOPRB,LENREC,SPLFRQ,WIND,WAVE,NIX,N1,NDUP
   30 FORMAT (I1,I5,3F5.2,2I1,I2)
   35   CALL SREAD (DATA,9100,NPKWDS,KEOF,8)
        IF (KEOF.NE.+1) GO TO 100
        WRITE (6,101)
  101 FORMAT (1H1,25HEND OF FILE ON DATA TAPE.)
        GO TO 102
  100   IF(NIX.EQ.0) GO TO 107
        WRITE(6,108) KR
  108   FORMAT(1X///1X,6HRECORD,I3,15H NOT PROCESSED.)
        GO TO 7777
   107 IF(N1.NE.0) GO TO 109
        WRITE(10) KR,NOPRB,LENREC,SPLFRQ,WIND,WAVE
  109   NCOR = LENREC/4
        IF (NPKWDS.GT.NCOR) NPKWDS = NCOR
        MM = NPKWDS*4/NOPRB
        DO 8888 KP=1,NOPRB
        CALL UNPAK (DATA,NPKWDS,M,NOPRB,KP)
C
C       THIS SECTION PREPARES FREQUENCY DISTRIBUTION OF VOLTAGE VALUES
C
        DO 1000 I=1,512
        IS(I)=I-257
 1000 KIS(I) = 0
        WRITE (6,70) KR,PROBE(KP),X(KP),Y(KP),IDEN,MM,SPLFRQ,WAVE,WIND
   70   FORMAT (1H1,6HRECORD,I3,2H, ,A6,11H PROBE, X =,F7.3,5H, Y =,F7.3,
       11H,1X,12A6//1X,I5,24H NUMBERS, SAMPLE FREQ. =,
       2          F7.2, 17H HZ, WAVE FREQ. =,F5.2, 17H HZ, WIND SPEED =,
       3 F5.2,7H M/SEC.//)
        DO 2000 I=1,MM
        J = M(I) + 257
 2000 KIS(J) = KIS(J) + 1
        WRITE (6,90)
   90 FORMAT (1X,41HFREQUENCY-DISTRIBUTION OF VOLTAGE VALUES.//)
        CALL LIST (KIS,IS)
C
C       THIS SECTION PREPARES A FREQUENCY DISTRIBUTION OF FIRST
C       DIFFERENCES OF VOLTAGE VALUES.
C
        DO 2600 I=1,512
         IS(I)=I-1
 2600 KIS(I)=0
        MMM1=MM-1
        DO 2700 I=1,MMM1
        K = IABS (M(I)-M(I+1)) + 1
 2700 KIS(K) = KIS(K) + 1
        WRITE (6,80) KR,PROBE(KP),X(KP),Y(KP),IDEN,MM,SPLFRQ,WAVE,WIND
   80 FORMAT (1H1,6HRECORD,I3,2H, ,A6,11H PROBE,X =,F7.3,5H, Y =,F7.3,
       11H,1X,12A6//1X,I5,24H NUMBERS, SAMPLE FREQ. =,
       2          F7.2, 17H HZ, WAVE FREQ. =,F5.2, 17H HZ, WIND SPEED =,
       3 F5.2,7H M/SEC.//)
        WRITE (6,97)
   97 FORMAT (1X,62HFREQUENCY-DISTRIBUTION OF FIRST DIFFERENCES OF VOLTA
       1GE VALUES.//)
        CALL LIST (KIS,IS)
        IF (N1.NE.0) GO TO 8888
        WRITE(10) KP,PROBE(KP),X(KP),Y(KP),MM
        WRITE(10) (M(I),I=1,MM)
 8888 CONTINUE
 7777 CONTINUE
  102   END FILE 10
        END FILE 10
        END FILE 10
        REWIND 9
        REWIND 10
        STOP
        END
```

Reproduced with permission of the copyright owner. Further reproduction prohibited without permission.

```
C     WAVE TANK PROJECT,---SECOND PROGRAM--- -WT-B--  JAN,1973
C
C     USE THIS PROGRAM AFTER WT-A.
C
C     USING THE APPROPRIATE OPTIONS, THIS PROGRAM WILL ---
C
C     (*) CONVERT COUNTS FROM THE A/D TO PHYSICAL DISPLACEMENTS.
C
C     (*) DETECT EXTREME VALUES OF AMPLITUDE AND FIRST DIFFERENCE
C     ACCORDING TO THE LIMITS PRESET (BASED ON WT-A),AND INTERPOLATE
C     LINEARLY FOR THESE EXTREME VALUES. IN CASE THE NUMBER OF
C     CONSECUTIVE BAD VALUES EXCEEDS TWO, THIS IS PRINTED OUT AND THE
C     PROCESSING FOR THAT PROBE IS DISCONTINUED.
C
C     (*) PREPARE A NEW TABLE OF THE FREQUENCY DISTRIBUTION OF VALUES
C     AND A NEW TABLE OF THE FREQUENCY DISTRIBUTION OF FIRST DIFFERENCES
C     BETWEEN SUCCESSIVE VALUES.
C
C
C     NOUT = 0 MEANS PREPARE AN OUTPUT TAPE CONTAINING ALL RECORDS
C     FOR WHICH NIX=0. THOSE RECORDS FOR WHICH NIX NOT =0 ARE DISCARDED
C     AT THE END OF THIS PROGRAM.
C
C     CALIB(I) = THE CONVERSION FACTOR IN UNITS OF CM/COUNT OF THE A/D.
C
C     CALIB IS SPECIFIED ONCE FOR EACH RECORD
C
C     NIX IS SPECIFIED ONCE FOR EACH RECORD.
C     (A BLANK CARD IS EQUIVALENT TO NIX=0.)
C
C
      DIMENSION IDEN(12),A(12000),M(12000),PROBE(5),IS(512),JS(512),
     *AHIGH(5,5), ALOW(5,5), ABSDIF(5,5),KIS(512),X(5),Y(5),CALIB(5) ,
     *CORRP(5),CORRN(5)
      EQUIVALENCE (A(1),M(1))
      REWIND 10
      DO 4600 I=1,512
      IS(I)=I-257
       JS(I)=I-1
 4600 CONTINUE
      READ(5,13) NOUT
  13  FORMAT(I1)
      READ(5,8824) NLOST
 8824 FORMAT(I2)
      READ(10) NOREC,IDEN
      NORECC =NOREC-NLOST
      IF (NOUT.NE.0) GO TO 110
      REWIND 9
      WRITE (9) NOREC,IDEN
      GO TO 100
  110 WRITE (6,120)
  120 FORMAT (1H1,46HNO OUTPUT TAPE HAS BEEN PREPARED FOR THIS RUN.)
  100 DO 400  JK=1,NORECC
      READ(5,30) NIX
  30  FORMAT(I1)
```

Reproduced with permission of the copyright owner. Further reproduction prohibited without permission.

```
      READ (10) KR,NOPRB,LENREC,SPLFRQ,WIND,WAVE
      IF (NCUT.NE.0.OR.NIX.NE.0) GO TO 150
      WRITE (9) KR,NOPRB,LENREC,SPLFRQ,WIND,WAVE
  150 DO 500 IJ=1,NOPRB
      READ(5,11) CALIB(IJ),CORRP(IJ),CORRN(IJ)
   11 FORMAT(3F10.6)
      READ(10) KP,PROBE(KP),X(KP),Y(KP),MM
      IF (NCUT.NE.0.OR.NIX.NE.0) GO TO 200
      WRITE(9) KP,PROBE(KP),X(KP),Y(KP),MM
      WRITE (6,71) KR,PROBE(KP),X(KP),Y(KP),IDEN,MM,SPLFRQ,WAVE,WIND
   71 FORMAT (1H1,6HRECORD,I3,2H, ,A6,11H PROBE,X =,F7.3,5H, Y =,F7.3,
     11H,1X,12A6//1X,I5,24H NUMBERS, SAMPLE FREQ. =,
     2          F7.2, 17H HZ, WAVE FREQ. =,F5.2, 17H HZ, WIND SPEED =,
     3 F5.2,7H M/SEC.//)
      GO TO 301
  200 WRITE(6,15) JK
   15 FORMAT(1HO,7HRECORD ,I2,30H HAS NOT BEEN WRITTEN ON TAPE.)
  301 READ (10) (M(K),K=1,MM)
      READ(5,555) AHIGH(JK,IJ),ALOW(JK,IJ),ABSDIF(JK,IJ)
  555 FORMAT(3F10.2)
      WRITE(6,744)AHIGH(JK,IJ),ALOW(JK,IJ),ABSDIF(JK,IJ)
  744 FORMAT(1HO,13HUPPER LIMIT =,F10.2,1H,,5X,13HLOWER LIMIT =,F10.2,
     *1H,,5X,26HMAXIMUM FIRST DIFFERENCE =,F10.2)
      AHI  =AHIGH(JK,IJ)*CALIB(IJ)
      ALO  = ALOW(JK,IJ) *CALIB(IJ)
      ABSDFF = ABSDIF(JK,IJ)*CALIB(IJ)
C
C     TO ESTABLISH THE FIRST GOOD VALUE
C
C
      DO 222 KU=1,MM
  222 A(KU)=CALIB(IJ)*FLOAT(M(KU))
      N=0
      K=1
  111 IF(A(K).GE.ALO .AND. A(K).LE.AHI .AND. ABS(A(K+1)-A(K)).LE.
     *ABSDFF) GO TO 105
      K=K+1
      GO TO 111
  105 INIT=K+1
      IF(INIT-3) 77,55,757
   55 A(1)=2.0*A(2)-A(3)
      GO TO 77
  757 WRITE(6,129) (A(K),K=1,5)
  129 FORMAT(1HO,2X,46HMORE THAN ONE BAD VALUE AT BEGINNING OF RECORD/
     *5X,37HFIRST FIVE VALUES OF DATA SERIES ARE ,5F15.2)
   77 WRITE(6,1150) INIT,A(K),A(K+1)
 1150 FORMAT(1HO,5X,28HINDEX OF FIRST GOOD VALUE = ,I5,1H.,
     *15H PRIOR VALUE = ,F10.2,1H,,14H NEXT VALUE = ,F10.2)
      N=N+1
      IF(N.EQ.1) GO TO 2111
      WRITE(6,87)
   87 FORMAT(1HO,5X,47HINITIAL VALUE SCHEME FAILED. PASS TO NEXT PROBE)
      GO TO 500
C
C     DETECTION OF EXTREME VALUES OF SLOPE AND AMPLITUDE AND
C     SUBSEQUENT INTERPOLATION FOR THE EXTREME VALUES.
```

Reproduced with permission of the copyright owner. Further reproduction prohibited without permission.

```
 2111 DO 50 K=INIT,MM
      IF(A(K).LT.ALO) WRITE(6,444) K,A(K)
  444 FORMAT(1HO,5X,26HTHE DATA POINT WITH INDEX ,I5,13H AND VALUE = ,
     *F10.2,12H IS TOO LOW.)
      IF(A(K).GT.AHI) WRITE(6,544) K,A(K)
  544 FORMAT(1HO,5X,26HTHE DATA POINT WITH INDEX ,I5,13H AND VALUE = ,
     *F10.2,13H IS TOO HIGH.)
      IF(A(K).GT.AHI.OR.A(K).LT.ALO) GO TO 60
      IF(ABS(A(K)-A(K-1)).GT.ABSDFF) GO TO 60
      GO TO 50
   60 IF(ABS(A(K+1)-A(K-1)).GT.2.0*ABSDFF) GO TO 83
      A(K)=(A(K+1)+A(K-1))/2.0
      WRITE(6,65) K,A(K)
   65  FORMAT(1HO,5X,26HTHE DATA POINT WITH INDEX ,I5,
     *18H AND WITH VALUE = ,F10.2,
     *46H HAS BEEN INTERPOLATED BASED ON ONE BAD VALUE.)
      GO TO 50
   83  IF(ABS(A(K+2)-A(K-1)).GT.3.0*ABSDFF) GO TO 93
      A(K)=A(K-1)+(A(K+2)-A(K-1))/3.0
      WRITE(6,85) K,A(K)
   85  FORMAT(1HO,5X,26HTHE DATA POINT WITH INDEX ,I5,
     *18H AND WITH VALUE = ,F10.2,
     *47H HAS BEEN INTERPOLATED BASED ON TWO BAD VALUES.)
      GO TO 50
   93 WRITE(6,72)
   72 FORMAT(1HO,5X,43HMORE THAN TWO CONSECUTIVE BAD VALUES EXIST.)
      IF(K.LE.11995) WRITE(6,82) K,A(K-1),A(K),A(K+1),A(K+2),A(K+3),
     *A(K+4),A(K+5)
   82 FORMAT(1HO,5X,26HTHE DATA POINT WITH INDEX ,I5,
     *56H IS THE SECOND IN THE FOLLOWING SET OF SUCCESSIVE VALUES/
     *7F15.2)
      WRITE(6,49)
   49 FORMAT(1HO,5X, 40HPROCESSING DISCONTINUED FOR THIS  PROBE.)
      GO TO 500
   50 CONTINUE
      WRITE(6,119)
  119 FORMAT(1HO,1X,31HNO MORE EXTREME VALUES DETECTED)
C     REMOVE RECORD MEAN
      AVE=0.0
      DO 26 IR=1,MM
   26 AVE=AVE+A(IR)
      AVE=AVE/FLOAT(MM)
      DO 28 IP=1,MM
   28 A(IP)=A(IP)-AVE
      DO 223 KI=1,MM
      IF(A(KI).LT.-1.136) GO TO 1847
      IF (A(KI).GT.+1.136) GO TO 1872
      GO TO 223
 1847 A(KI)=A(KI)*CORRN(IJ)/CALIB(IJ)
      GO TO 223
 1872 A(KI)=A(KI)*CORRP(IJ)/CALIB(IJ)
  223 CONTINUE
      IF (NCUT.NE.0.OR.NIX.NE.0) GO TO 147
      WRITE(9) (A(K),K=1,MM)
```

Reproduced with permission of the copyright owner. Further reproduction prohibited without permission.

```
C     THIS SECTION PREPARES FREQUENCY DISTRIBUTION OF AMPLITUDE VALUES.
C
 147  DO 1000 I=1,512
 1000 KIS(I) = 0
      WRITE (6,70) KR,PROBE(KP),X(KP),Y(KP),IDEN,MM,SPLFRQ,WAVE,WIND
  70  FORMAT (1H1,6HRECORD,I3,2H, ,A6,11H PROBE, X =,F7.3,5H, Y =,F7.3,
     11H,1X,12A6//1X,I5,24H NUMBERS, SAMPLE FREQ. =,
     2          F7.2, 17H HZ, WAVE FREQ. =,F5.2, 17H HZ, WIND SPEED =,
     3 F5.2,7H M/SEC.//)
      DO 2000 I=1,MM
      M(I)=A(I)
      J = M(I) + 257
 2000 KIS(J) = KIS(J) + 1
      WRITE (6,90)
  90  FORMAT (1X,41HFREQUENCY-DISTRIBUTION OF AMPLTDE VALUES.//)
      CALL LIST (KIS,IS)
C
C     THIS SECTION PREPARES A FREQUENCY DISTRIBUTION OF FIRST
C     DIFFERENCES OF AMPLTDE VALUES.
C
      DO 2600 I=1,512
 2600 KIS(I)=0
      LM1=MM-1
      DO 2700 I=1,LM1
      K = IABS (M(I)-M(I+1)) + 1
 2700 KIS(K) = KIS(K) + 1
      WRITE (6,80) KR,PROBE(KP),X(KP),Y(KP),IDEN,MM,SPLFRQ,WAVE,WIND
  80  FORMAT (1H1,6HRECORD,I3,2H, ,A6,11H PROBE, X =,F7.3,5H, Y =,F7.3,
     11H,1X,12A6//1X,I5,24H NUMBERS, SAMPLE FREQ. =,
     2          F7.2, 17H HZ, WAVE FREQ. =,F5.2, 17H HZ, WIND SPEED =,
     3 F5.2,7H M/SEC.//)
      WRITE (6,97)
  97 FORMAT (1X,62HFREQUENCY-DISTRIBUTION OF FIRST DIFFERENCES OF AMPLT
     1DE VALUES.//)
      CALL LIST (KIS,JS)
 500  CONTINUE
 400  CONTINUE
      END FILE 9
      END FILE 9
      END FILE 9
      REWIND 9
      REWIND 10
      STOP
      END
```

Reproduced with permission of the copyright owner. Further reproduction prohibited without permission.

```
C     THIRD PROGRAM---WT-CC--- MD HALL WAVE TANK ----JAN,1973.
C     THIS PROGRAM DOES THE FOLLOWING---
C
C     IT SUBTRACTS OUT THE MEAN AND LINEAR TREND
C
C     IT FINDS THE POSITIVE GOING MEAN ZERO CROSSINGS AND DETERMINES
C     THE REFERENCE POINTS FOR THE PHASE AVERAGING.MORE DETAILS BELOW.
C
C     IT COMPUTES AND PLOTS THE PHASE-AVERAGED DISTRIBUTION OF THE
C     MEAN LONG WAVE AND OF THE MEAN SQUARED DEVIATION DUE TO THE
C     SMALLER SCALE WAVES.
C
C     NOUT=0 MEANS PREPARE AN OUTPUT TAPE FOR ALL RECORDS.
C     IF NOUT NOT = 0 THEN NO OUTPUT TAPE IS WRITTEN.
C
C     NOPLOT=0 MEANS A CALCOMP PLOT TAPE WILL BE GENERATED
C
C     IF  NPHASE=0 THEN A PHASE-AVERAGING OPERATION WILL BE DONE. TO
C     BYPASS THIS PROCESS FOR ANY RECORD SET  NPHASE.NE.0
C
C
C     THIS PROGRAM ALSO ANALYSES THE AMPLITUDE PROBE DATA FOR
C     EACH RECORD (FOR WHICH NIX = 0 IN THE PREVIOUS PROGRAM). AND FINDS-
C
C     (*) THE LOCATION OF EACH ZERO. (USING A DELTA - BAND ABOUT ZERO,
C     THE COMPONENTS BELONGING TO ANY GIVEN ZERO-CROSSING SET ARE AVER-
C     AGED TO GIVE THAT PARTICULAR ZERO.)
C
C     (*) THE NATURE OF THE ZERO (POSITIVE-GOING, NEGATIVE-GOING, OR
C     INDEFINITE IN CASE OF AN IRREGULARITY)
C
C     (*) THE POSITION OF THE FIRST POSITIVE-GOING ZERO IN THE DATA
C     SERIES.
C
C     (*) THE NUMBER OF CYCLES BEGINNING AT THE FIRST POSITIVE ZERO.
C
C     (*) THE AVERAGE INTERVAL BETWEEN POSITIVE-GOING ZEROS.
C
C     DELTA IS THE AMPLITUDE OF THE BAND ABOUT ZERO FOR ASSOCIATING A
C     GIVEN DATA POINT WITH A GIVEN ZERO.
C
C     LIMFRQ IS THE UPPER LIMIT GOVERNING THE SEPARATION BETWEEN DATA
C     POINTS BELONGING TO THE SAME ZERO.
C
C     NZ =  INDEX OF THE AVERAGED ZERO
C     NCOMP(NZ) = NO. OF COMPONENTS FORMING THE NZ'TH ZERO
C     KZ IS THE NAME OF THE ARRAY OF DATA PTS SATISFYING Z-C CRITERION
C     FOR ANY GIVEN NZ.
C
      DIMENSION A(12000),PROBE(5),IDEN(12),X(5),Y(5),KZ(20),ZERO(1200),
     1          NZEROT(1200),SIGN(1200),NZERO(440)          ,DIFF(440),
     2SM(3),AVSM(3),ADIFF(2),ASUM(32),ASQSUM(32),AVAR(32),APHASE(32)
      EQUIVALENCE (NZEROT(1),ZERO(1),NZERO(1))
      REWIND 9
      READ(5,11) NOUT,NOPLOT
```

Reproduced with permission of the copyright owner. Further reproduction prohibited without permission.

```
   11  FORMAT(I1,I1)
       READ(5,15) NLOST
   15  FORMAT(I2)
       READ(9) NOREC,IDEN
       IF(NOUT.NE.0) GO TO 1000
       REWIND 10
       WRITE(10) NOREC,IDEN
 1000  NORECC=NOREC-NLOST
       DO 17 IA=1,NORECC
       READ( 9) KR,NOPRB,LENREC,SPLFRQ,WIND,WAVE
       IF(NOUT.NE.0) GO TO 200
       WRITE(10) KR,NOPRB,LENREC,SPLFRQ,WIND,WAVE
   200 DO 19 IB=1,NOPRB
       READ(9) KP,PROBE(KP),X(KP),Y(KP),MM
       READ(5,20) LIMFRQ,DELTA
   20  FORMAT(I2,F10.5)
       READ(5,16)  NPHASE
   16  FORMAT(I1)
       WRITE (6,50) KR,PROBE(KP),X(KP),Y(KP),IDEN,MM,SPLFRQ,WAVE,WIND,
      *DELTA, LIMFRQ
   50  FORMAT (1H1,6HRECORD,I3,2H, ,A6,11H PROBE,X = ,F7.3,5H, Y =,F7.3,
      11H,1X,12A6//1X,I5,24H NUMBERS, SAMPLE FREQ. =,
      2          F7.2, 17H HZ, WAVE FREQ. =,F5.2, 17H HZ, WIND SPEED =,
      3 F5.2,7H M/SEC.//10X,8HDELTA = ,F10.5,10X,9HLIMFRQ = ,I3)
       IF(NOUT.NE.0) GO TO 300
       WRITE(10) KP,PROBE(KP),X(KP),Y(KP),MM
   300 READ(9) (A(K),K=1,MM)
       IF(KR.NE.7) GO TO 19
       DO 23 K=1,3
       SM(K)=0.0
       DO 25 IR=1,4000
       IRR=IR+(K-1)*4000
       SM(K)=SM(K)+A(IRR)
   25  CONTINUE
       AVSM(K)=SM(K)/4000.0
   23  CONTINUE
       ADIFF(1)=AVSM(2)-AVSM(1)
       ADIFF(2)=AVSM(3)-AVSM(2)
       AGRAD=(AVSM(3)-AVSM(1))/8000.0
       AMPAV=(AVSM(1)+AVSM(2)+AVSM(3)) /3.0
       DO 24 K=1,MM
   24  A(K)=A(K)-AMPAV-AGRAD*FLOAT(K-6000)
       WRITE(6,29) AMPAVE,ADIFF(1),ADIFF(2)
   29  FORMAT(1H0,10X,18HRECORD AVERAGE IS ,F10.7,5X,14HGRADIENTS ARE ,
      *F10.7,5H AND ,F10.7)
       IF(NOUT.NE.0) GO TO 400
       WRITE(10) (A(K),K=1,MM)
   400 IF( NPHASE.NE.0) GO TO 19
C
C      THIS SECTION FINDS LOCATION AND ORDER OF EACH Z-C FOR THE
C      AMPLITUDE PROBE.
C
        NZ=0
       N = 0
       K=1
   21  IF(ABS(A(K)).LE.DELTA) GO TO 31
```

Reproduced with permission of the copyright owner. Further reproduction prohibited without permission.

```
 27   K=K+1
      GO TO 21
 31   N=N+1
      KZ(N)=K
      IF(N.EQ.1) GO TO 27
      IF((KZ(N)-KZ(N-1)) .LE. LIMFRQ) GO TO 27
      NZ=NZ+1
      IF(NZ.EQ.1) GO TO 275
      NCOMP =N-1
      NZEROT(NZ) = 0
      NM1=N-1
      DO 40 IJK=1,NM1
      NZEROT(NZ)=NZEROT(NZ)+KZ(IJK)
 40   CONTINUE
      ZERO(NZ)=FLOAT(NZEROT(NZ))/FLOAT(NCOMP)
      IZ=IFIX(ZERO(NZ))
      IF((ZERO(NZ)-FLOAT(IZ)).GE.0.5) GO TO 42
      ZERO(NZ)=FLOAT(IZ)
      GO TO 43
 42   ZERO(NZ)=FLOAT(IZ+1)
 43   LM2=MM-30
      KZ1M1=KZ(1)-1
      KZNM11=KZ(NM1)+1
      DELTAM=-DELTA
      IF(                    (A(KZ1M1).LT.DELTAM).AND.(KZ(NM1).LT.LM2).AND.
     *                         (A(KZNM11).GT.DELTA)) GO TO 90
      IF(                    (A(KZ1M1).GT.DELTA ).AND.
     * (KZ(NM1).LT.LM2).AND.(A(KZNM11).LT.DELTAM)) GO TO 94
      GO TO 96
 90   SIGN(NZ) = +1.0
      GO TO 275
 94   SIGN(NZ) = -1.0
      GO TO 275
 96   SIGN(NZ)= 0.0
275   N=0
      K=K-1
      IF (K.LT.MM) GO TO 27
C
C     TO DETERMINE THE 1ST Z-C(IZERO), ITS POSITION IN THE ZERO SERIES
C    *(NC1POS), AND THE NO. OF +VE-GOING Z-C'S(NOPOS)
C
      NCNZ=0
      DO 167 NT=2,NZ
      IF(SIGN(NT).NE.0.0) GO TO 167
      NCNZ=NCNZ+1
167   CONTINUE
      NOPOS = 0
      DO 108 IN=2,NZ
      IF(SIGN(IN).NE.1.0) GO TO 108
      NOPOS=NOPOS+1
      MZERO(NOPOS)=IFIX(ZERO(IN))
      IF(NOPOS.NE.1) GO TO 108
      IZERO=MZERO(NOPOS)
      NC1POS=IN
108   CONTINUE
      NCCYCL=NOPOS-1
```

Reproduced with permission of the copyright owner. Further reproduction prohibited without permission.

```
C       CALCULATE MEAN FREQ. AND DEVIATION
C
      BASAVE = SPLFRQ/WAVE
      TOT=0.0
      DO 100 IE=1,NOCYCL
      IEP1=IE+1
      DIFF(IE)=FLOAT(MZERO(IEP1)-MZERO(IE))
      TOT=TOT+DIFF(IE)
  100 CONTINUE
      AVE=TOT/FLOAT(NOCYCL)
      INT =IFIX(AVE)
      WRITE(6,308)
  308 FORMAT(1H0,5X,23HMEAN INDEX OF POS. ZERO,10X,9HDEVIATION,10X,
     *10HDIFFERENCE)
      DO 55 IK=1,NOCYCL
      DEV     =(DIFF(IK)-AVE)/AVE
      WRITE(6,309)MZERO(IK),DEV     ,DIFF(IK)
  309 FORMAT(16X,I5,    19X,F8.3,12X,F8.2)
   55 CONTINUE
      NZ=NZ-NONZ
      WRITE(6,228) BASAVE,AVE,NZ,NONZ
  228 FORMAT(1H0,5X,57HTHE NOMINAL FREQUENCY BASED ON THE WAVEMAKER FREQ
     1UENCY = ,F10.2,/,5X,46HTHE COMPUTED FREQUENCY FROM AMPLITUDE PROBE
     2 = ,F10.2,/,5X,22H NO. OF TRUE ZEROES = ,I3,5X,26H    NO. OF FALSE
     3 ZEROES = ,I3)
      WRITE(6,158) NO1POS, IZERO, NOPOS, NOCYCL
  158 FORMAT(1H0,22HTHE ZERO WITH INDEX = ,I1,15H OCCURS AT K = ,I5,
     *20H IN THE DATA SERIES.,/,30H THE NO. OF POSITIVE ZEROES = ,I3,
     *1H,,30H THE NO. OF COMPLETE CYCLES = ,I3)
      DO 41 JA=1,INT
      APHASE(JA)=FLOAT(JA-1)
      ASUM(JA)=0.0
      ASQSUM(JA)=0.0
      DO 37 IE=1,NOCYCL
      IPH=MZERO(IE)+(JA-1)
      ASUM(JA)=ASUM(JA)+A(IPH)
      ASQSUM(JA)=ASQSUM(JA)+(A(IPH))**2
   37 CONTINUE
      ASUM(JA)=ASUM(JA)/FLOAT(NOCYCL)
      ASQSUM(JA)=ASQSUM(JA)/FLOAT(NOCYCL)
      AVAR(JA)=ASQSUM(JA)-(ASUM(JA))**2
      WRITE(6,14) ASUM(JA), AVAR(JA)
   14 FORMAT(1H0,5X,F10.5,10X,F10.5)
   41 CONTINUE
      IF(NOPLOT.NE.0) GO TO 19
      CALL LABELX(18,18HPHASE OF LONG WAVE)
      CALL LABELY (27,27HMEAN AMPLITUDE OF LONG WAVE)
      CALL TITLE(48,48HPHASE-AVERAGED LONG WAVE PROFILE OVER 425 CYCLES)
      CALL PLTNEW(APHASE,ASUM,28,01)
      CALL LABELX(18,18HPHASE OF LONG WAVE)
      CALL LABELY (37,37HMEAN SQUARED AMPLITUDE OF SHORT WAVES)
      CALL TITLE(46,48HPHASE-AVERAGED MEAN-SQUARED SHORT WAVE DISTRIB.)
      CALL RANGE(0.0,28.0,5.0,5.0)
      CALL PLTNEW(APHASE,AVAR, 28,01)
   19 CONTINUE
   17 CONTINUE
      REWIND 9
      IF(NOUT.NE.0) GO TO 700
      END FILE 10
      END FILE 10
      END FILE 10
      REWIND 10
  700 STOP
      END
```

Reproduced with permission of the copyright owner. Further reproduction prohibited without permission.

```
MT-FFT ---MD. HALL WAVE TANK--- JAN,1973

THIS PROGRAM COMPUTES THE SMOOTHED AMPLITUDE SPECTRUM FOR EACH
PROBE ACCORDING TO THE BARTLETT PROCEDURE. THE 12000 WORD DATA
SERIES FOR EACH PROBE IS DIVIDED INTO 11 SUBSERIES OF LENGTH 1024
WORDS. THE COMPONENT AMPLITUDE**2 SPECTRA ARE THEN AVERAGED TO
FURTHER IN GROUPS OF 3 TO OBTAIN 171 SPECTRAL ESTIMATES OVER
0 - 24 HZ.


      DIMENSION A(12000),IDEN(12),PROBE(5),X(5),Y(5),DATA(1024),
     *CFC(515),                FREQ(515),        SMCFC(174) ,SMFREQ(174)
      EQUIVALENCE                    (FREQ(1),SMFREQ(1))
      COMPLEX DATA
      DATA NN/1024/
      REWIND 10
      READ(10)NUREC,IDEN
      SCA=1024.0*1024.0
      SCB=24.0/11.0
      SCC=24.0/512.0
      READ(5,13) NOUT
   13 FORMAT(I2)
      NOREC=NUREC-NOUT
      DO 15 IN=1,NOREC
      READ(10)KR,NOPRB,LEVREC,SPLFRQ,WIND,WAVE
      DO 17 IC=1,NOPRB
      READ(10)KP,PROBE(KP),X(KP),Y(KP),MM
      WRITE (6,19) KR,PROBE(KP),X(KP),Y(KP),IDEN,MM,SPLFRQ,WAVE,WIND
   19 FORMAT (1H1,6HRECORD,I3,2H, ,A6,11H PROBE, X =,F7.3,5H, Y =,F7.3,
     11H,1X,12A6//1X,15,24H NUMBERS, SAMPLE FREQ. =,
     2       F7.2, 17H HZ, WAVE FREQ. =,F5.2, 17H HZ, WIND SPEED =,
     3 F5.2,7H M/SEC.//)
      READ(10)(A(K),K=1,12000)
      DO 21 IC=1,513
   21 CFC(IC)=0.0
      DO 23 IP=1,11
      DO 25 JL=1,1024
      JJ=JL+(IP-1)*1024
      DATA(JL)=A(JJ)
   25 CONTINUE
      CALL FFT2(DATA,NN,1,-1)
      DO 27 LL=1,513
      FC     =((CABS(DATA(LL)))**2)/SCA
      CFC(LL)=CFC(LL)+FC
   27 CONTINUE
   23 CONTINUE
      VAR=0.0
      DO 29 LT=1,513
      FREQ(LT)=FLOAT(LT-1)*SCC
      CFC(LT)=CFC(LT)*SCB
      VAR=VAR+CFC(LT)
   29 CONTINUE
      VAR=VAR/12.0
      WRITE(6,89) VAR
   89 FORMAT(1HO,10X,22HTHE RECORD VARIANCE = ,F10.5)
      DO 49 I=1,100
      WRITE(6,77) FREQ(I),CFC(I)
   77 FORMAT(5X,F10.5,5X,F10.5)
   49 CONTINUE
      DO 47 NR=1,171
      LI=2+3*(NR-1)
      LIM1=LI-1
      LIP1=LI+1
      SMCFC(NR)=(CFC(LIM1)+CFC(LI)+CFC(LIP1))/3.0
      SMCFC(NR)=ALOG10(SMCFC(NR))
   47 CONTINUE
      DO 67 NP=1,171
      LM=2+3*(NP-1)
      SMFREQ(NP)=(FLOAT(LM))*SCC
   67 CONTINUE
      CALL AXEMT(6.0,8.0,4,4)
      CALL LABELX(14,14HFREQUENCY (HZ))
      CALL LABELY(45,45HMEAN SQUARED SURFACE DISPLACEMENT IN CM**2/HZ)
      CALL TITLE(46,46HSMOOTHED SPECTRUM FOR        PROBE OF RECORD   )
      CALL RANGLE(0.0,24.0,-5.0,2.0)
      CALL PLTNEW(SMFREQ,SMCFC,171,31)
   17 CONTINUE
   15 CONTINUE
      REWIND 10
       STOP
      END
```

Reproduced with permission of the copyright owner. Further reproduction prohibited without permission.

REFERENCES

Barger, W.R., Garrett, W.D., Mollo-Christensen,E.L. Ruggles, K.W., 1970: Effects of an artificial sea slick upon the atmosphere and the ocean. J. Appl. Meteorology. 9, 396-400.

Barnett, T.P. and Wilkerson, J.C., 1967: On the generation of ocean wind-waves as inferred from airborne radar measurements of fetch limited spectra. J. Mar. Research, 25, 292-321.

Courant, R., 1961: Differential and Integral Calculus. Vol II. Blackie & Son Ltd, London.

Cox, C.S., 1958: Measurements of slopes of high frequency wind waves. J. Mar. Research. 16, 3, 199-225.

Crapper, G.D., 1957: An exact solution for progressive capillary waves of arbitrary amplitude. J. Fluid Mech. 2, 532-540.

Crapper, G.D., 1970: Non-linear capillary waves generated by steep gravity waves. J. Fluid Mech. 40, 1, 149-159.

Davis, R.E., 1970: On the turbulent flow over a wavy boundary. J. Fluid Mech. 42, 4, 721-732.

Flower, R.J., 1973(a): Water wave sensing devices. Tech. Rept. (in preparation), Chesapeake Bay Inst., The Johns Hopkins University.

Hasselmann, K., 1971: On the mass and momentum transfer between short gravity waves and larger-scale motions. J. Fluid Mech. 50, 1, 189-205.

Hires, R.I., 1968: An experimental study of wind-wave interactions. Tech. Rept. No. 37, Chesapeake Bay Inst., The Johns Hopkins University. 169 pp.

Reproduced with permission of the copyright owner. Further reproduction prohibited without permission.

REFERENCES (continued)

Jenkins, G.M. and Watts, D.G., 1968: Spectral analysis and its applications. Holden-Day, San Francisco.

Kennedy, D.A., 1965: Some measurements of the dispersion of spheres in a turbulent flow. Ph.D. Thesis, The Johns Hopkins Univ. 88 pp.

Kinsman, Blair, 1965: Wind waves - their generation and propagation on the ocean surface. Prentice-Hall, N.J.

Laufer, J., 1951: Investigation of turbulent flow in a two-dimensional channel. Rept. 1053, N.A.C.A. 20 pp.

Longuet-Higgins, M.S., 1963: The generation of capillary waves by steep gravity waves. J. Fluid Mech. 16, 1, 138-159.

Longuet-Higgins, M.S., 1969(a): Action of a variable stress at the surface of water waves. Physics of Fluids, 12, 4, 737-740.

Longuet-Higgins, M.S., 1969(b): A nonlinear mechanism for the generation of sea waves. Proc. Roy. Soc. A. 311, 371-389.

Longuet-Higgins, M.S. and Stewart, R.W., 1960: Changes in the form of short gravity waves on long waves and tidal currents. J. Fluid Mech. 8, 565-583.

Longuet-Higgins, M.S. and Stewart, R.W., 1964: Radiation stresses in water waves; a physical discussion with applications. Deep Sea Research. 11, 529-562.

McGoldrick, L.F., 1972: On the rippling of small waves: a harmonic nonlinear nearly resonant interaction. J. Fluid Mech. 52, 4 725-751.

Michell, J., 1893: The highest waves in water. Phil. Mag. xxxvi, 430.

Reproduced with permission of the copyright owner. Further reproduction prohibited without permission.

REFERENCES (continued)

Miles, J.W., 1957: On the generation of surface waves by shear flows. J. Fluid Mech. 3, 2, 185-204.

Miles, J.W., 1959(a): On the generation of surface waves by shear flows Part 2. J. Fluid Mech. 6, 4, 568-582.

Miles, J.W., 1962(b): On the generation of surface waves by shear flows, Part 4. J. Fluid Mech. 13, 3, 433-448.

Mitsuyasu, H., 1966: Interactions between water waves and winds (I). Report of the Research Institute for Applied Mechanics. Vol. XIV, No. 48, 67-88.

O'Brien, E., 1967: On the flux of heat through laminar wavy liquid layers. J. Fluid Mech. 28, 2, 295-303.

Phillips, O.M., 1957: On the generation of wind by turbulent wind. J. Fluid Mech. 2, 5, 417-445.

Phillips, O.M., 1966: The dynamics of the upper ocean. Cambridge Univ. Press. 261 pp.

Schooley, A.H., 1958: Profiles of wind-created water waves in the capillary-gravity transition region. J. Mar. Research. 16, 2, 100-108.

Schwarz, W.H., 1957: Some effects of isotropic turbulence on a pendulum at moderate Reynolds number. Doc. of Engr. Thesis, The Johns Hopkins Univ. 105 pp.

Van Dyke, Milton, 1964: Perturbation methods in fluid mechanics. Academic Press, N.Y.

Whitham, G.B., 1970: Two-timing, variational principles and waves. J. Fluid Mech. 44, 2, 373-395.

Reproduced with permission of the copyright owner. Further reproduction prohibited without permission.

REFERENCES (continued)

Wilson, W.S., 1972: An experimental study of the growth of mechanically generated surface water waves when subjected to a fully developed turbulent flow. Tech. Rept. No.74, Chesapeake Bay Inst., The Johns Hopkins Univ. 85 pp.

Wu, J., 1968: Laboratory studies of wind-wave interactions. J. Fluid Mech. 34, 1, 91-111.

Reproduced with permission of the copyright owner. Further reproduction prohibited without permission.

Reproduced with permission of the copyright owner. Further reproduction prohibited without permission.

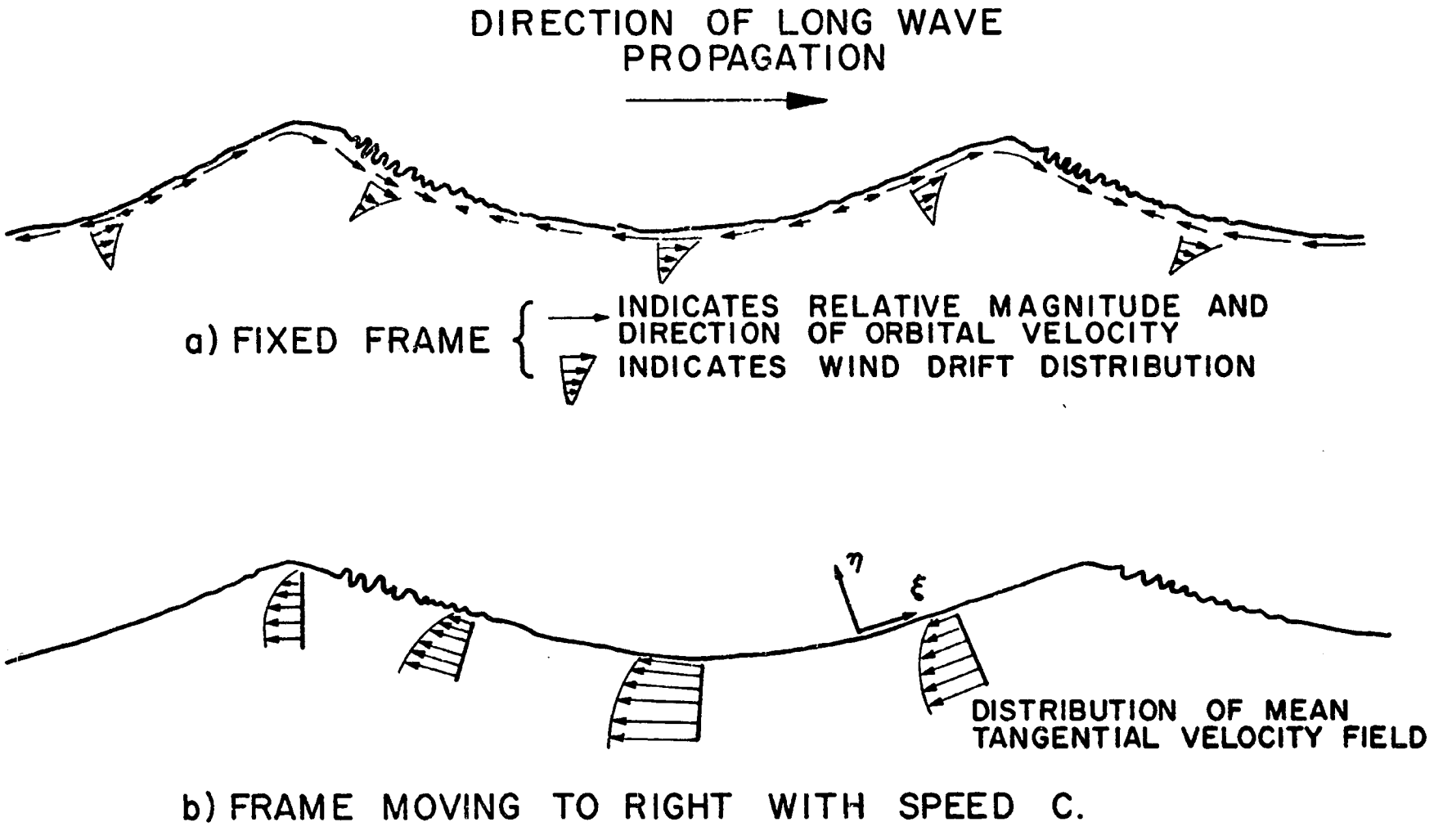

Fig. (1) Model of ripple structure in rest and moving frames.

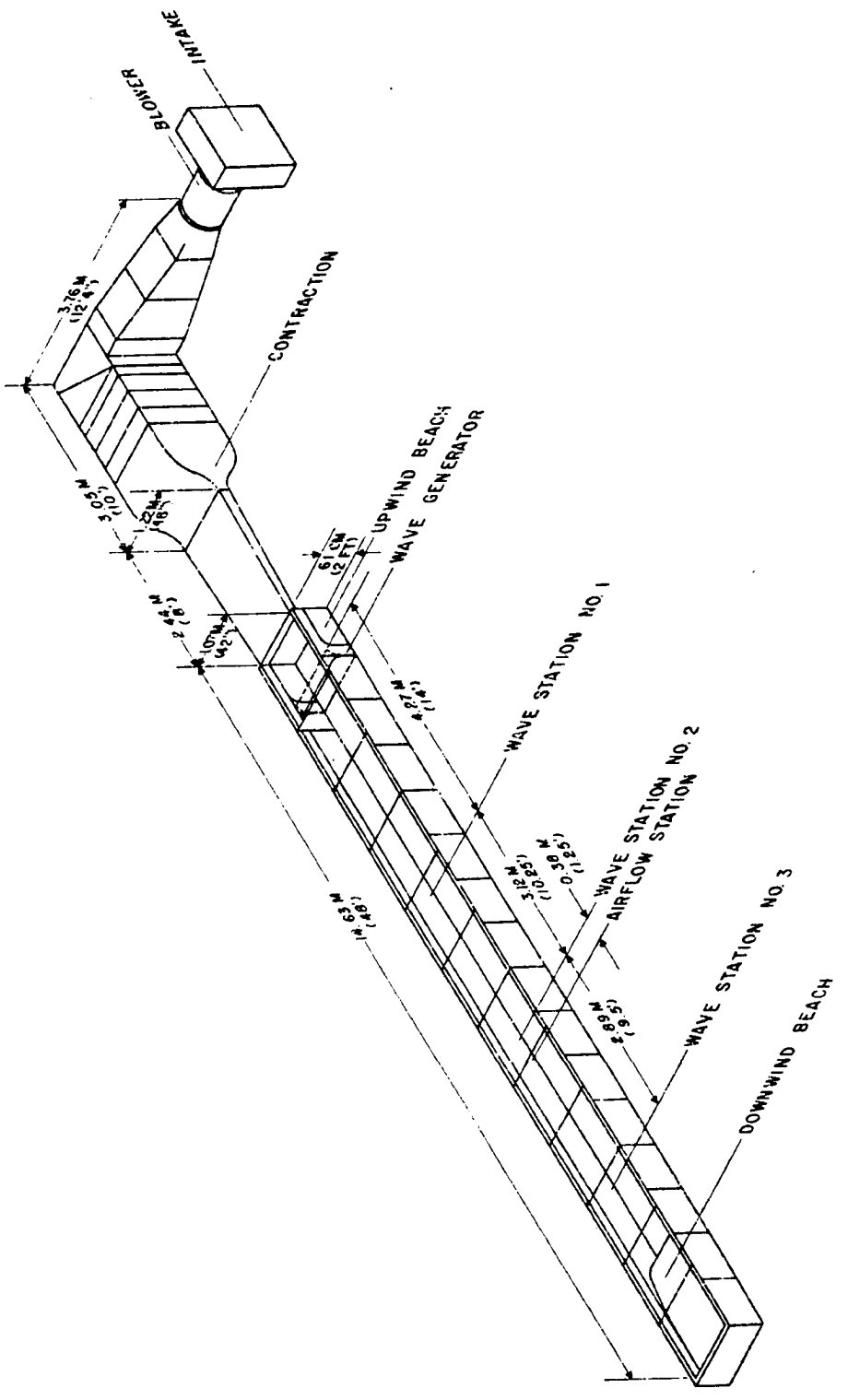

Fig. (2) Wind-wave facility.

Reproduced with permission of the copyright owner. Further reproduction prohibited without permission.

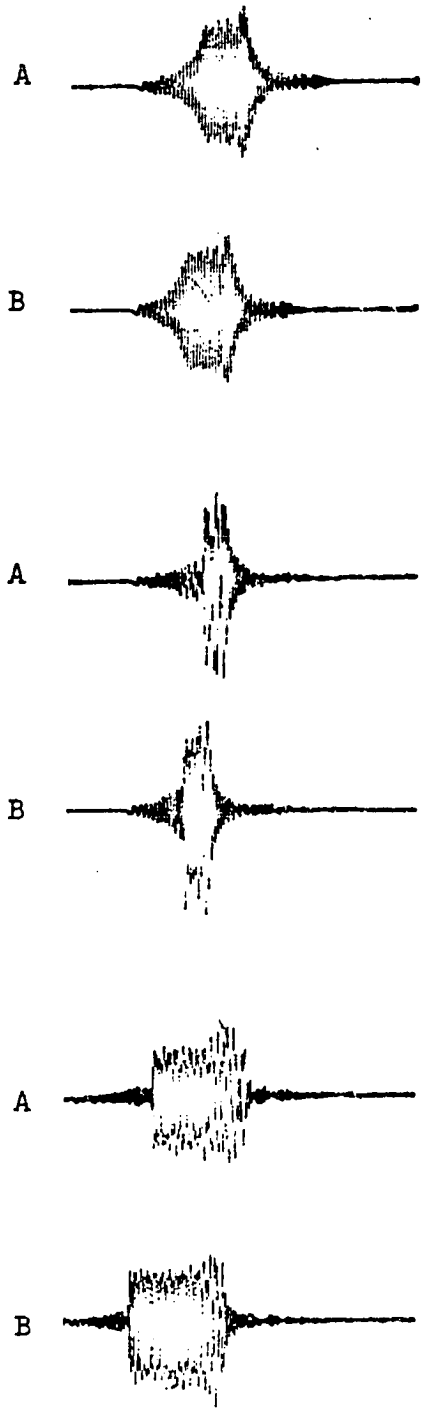

Fig. (3) Absorption of wave groups as detected by wave probes ~ 2 m and ~4 m upstream of beach (probe corresponding to trace A of each pair is closer to beach.)

Reproduced with permission of the copyright owner. Further reproduction prohibited without permission.

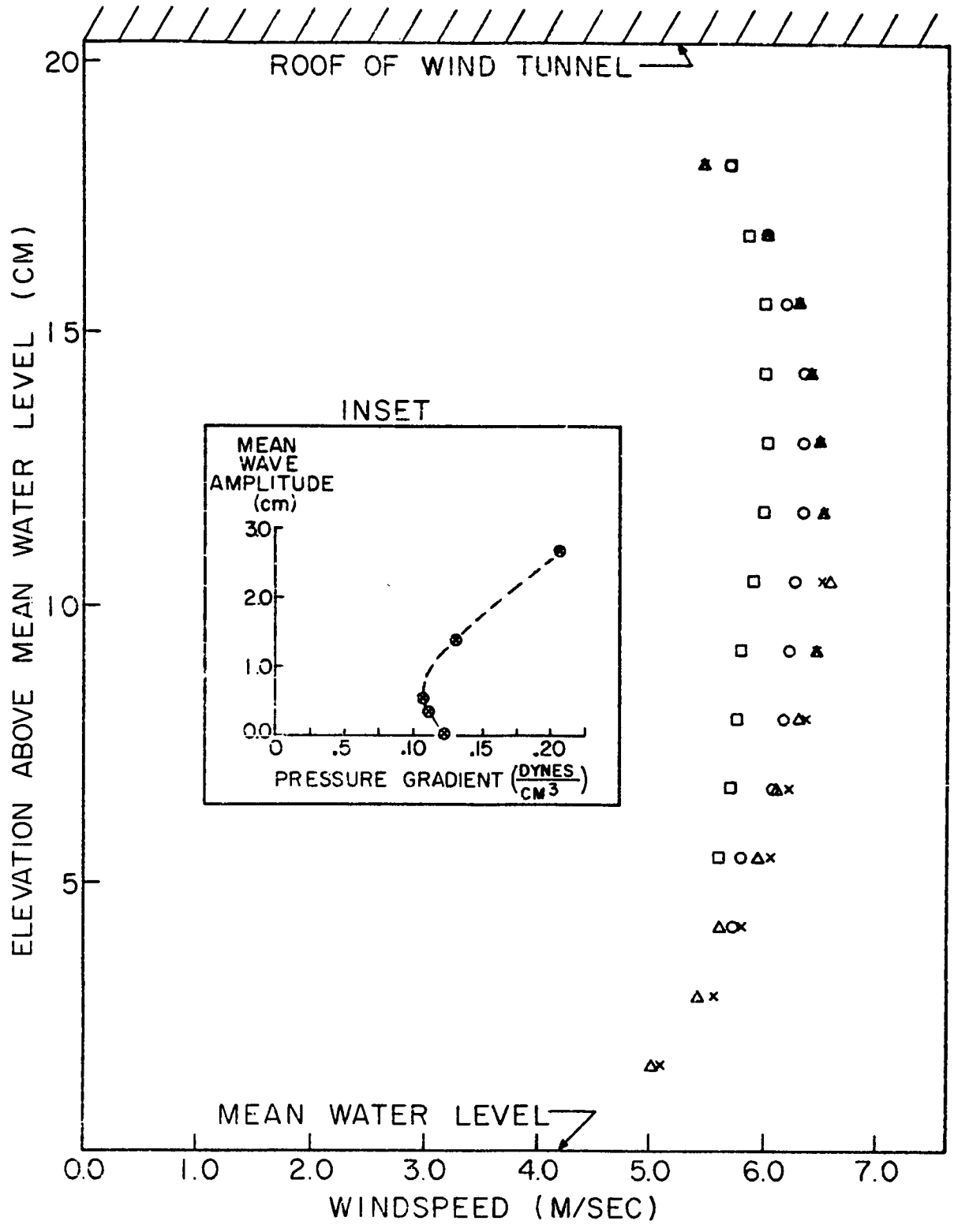

Fig. (4) Variation of vertical mean wind velocity profiles and streamwise pressure gradient as a function of wave amplitude.

Reproduced with permission of the copyright owner. Further reproduction prohibited without permission.

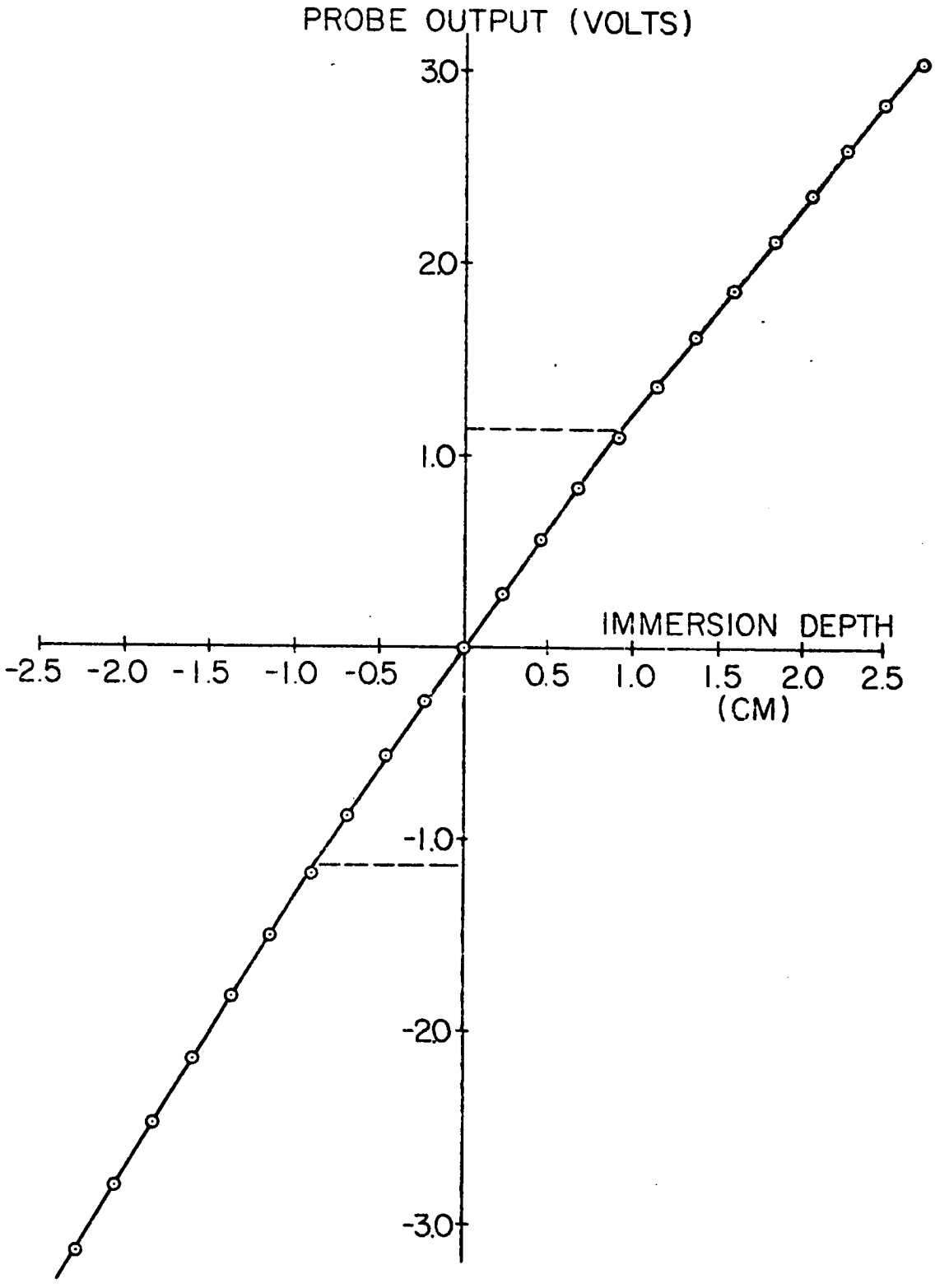

Fig. (5) Wave probe calibration curve.

Reproduced with permission of the copyright owner. Further reproduction prohibited without permission.

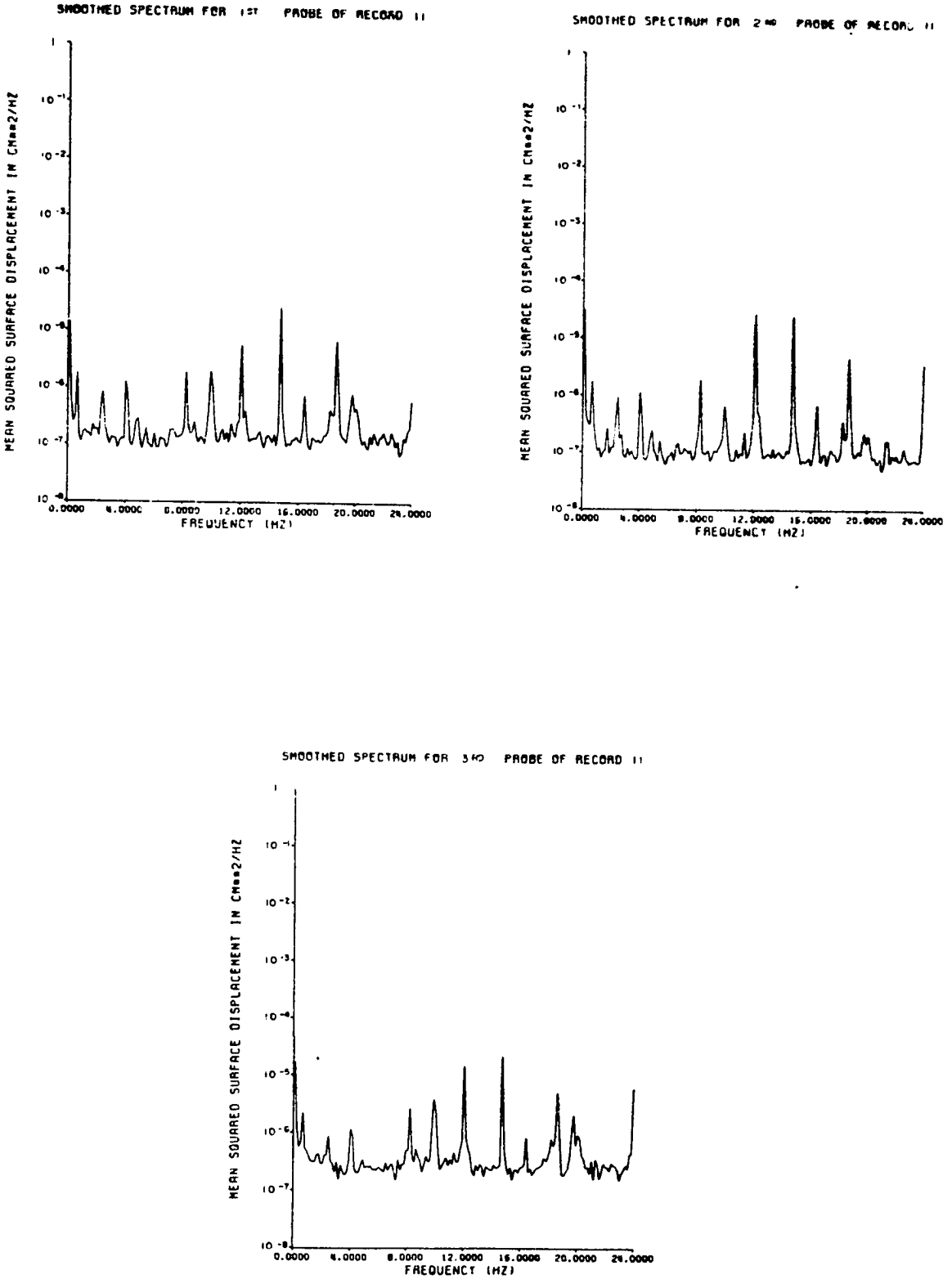

Fig. (6) Noise (electronic and computational) spectra.

Reproduced with permission of the copyright owner. Further reproduction prohibited without permission.

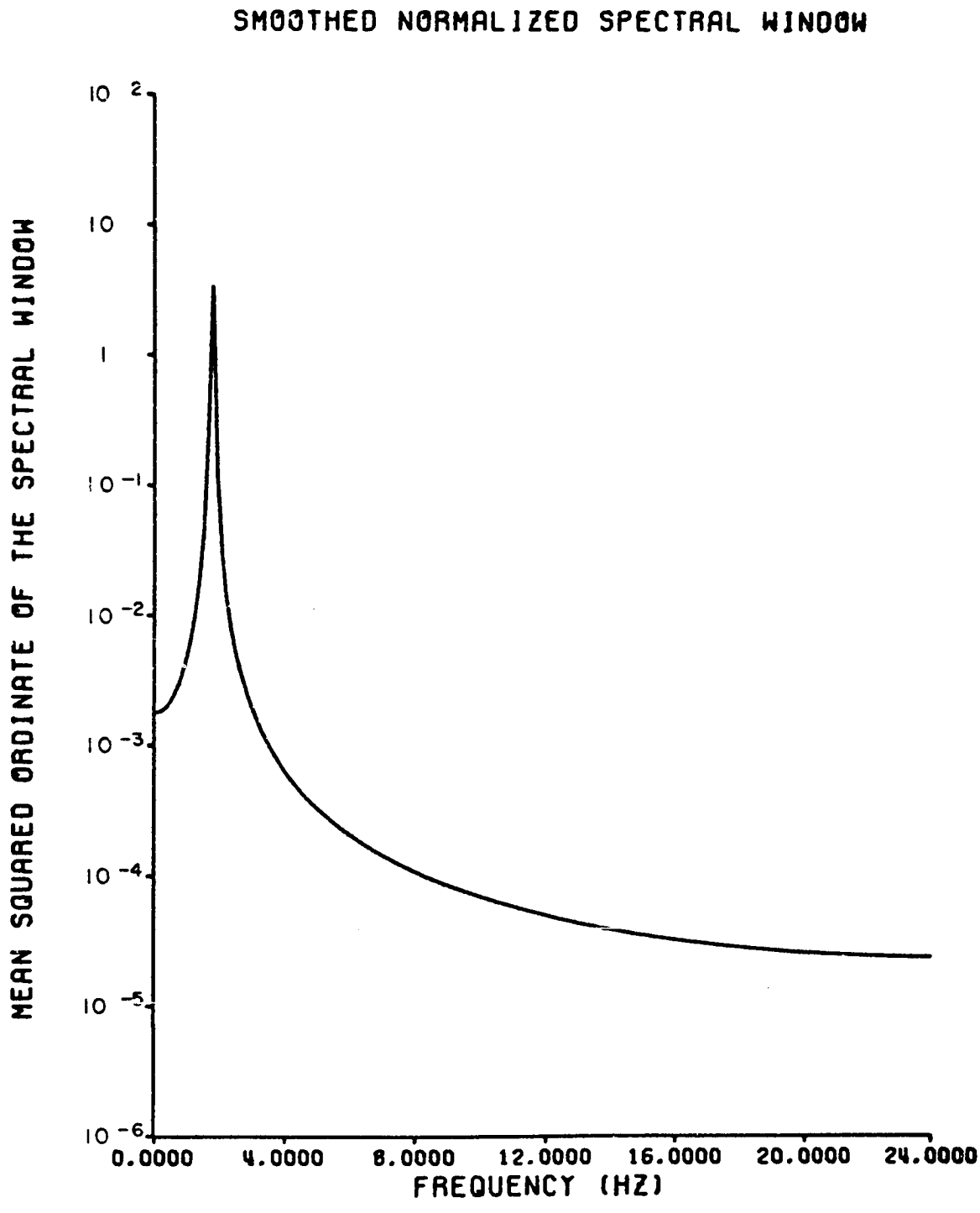

Fig. (7) Normalized spectral window shape.

Reproduced with permission of the copyright owner. Further reproduction prohibited without permission.

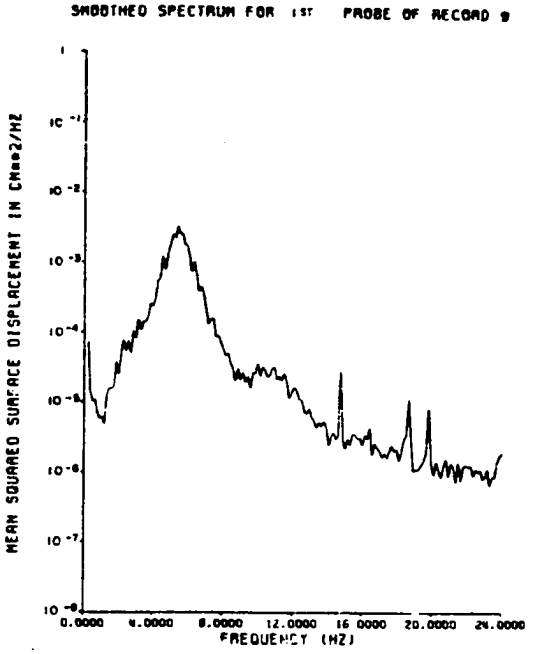

Fig.(8) Spectrum for purely wind-driven situation at first fetch (4.27 m).

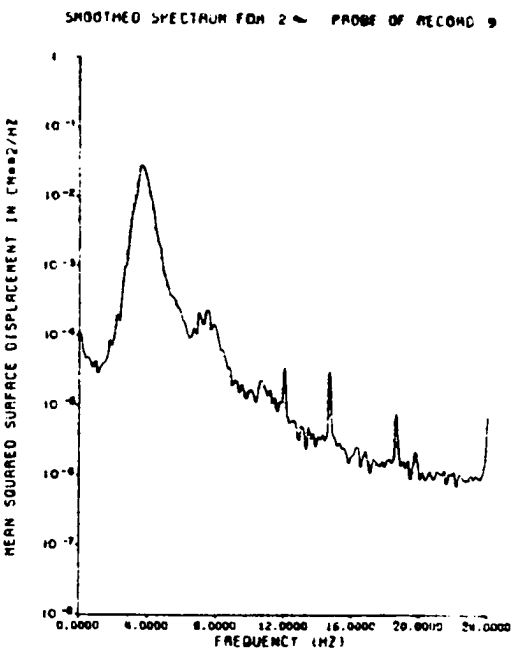

Fig.(9) Spectrum for purely wind-driven situation at the second fetch (7.32 m).

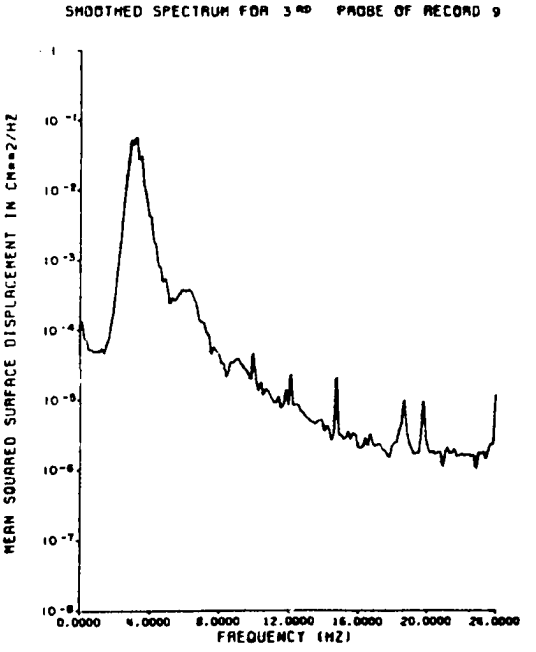

Fig.(10) Spectrum for purely wind-driven situation at the third fetch (10.36 m).

Reproduced with permission of the copyright owner. Further reproduction prohibited without permission.

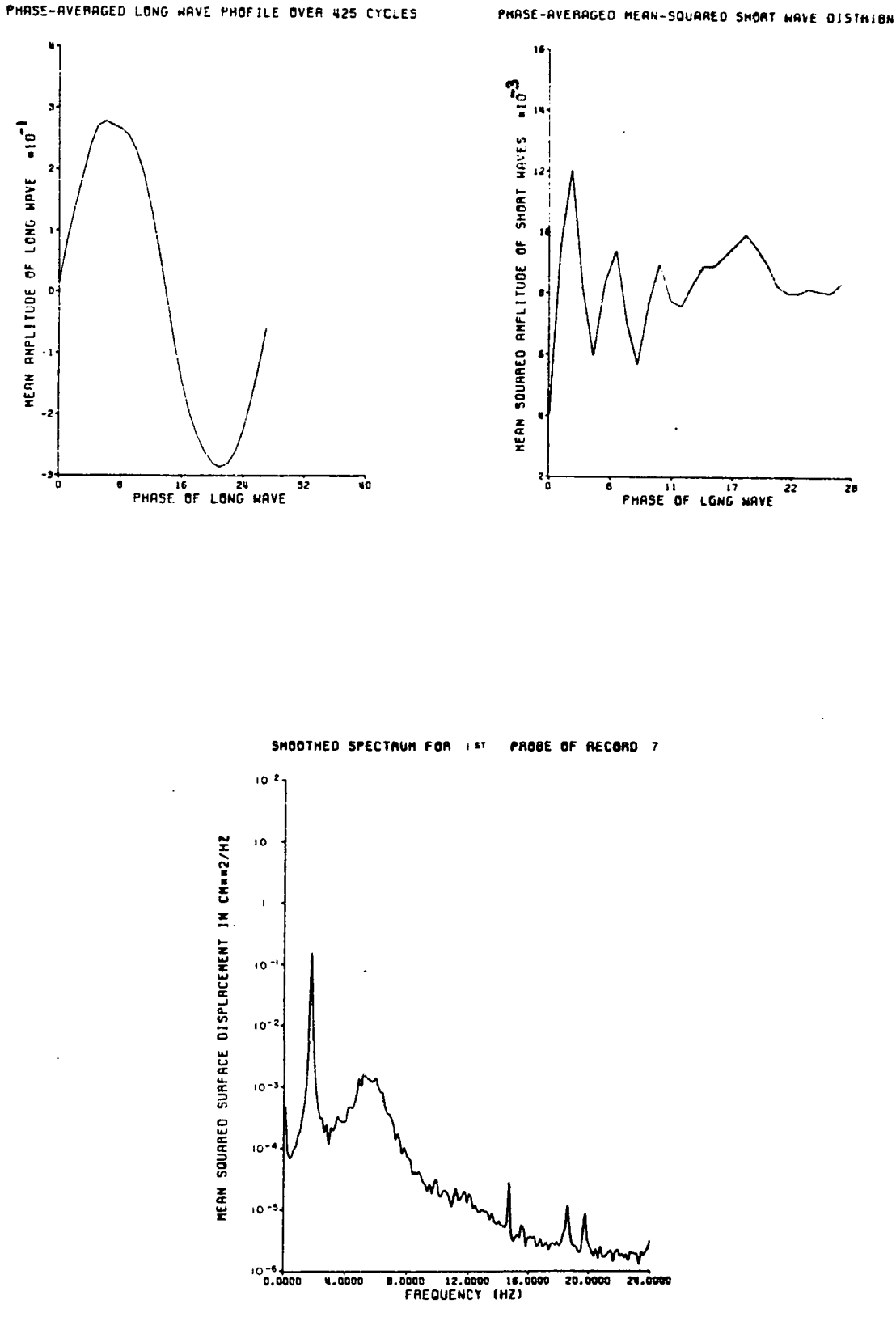

Fig. (11) Spectrum and phase-averaged distributions for the case of superposed 1.7 Hz mechanically-generated waves with slope $\sim$ 0.03 at the first fetch (4.27 m).

Reproduced with permission of the copyright owner. Further reproduction prohibited without permission.

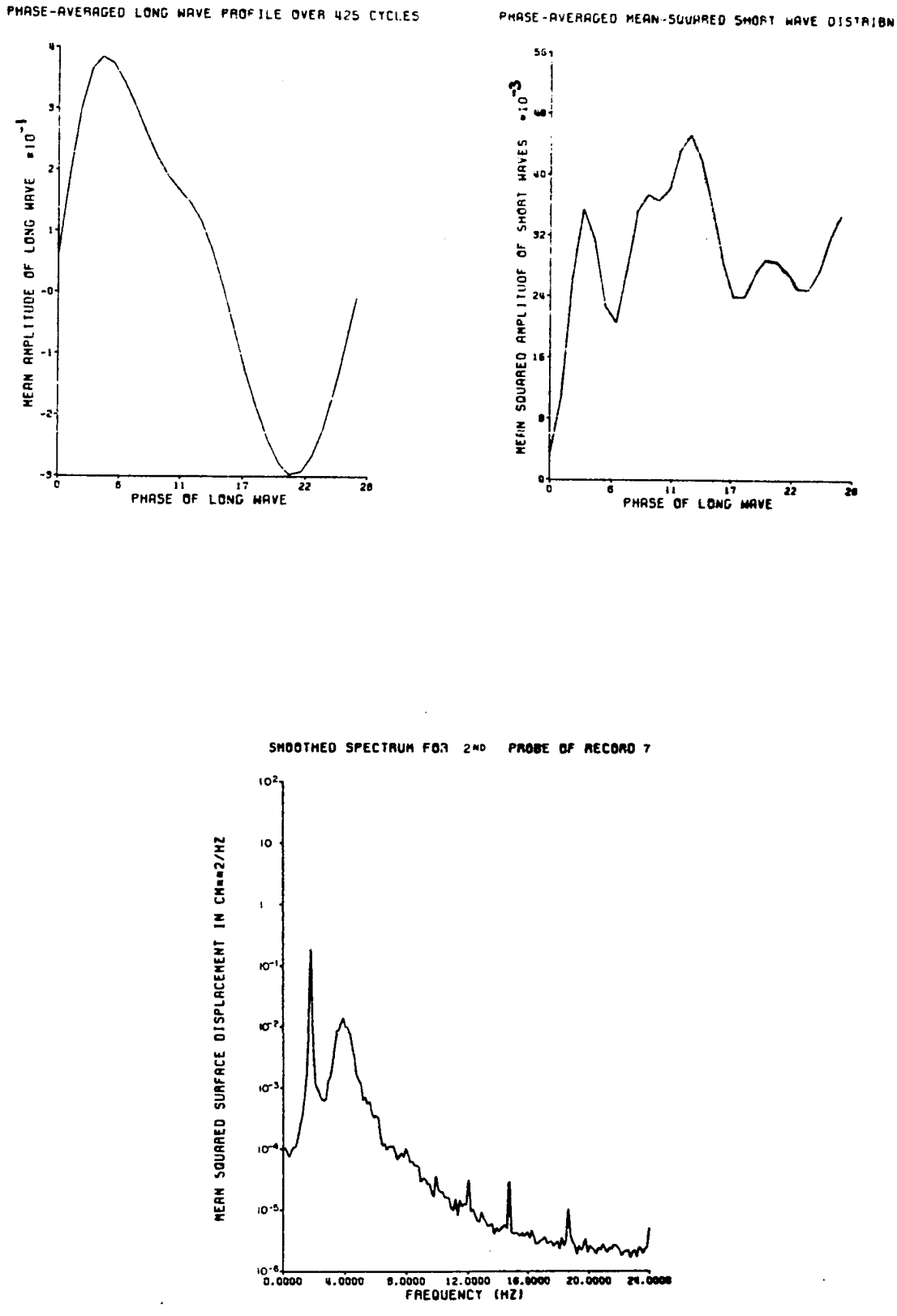

Fig. (12) Spectrum and phase-averaged distributions for the case of superposed 1.7 Hz mechanically-generated waves with slope $\sim$ 0.03 at the second fetch (7.32 m).

Reproduced with permission of the copyright owner. Further reproduction prohibited without permission.

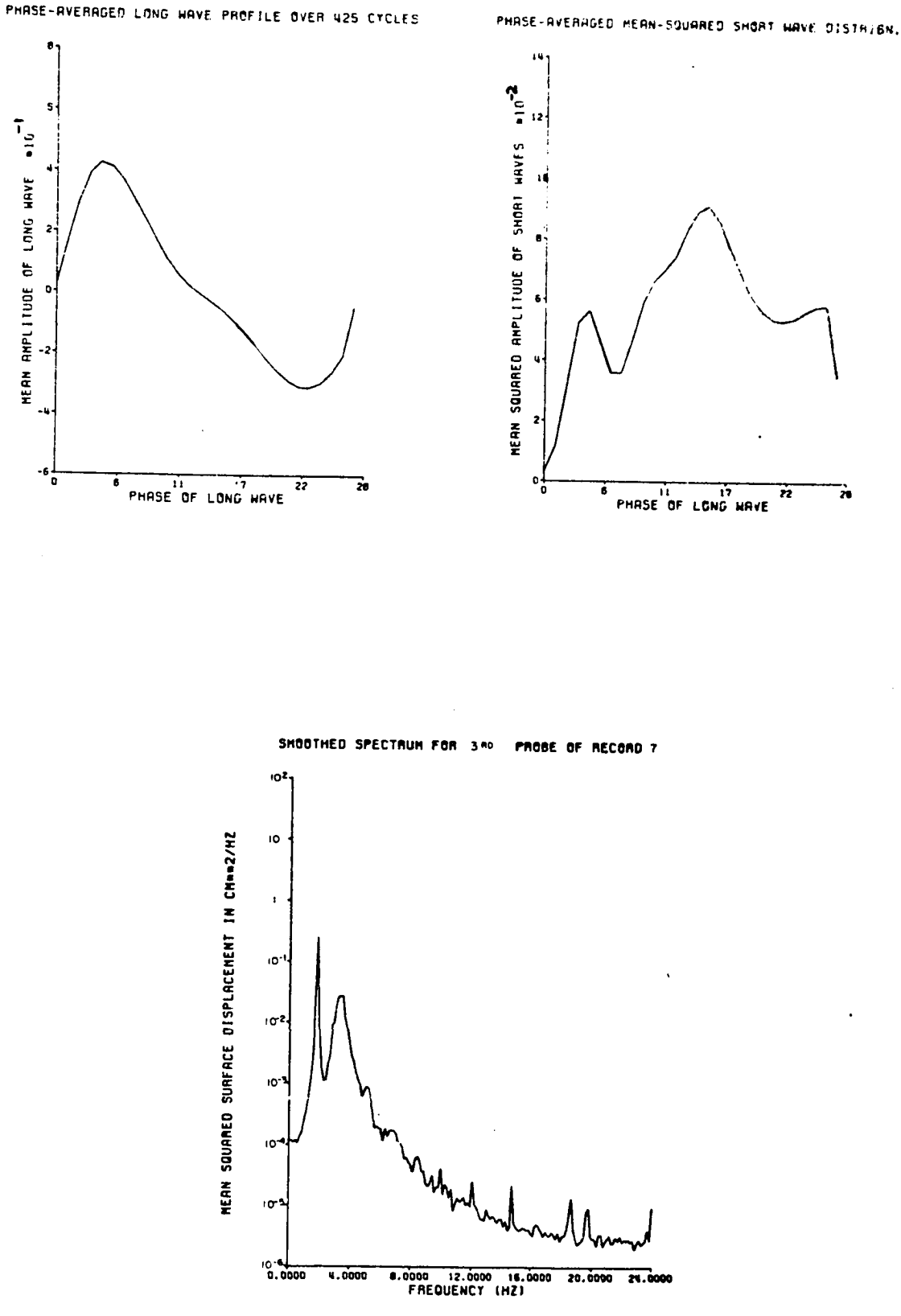

Fig. (13) Spectrum and phase-averaged distributions for the case of superposed 1.7 Hz mechanically-generated waves with slope ~ 0.03 at the third fetch (10.36 m).

Reproduced with permission of the copyright owner. Further reproduction prohibited without permission.

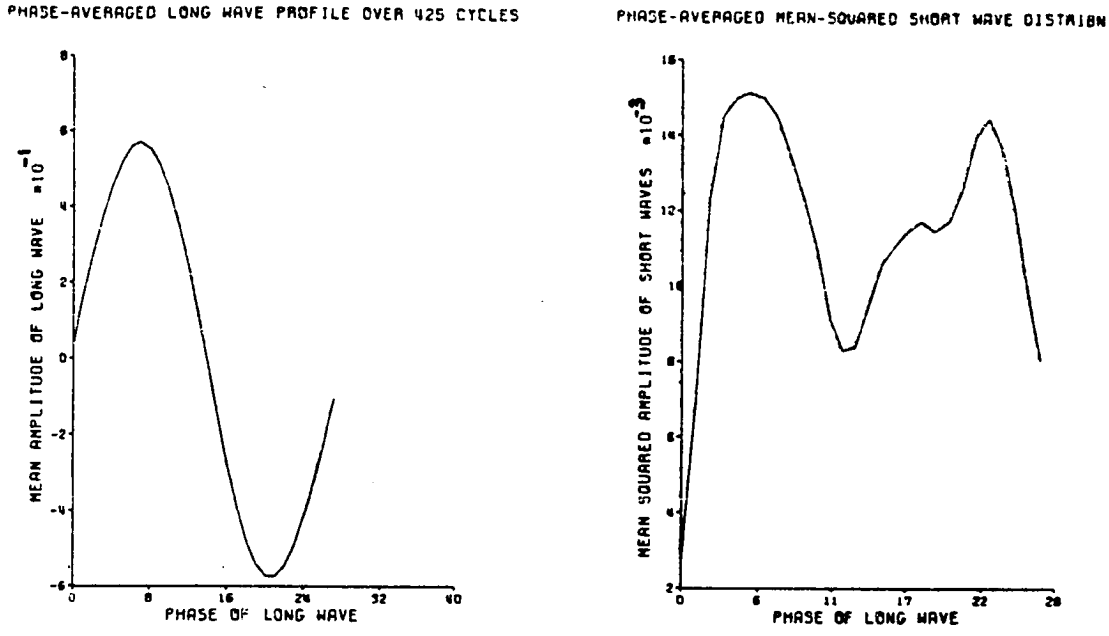

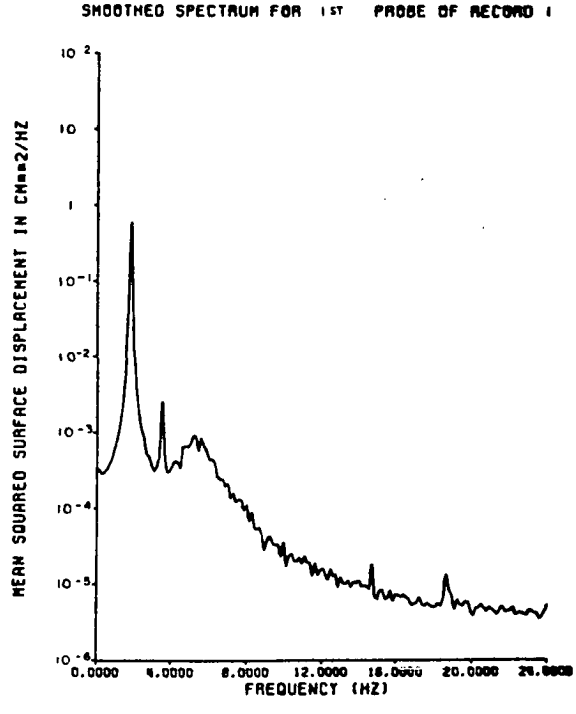

Fig. (14) Spectrum and phase-averaged distributions for the case of superposed 1.7 Hz mechanically-generated waves with slope $\sim$ 0.06 at the first fetch (4.27 m).

Reproduced with permission of the copyright owner. Further reproduction prohibited without permission.

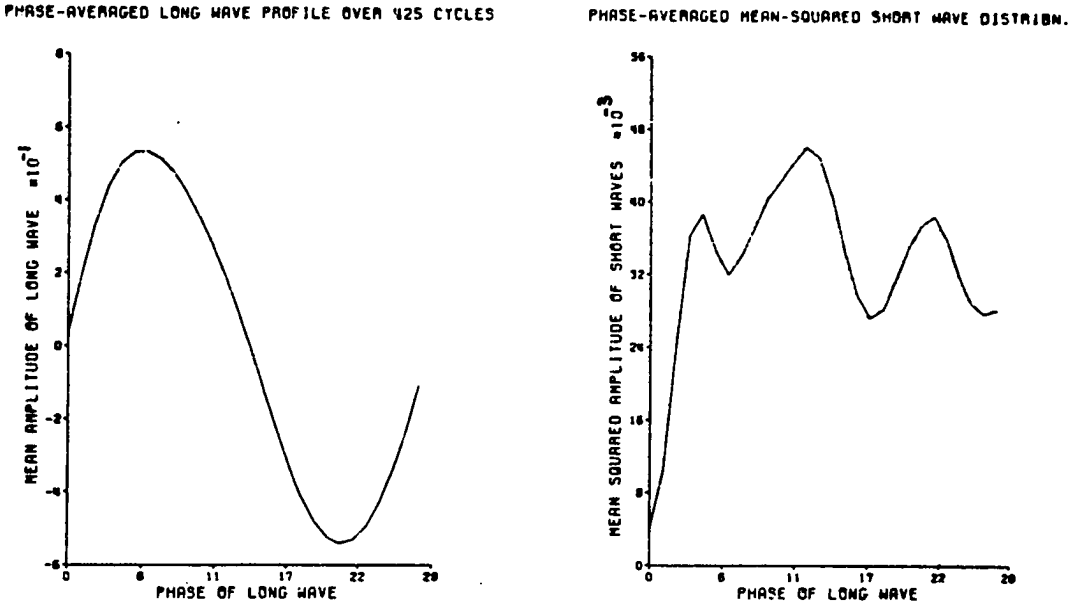

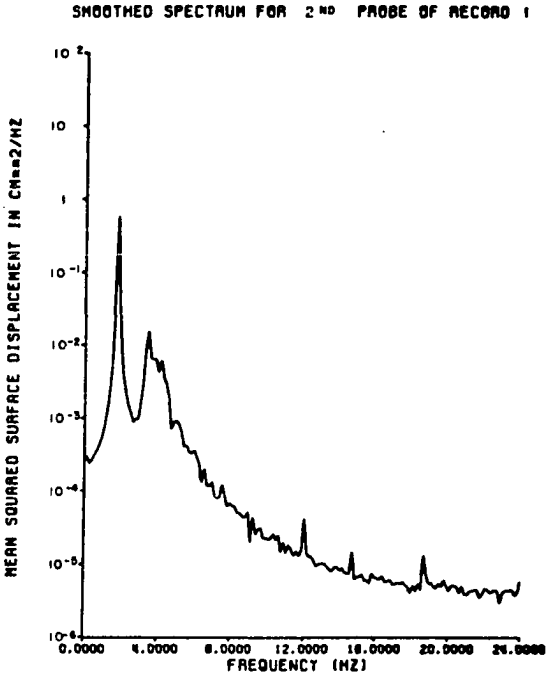

Fig. (15) Spectrum and phase-averaged distributions for the case of superposed 1.7 Hz mechanically-generated waves with slope ~ 0.06 at the second fetch (7.32 m).

Reproduced with permission of the copyright owner. Further reproduction prohibited without permission.

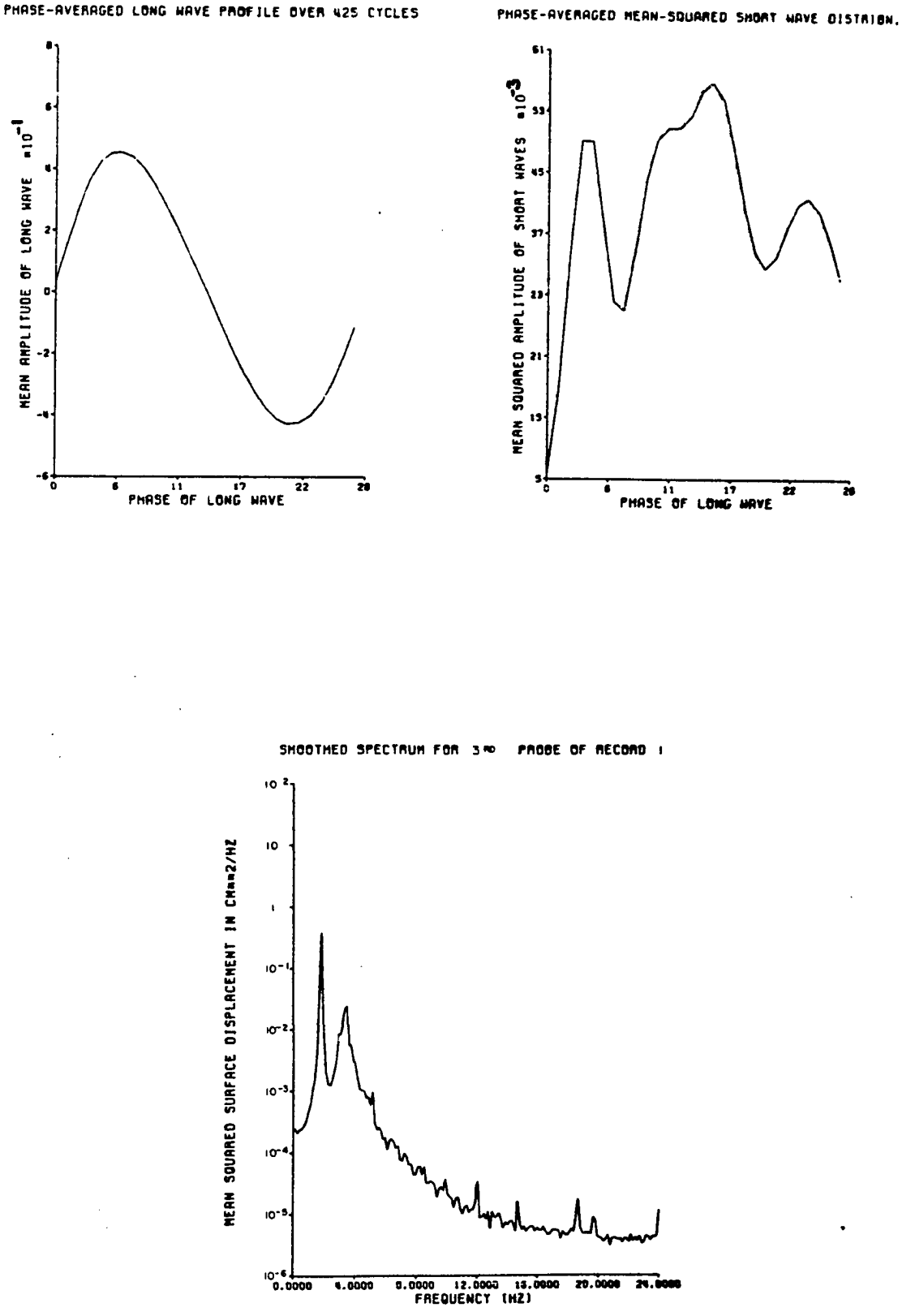

Fig. (16) Spectrum and phase-averaged distributions for the case of superposed 1.7 Hz mechanically-generated waves with slope $\sim$ 0.06 at the third fetch (10.36 m).

Reproduced with permission of the copyright owner. Further reproduction prohibited without permission.

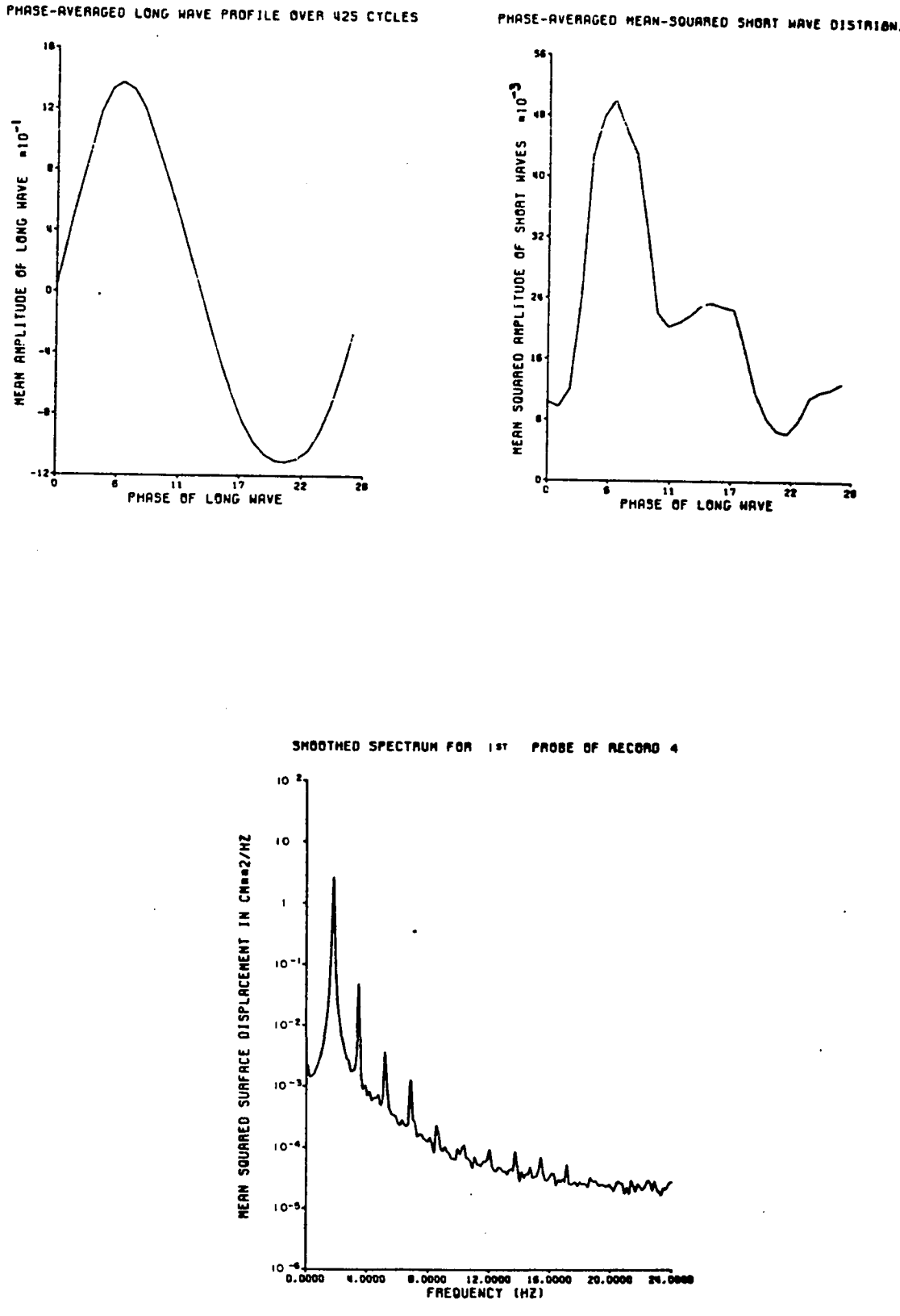

Fig. (17) Spectrum and phase-averaged distributions for the case of superposed 1.7 Hz mechanically-generated waves with slope $\sim$ 0.175 at the first fetch (4.27 m).

Reproduced with permission of the copyright owner. Further reproduction prohibited without permission.

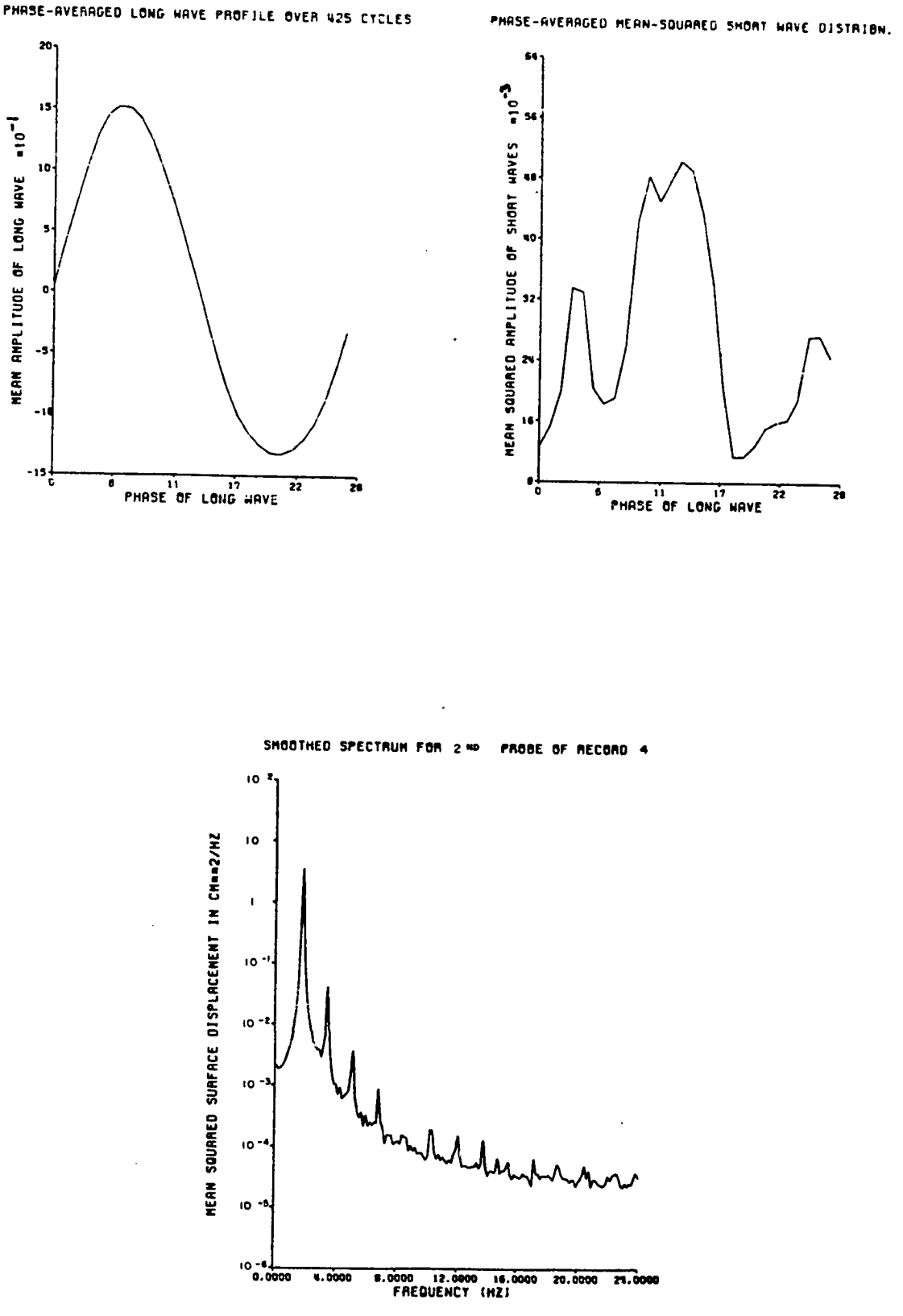

Fig. (18) Spectrum and phase-averaged distributions for the case of superposed 1.7 Hz mechanically-generated waves with slope$\sim$ 0.175 at the second fetch (7.32 m).

Reproduced with permission of the copyright owner. Further reproduction prohibited without permission.

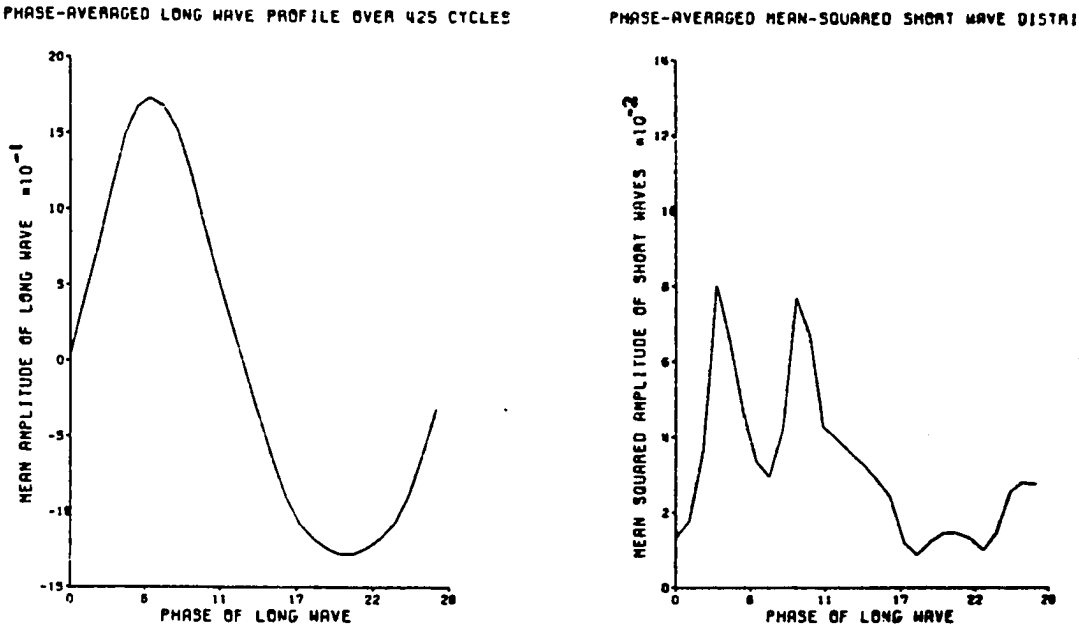

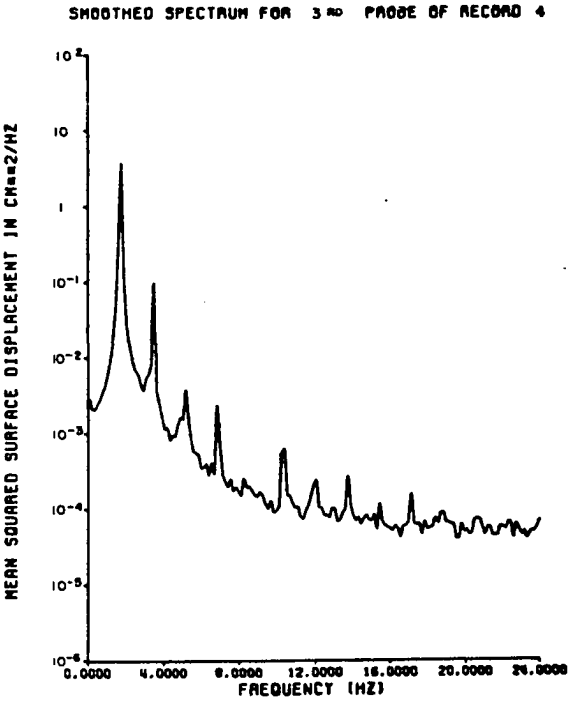

Fig. (19) Spectrum and phase-averaged distributions for the case of superposed 1.7 Hz mechanically-generated waves with slope $\sim$0.175 at the third fetch (10.36 m).

Reproduced with permission of the copyright owner. Further reproduction prohibited without permission.

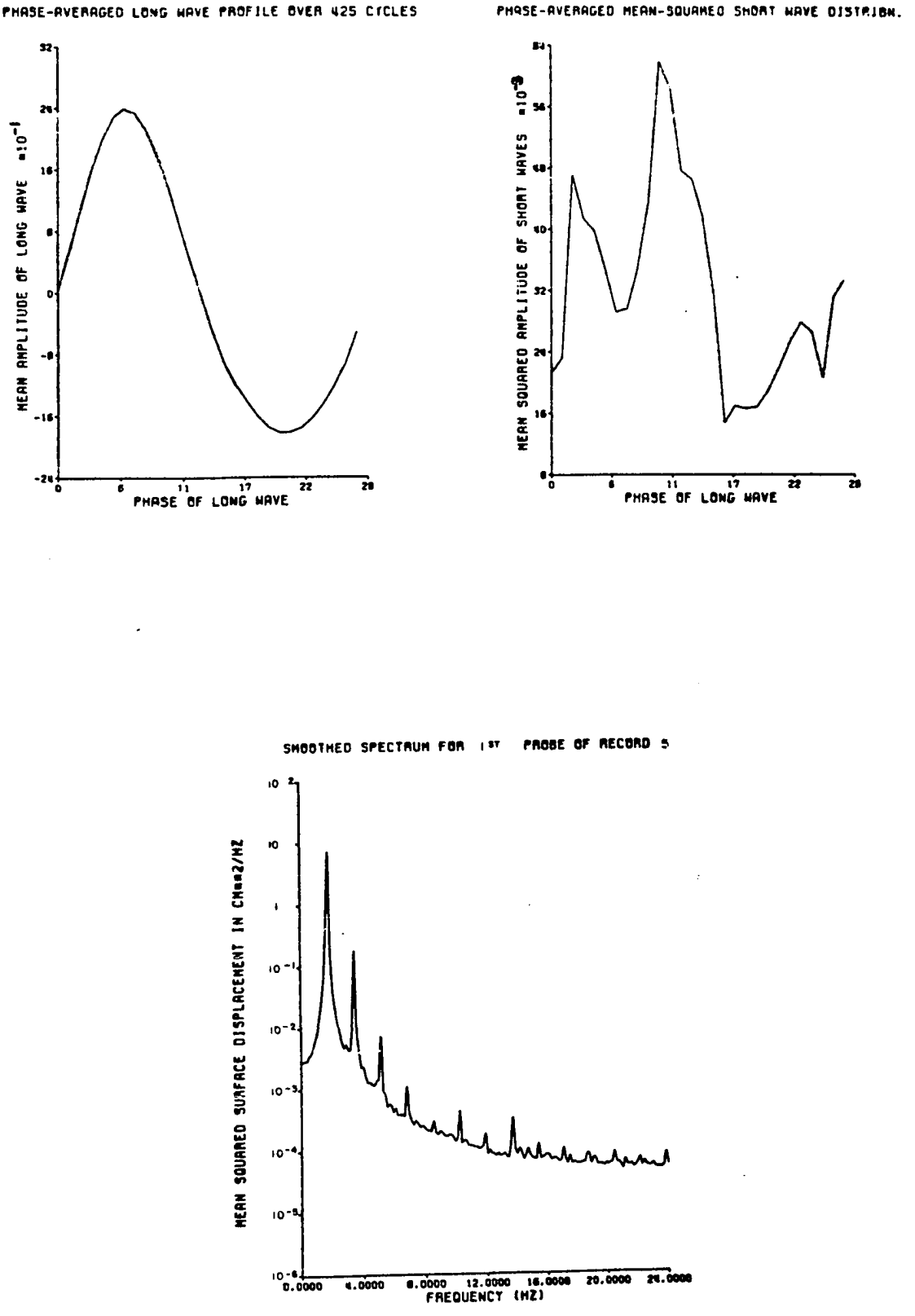

Fig. (20) Spectrum and phase-averaged distributions for the case of superposed 1.7 Hz mechanically-generated waves with slope $\sim$0.29 at the first fetch (4.27 m).

Reproduced with permission of the copyright owner. Further reproduction prohibited without permission.

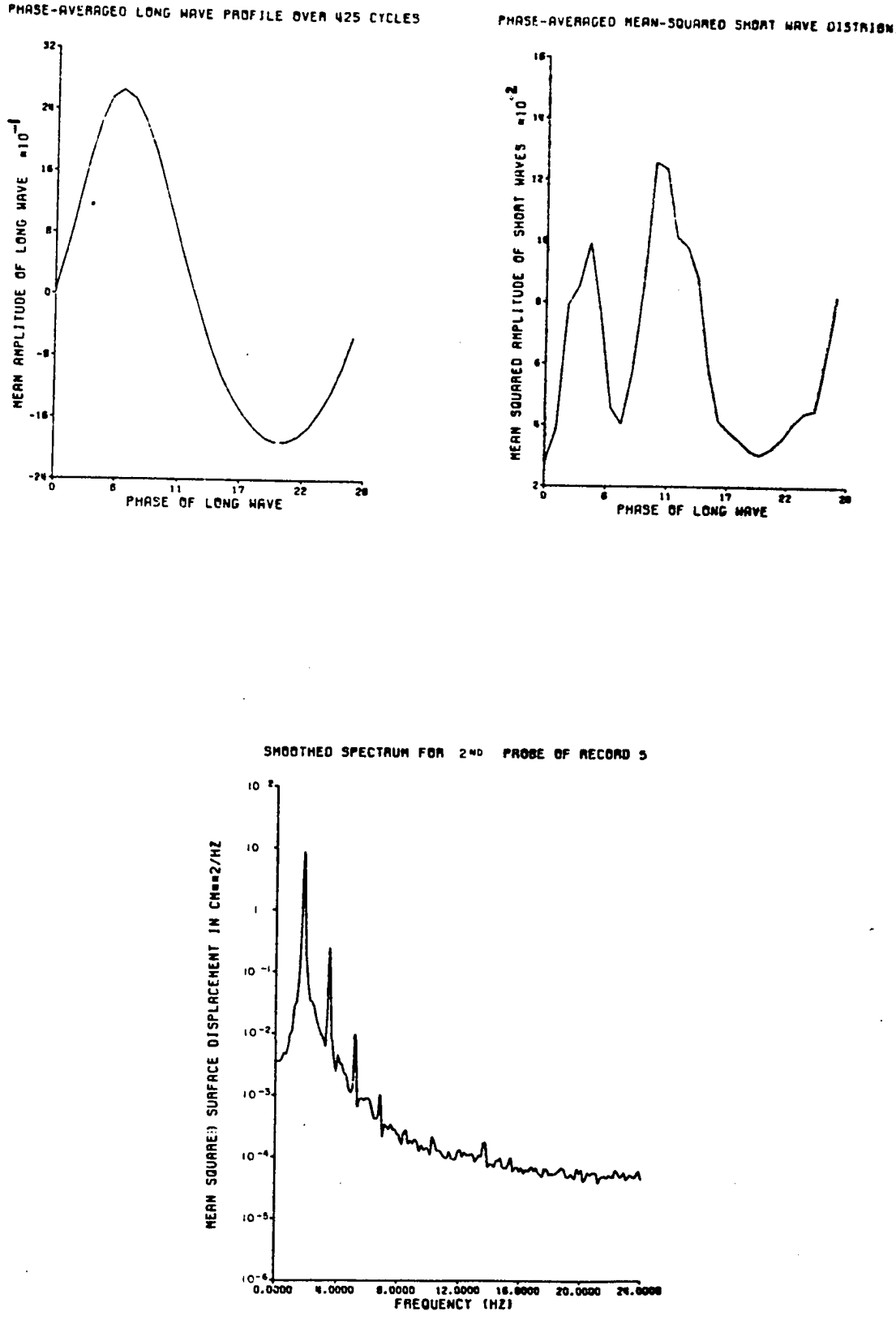

Fig. (21) Spectrum and phase-averaged distributions for the case of superposed 1.7 Hz mechanically-generated waves with slope $\sim$ 0.29 at the second fetch (7.32 m).

Reproduced with permission of the copyright owner. Further reproduction prohibited without permission.

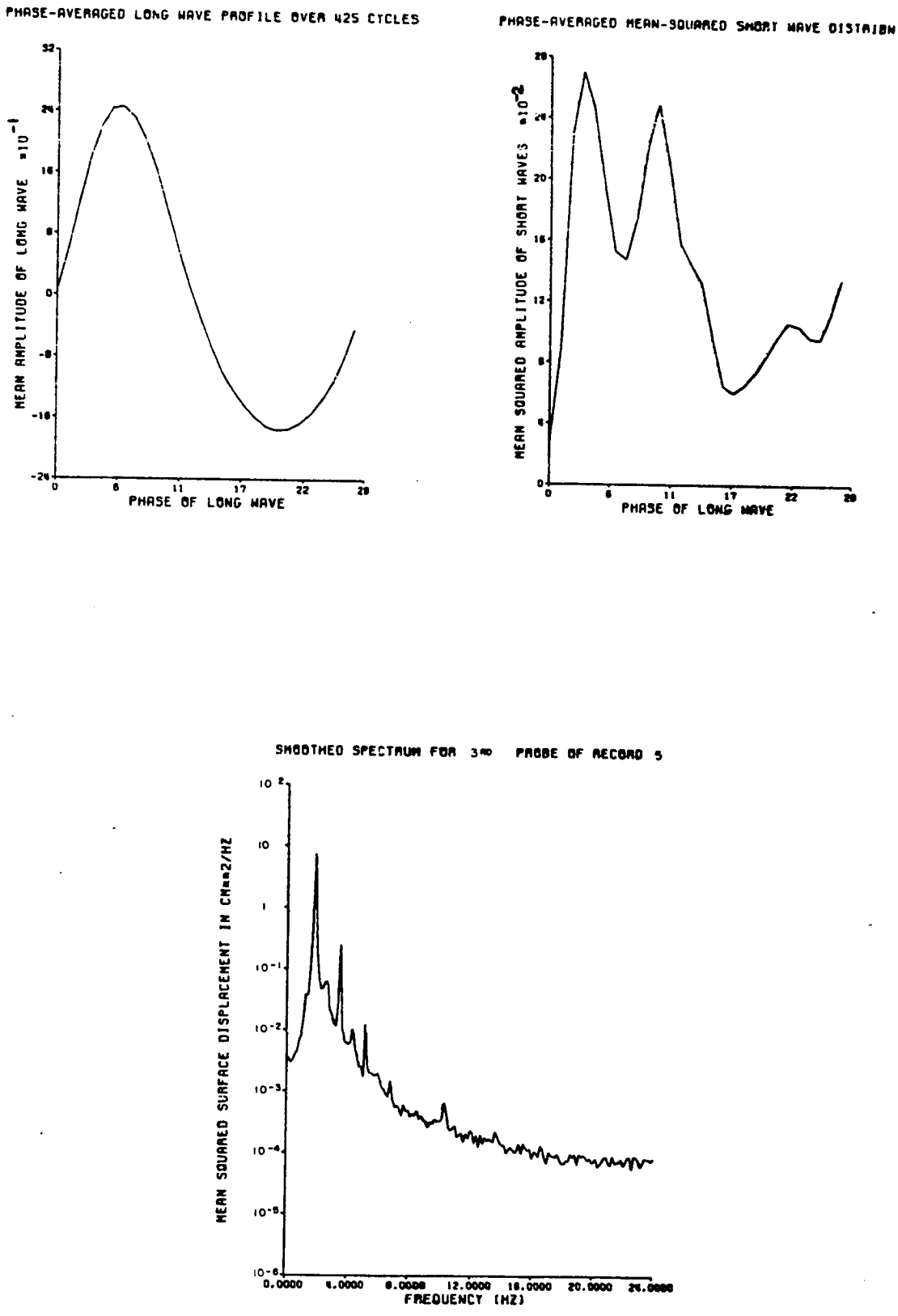

Fig. (22) Spectrum and phase-averaged distributions for the case of superposed 1.7 Hz mechanically-generated waves with slope $\sim$ 0.29 at the third fetch (10.36 m).

Reproduced with permission of the copyright owner. Further reproduction prohibited without permission.

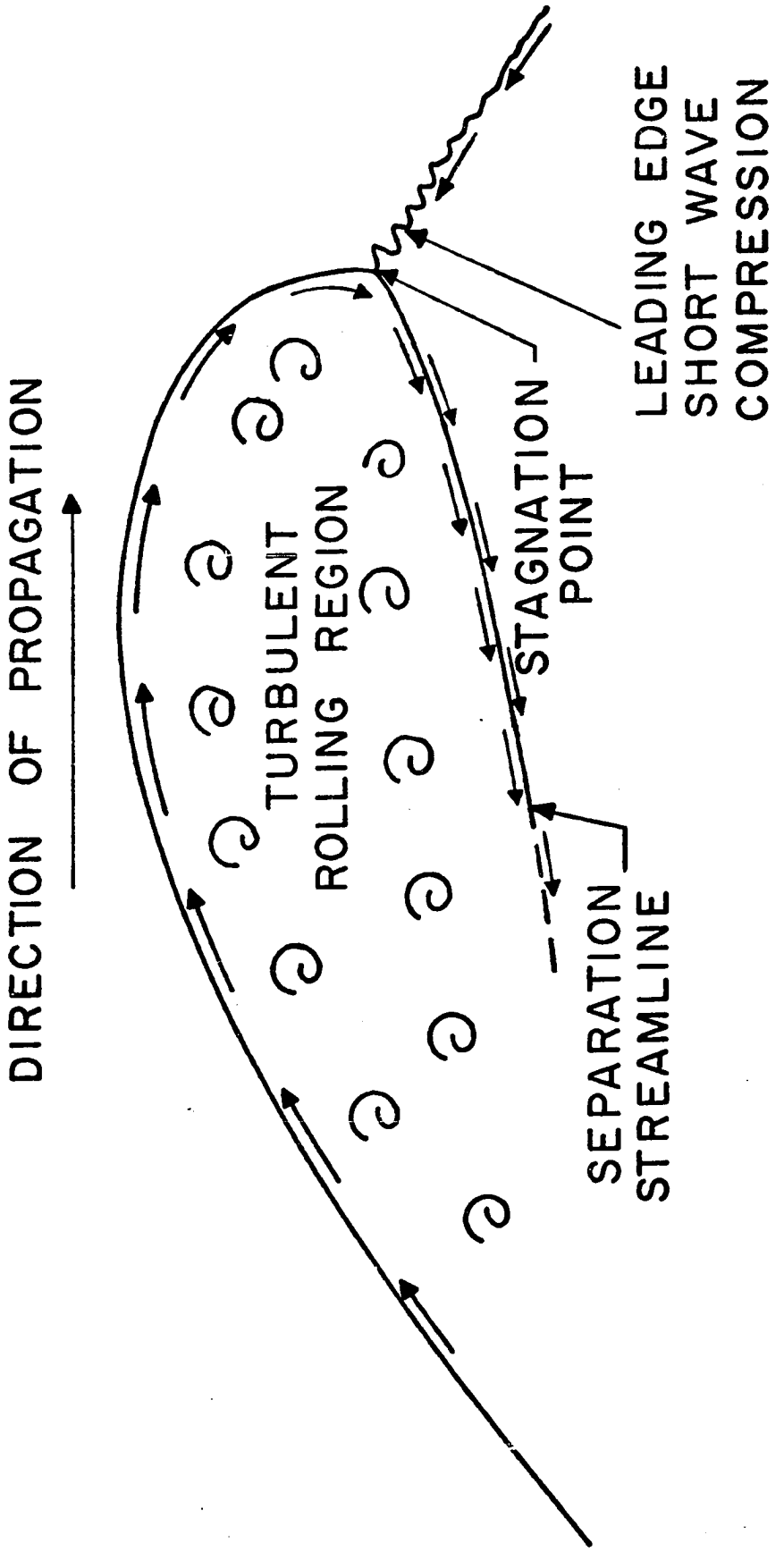

Fig. (23) Proposed model for rolling-breaking wave.

Reproduced with permission of the copyright owner. Further reproduction prohibited without permission.

KEY TO PLATES

In the strip chart recording shown in the lower half of each of the plates, the conversion factor between real time and the strip chart time (horizontal) axis is :

$$1 \text{ sec} \simeq 64 \text{ mm}$$

The vertical scale factor on the strip chart recordings is arbitrary. However, the same gain was maintained in all cases so that the relative wave height information is retained.

For each realization the spatial extent (L cm) of the photograph is reflected in an equivalent time interval T on the strip chart record by :

$$\frac{L}{T} \simeq C, \text{ the dominant phase speed.}$$

e.g. for the 1.7 Hz situations, $C \simeq 92$ cm/sec

1 sec = 64 mm on the strip chart $\simeq$ 92 cm in the photograph.

Hence the average extent of the photograph ($\pm$ 26 cm about the origin of 38 cm) is equivalent to approximately $\pm$ 20 mm diplacement about the reference epoch mark shown aligned with the 38 cm position.

Reproduced with permission of the copyright owner. Further reproduction prohibited without permission.

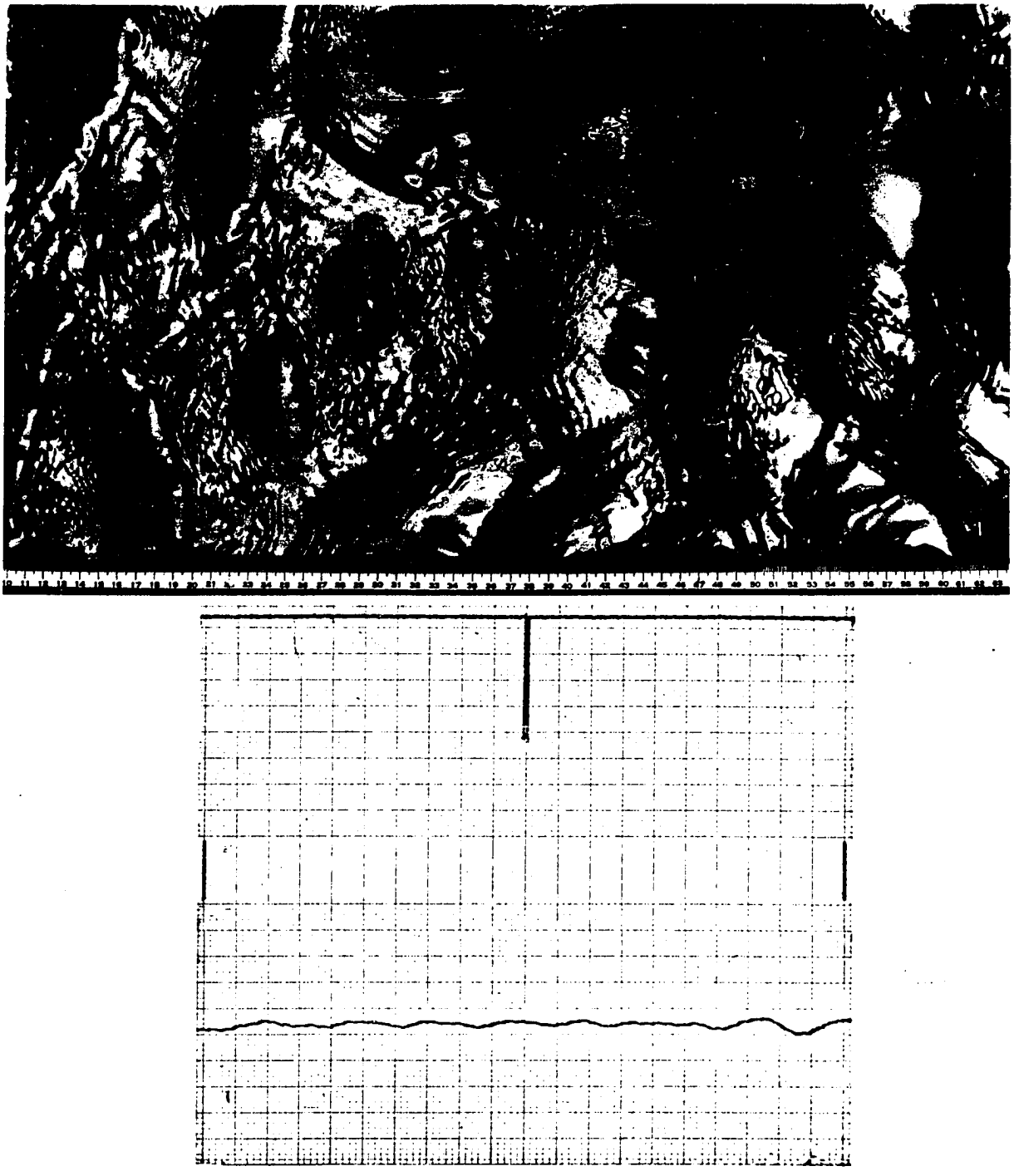

Plate 1. Surface structure for purely wind-driven situation at the first fetch (4.27 m).

Reproduced with permission of the copyright owner. Further reproduction prohibited without permission.

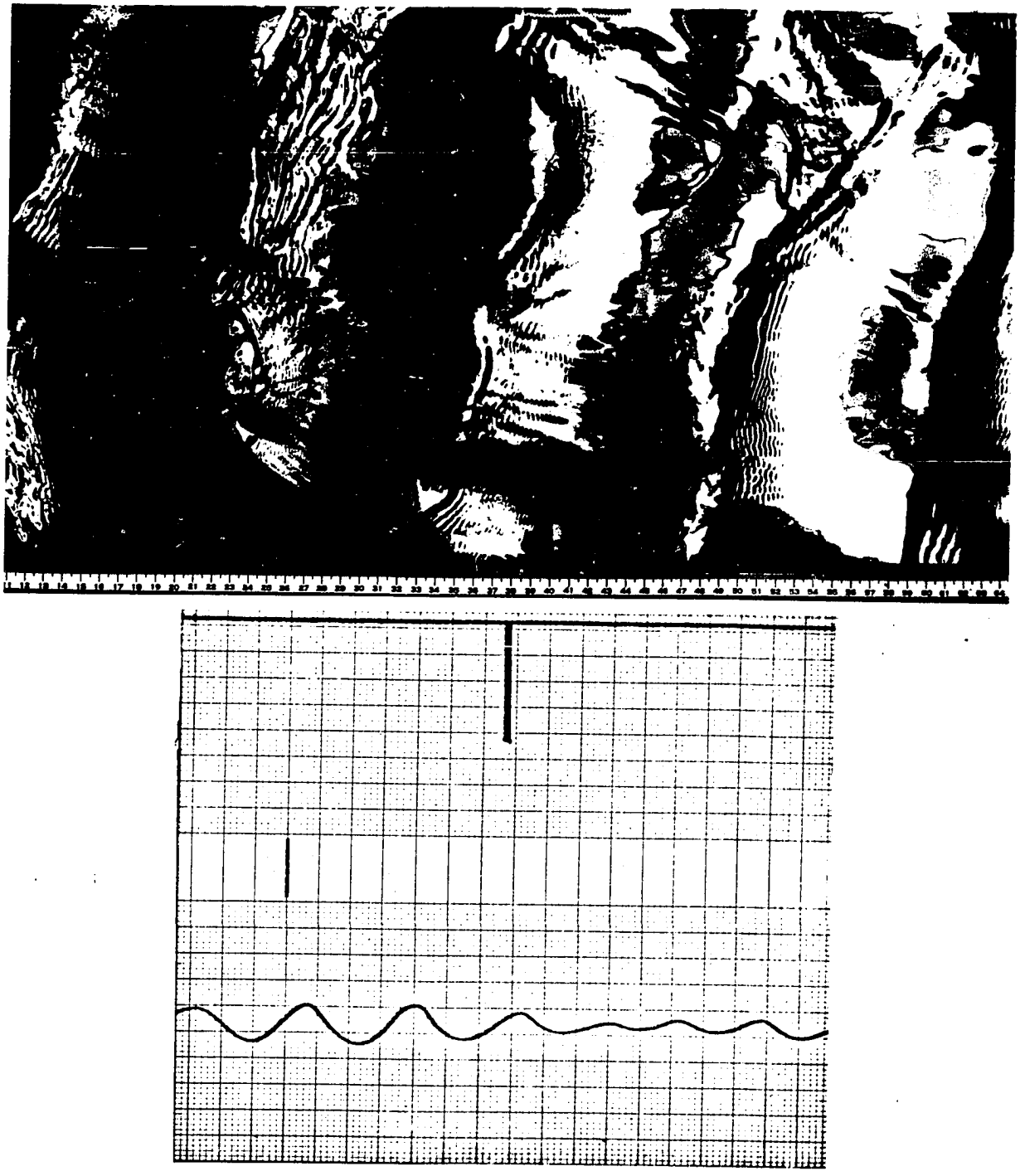

Plate 2. Surface structure for purely wind-driven situation at the second fetch (7.32 m).

Reproduced with permission of the copyright owner. Further reproduction prohibited without permission.

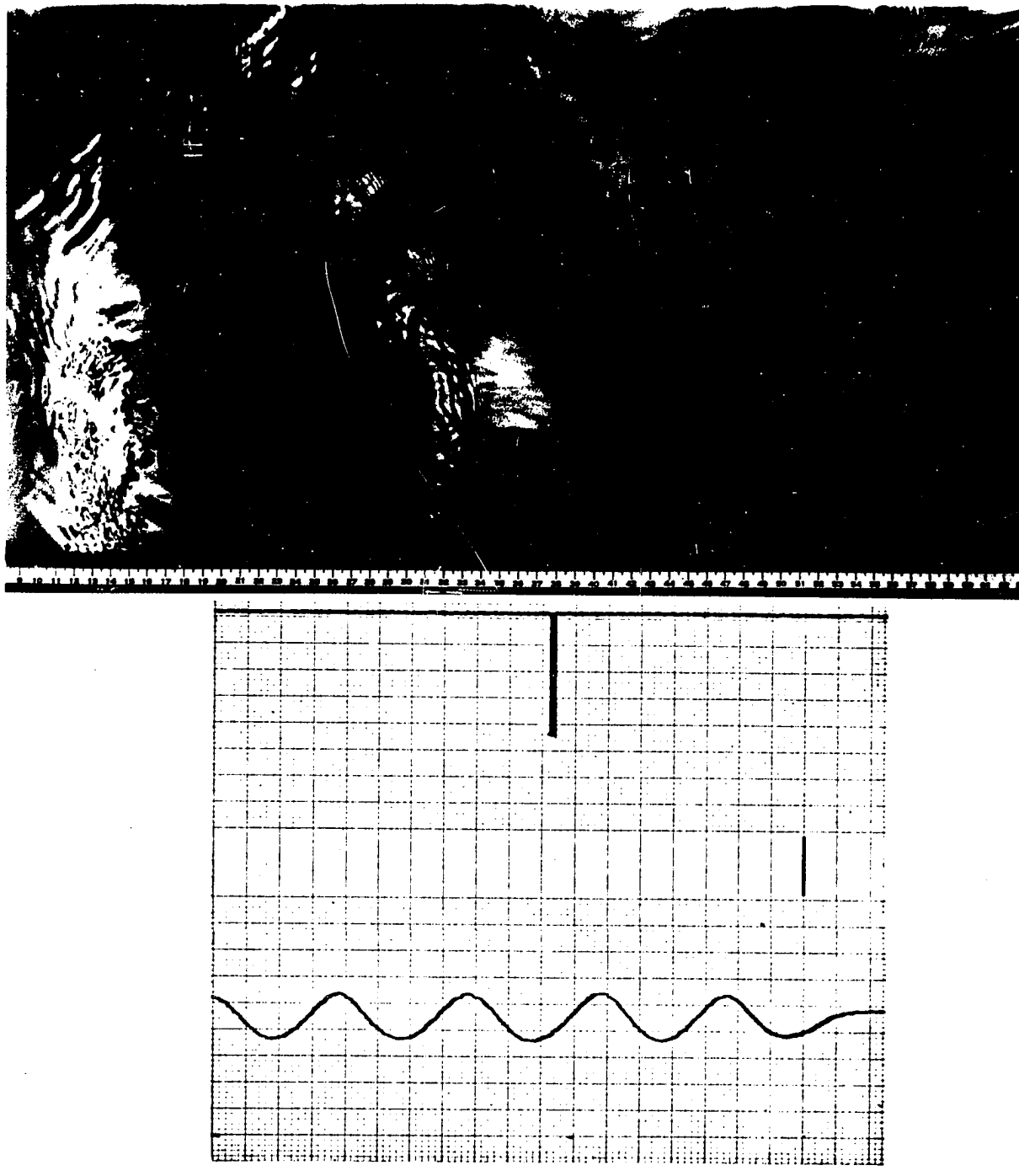

Plate 3. Surface structure for purely wind-driven situation at the third fetch (10.36 m).

Reproduced with permission of the copyright owner. Further reproduction prohibited without permission.

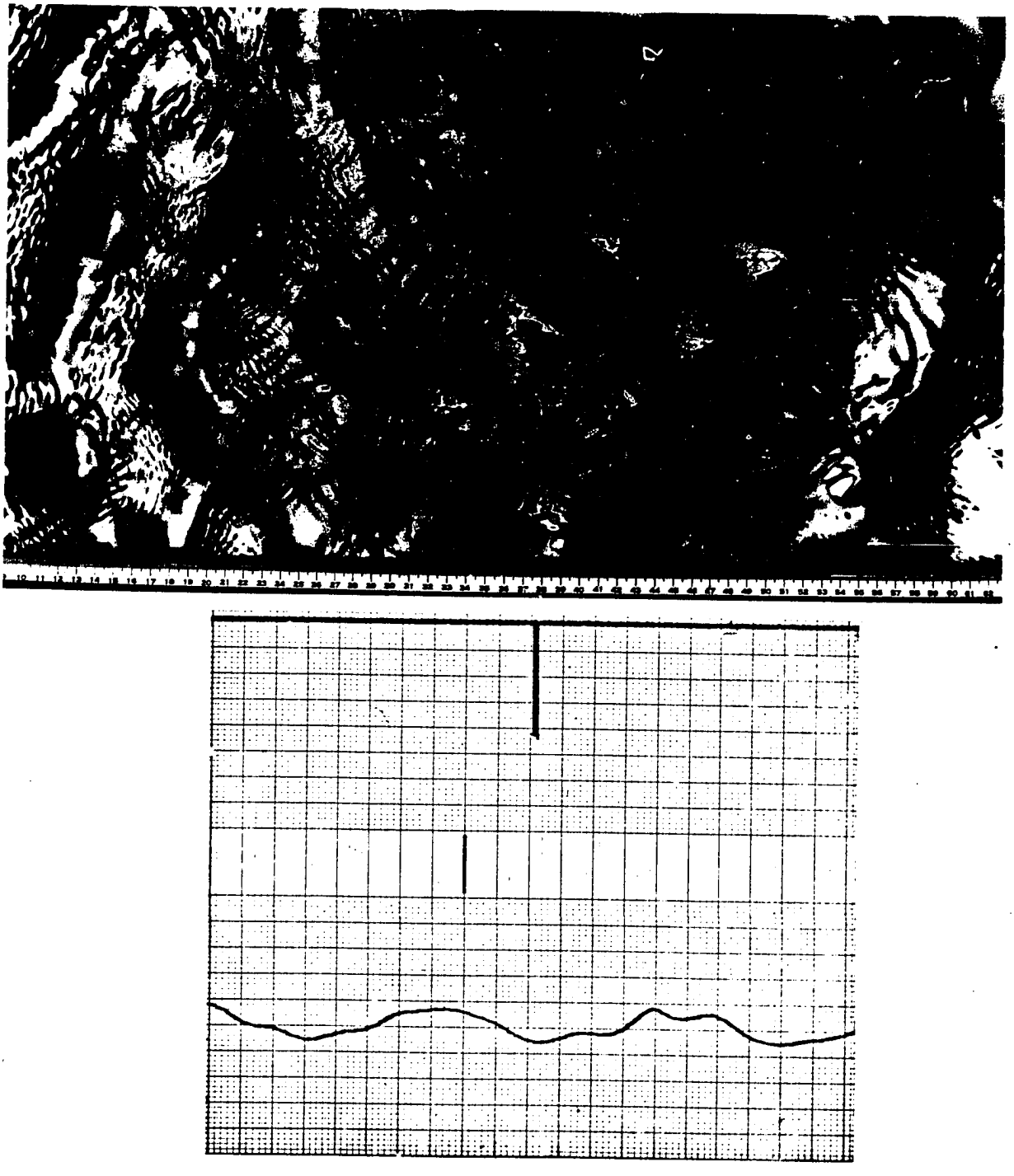

Plate 4. Surface structure with superposed 1.7 Hz mechanically-generated waves (slope $\sim$ 0.03) at the first fetch (4.27 m).

Reproduced with permission of the copyright owner. Further reproduction prohibited without permission.

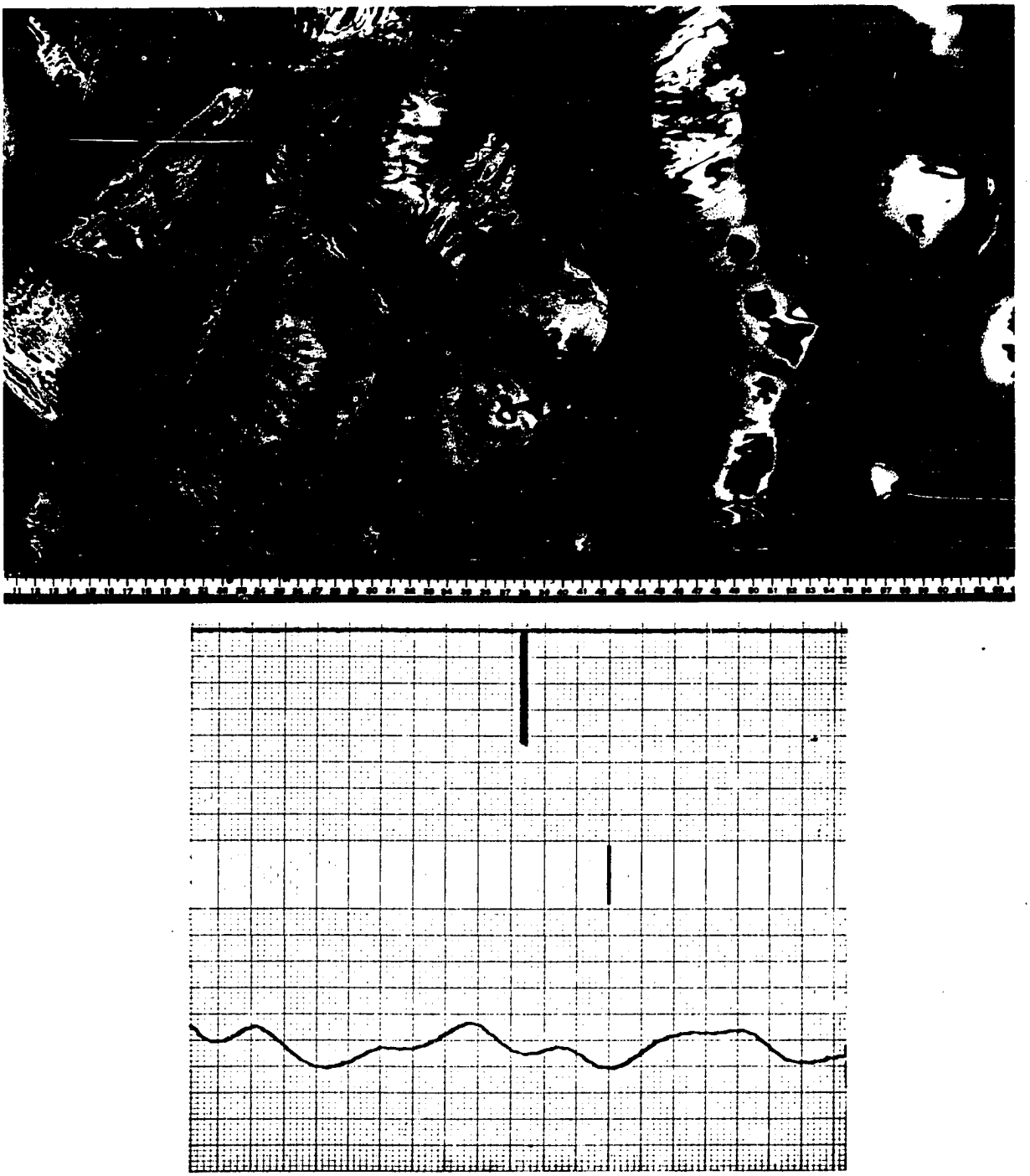

Plate 5. Surface structure with superposed 1.7 Hz mechanically-generated waves (slope $\sim$ 0.03) at the second fetch (7.32 m).

Reproduced with permission of the copyright owner. Further reproduction prohibited without permission.

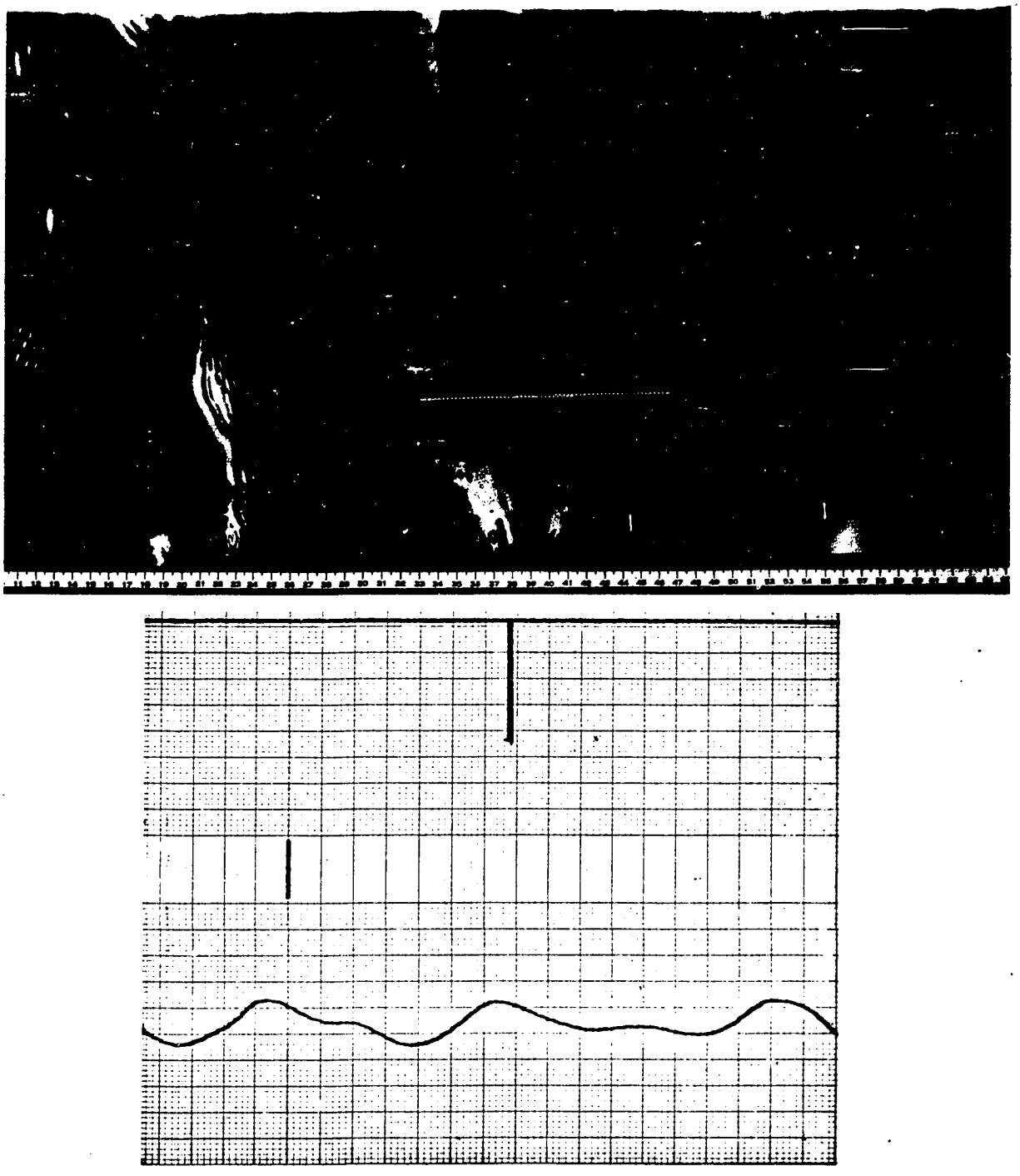

Plate 6. Surface structure with superposed 1.7 Hz mechanically-generated waves (slope $\sim$ 0.03) at the third fetch (10.36 m).

Reproduced with permission of the copyright owner. Further reproduction prohibited without permission.

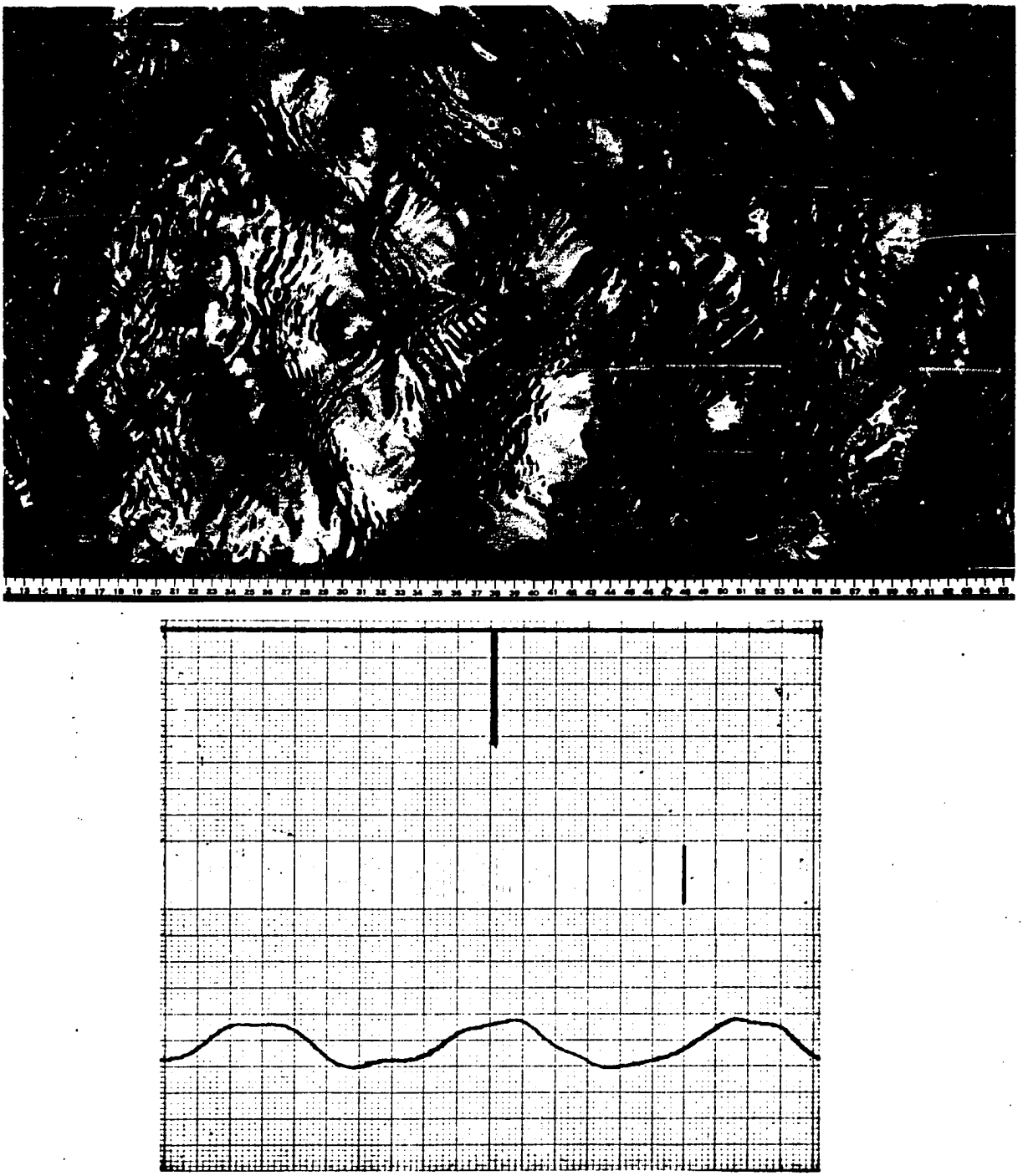

Plate 7. Surface structure with superposed 1.7 Hz mechanically-generated waves (slope $\sim$ 0.06) at the first fetch (4.27 m).

Reproduced with permission of the copyright owner. Further reproduction prohibited without permission.

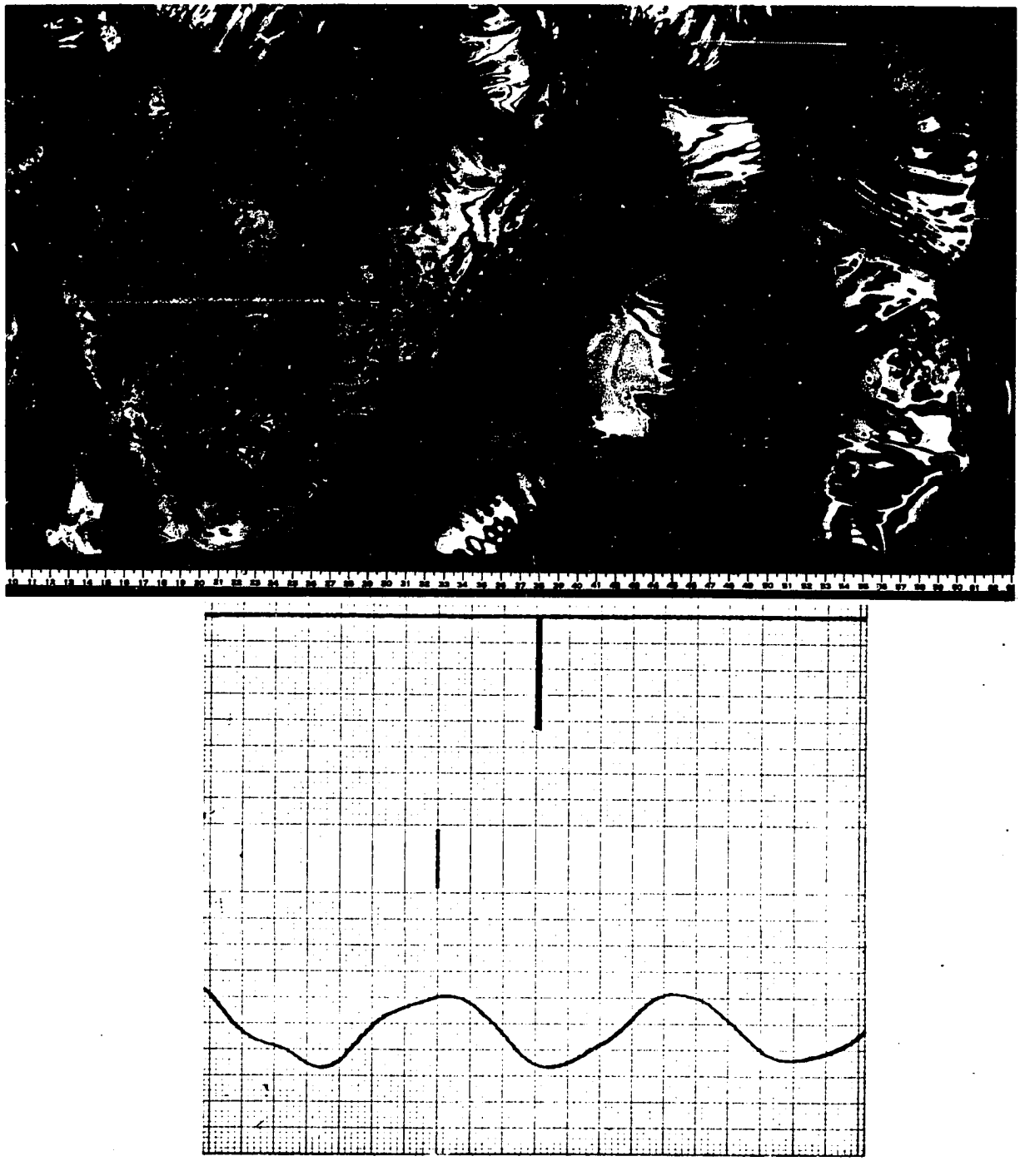

Plate 8. Surface structure with superposed 1.7 Hz mechanically-generated waves (slope $\sim$ 0.06) at the second fetch (7.32 m).

Reproduced with permission of the copyright owner. Further reproduction prohibited without permission.

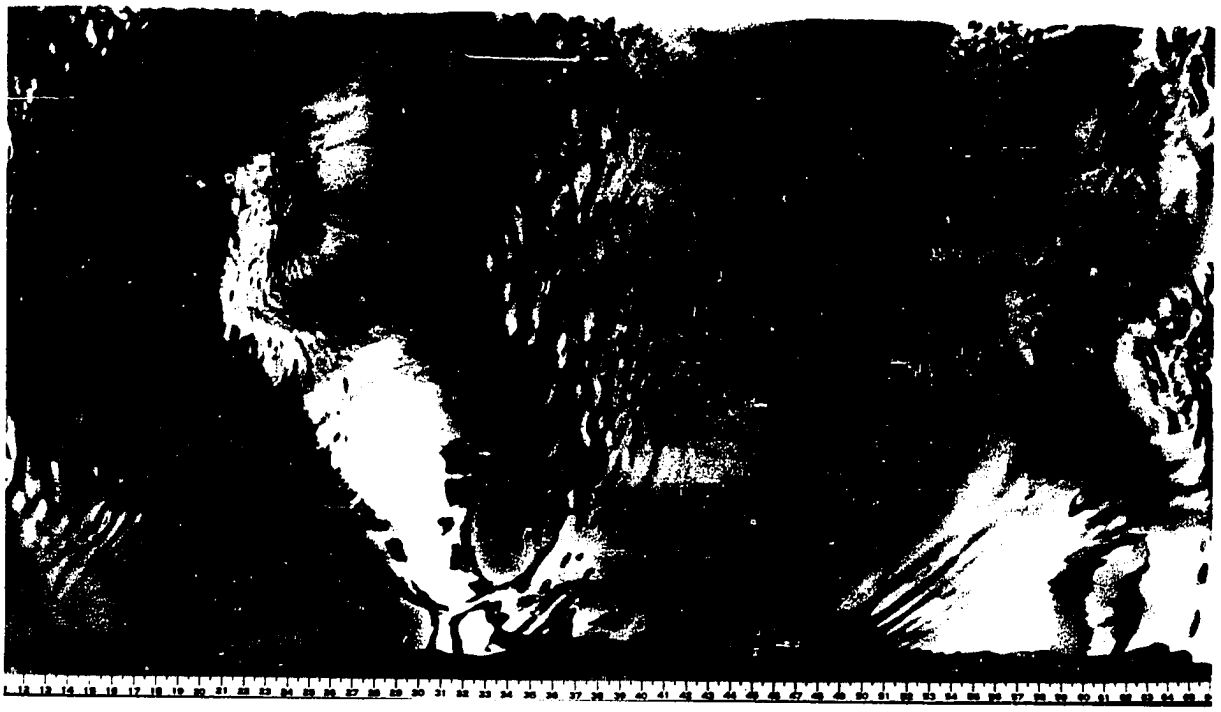

Plate 9. Surface structure with superposed 1.7 Hz mechanically-generated waves (slope $\sim$ 0.06) at the third fetch (10.36 m).

Reproduced with permission of the copyright owner. Further reproduction prohibited without permission.

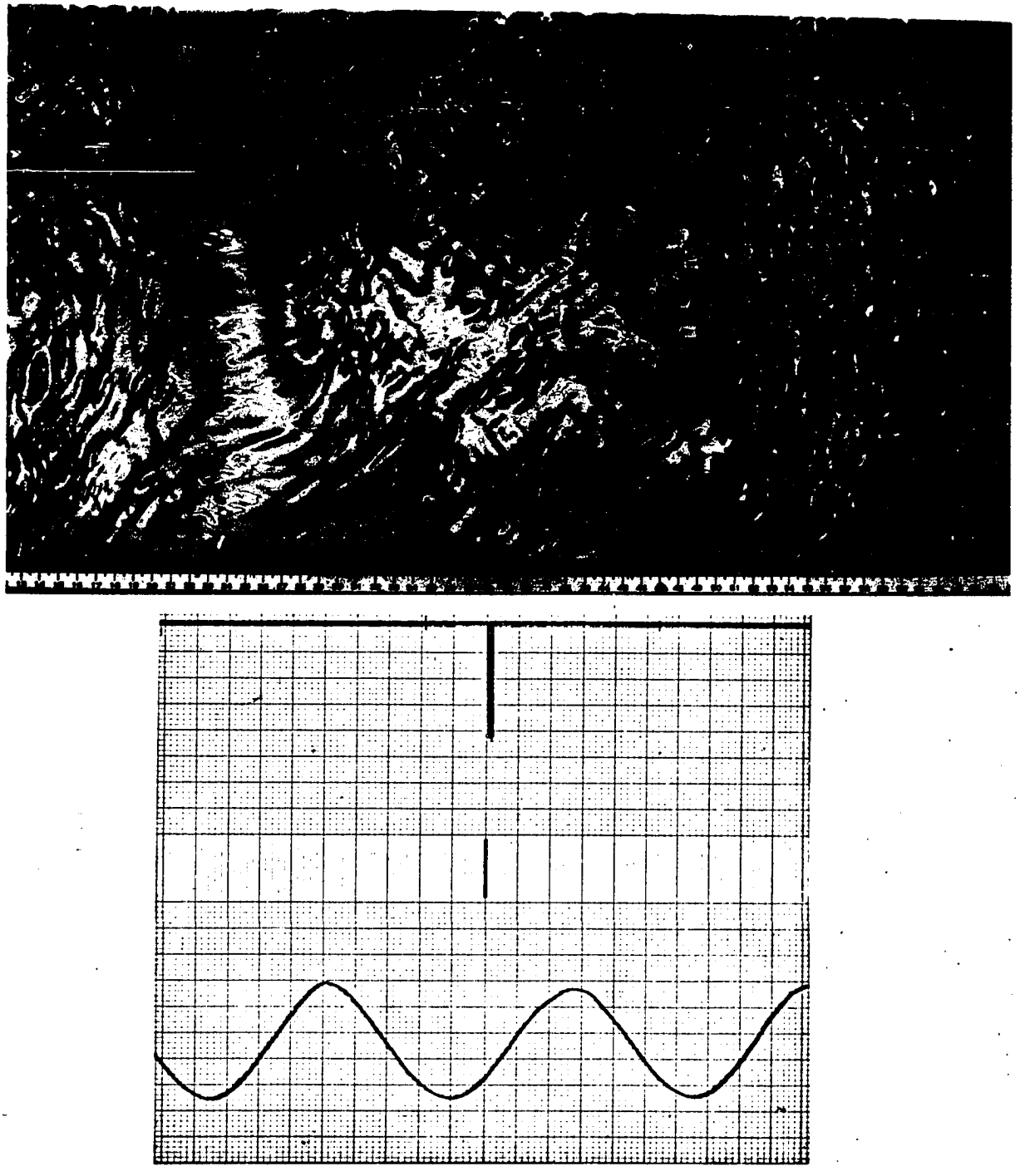

Plate 10. Surface structure with superposed 1.7 Hz mechanically-generated waves (slope ~ 0.175) at the first fetch (4.27 m).

Reproduced with permission of the copyright owner. Further reproduction prohibited without permission.

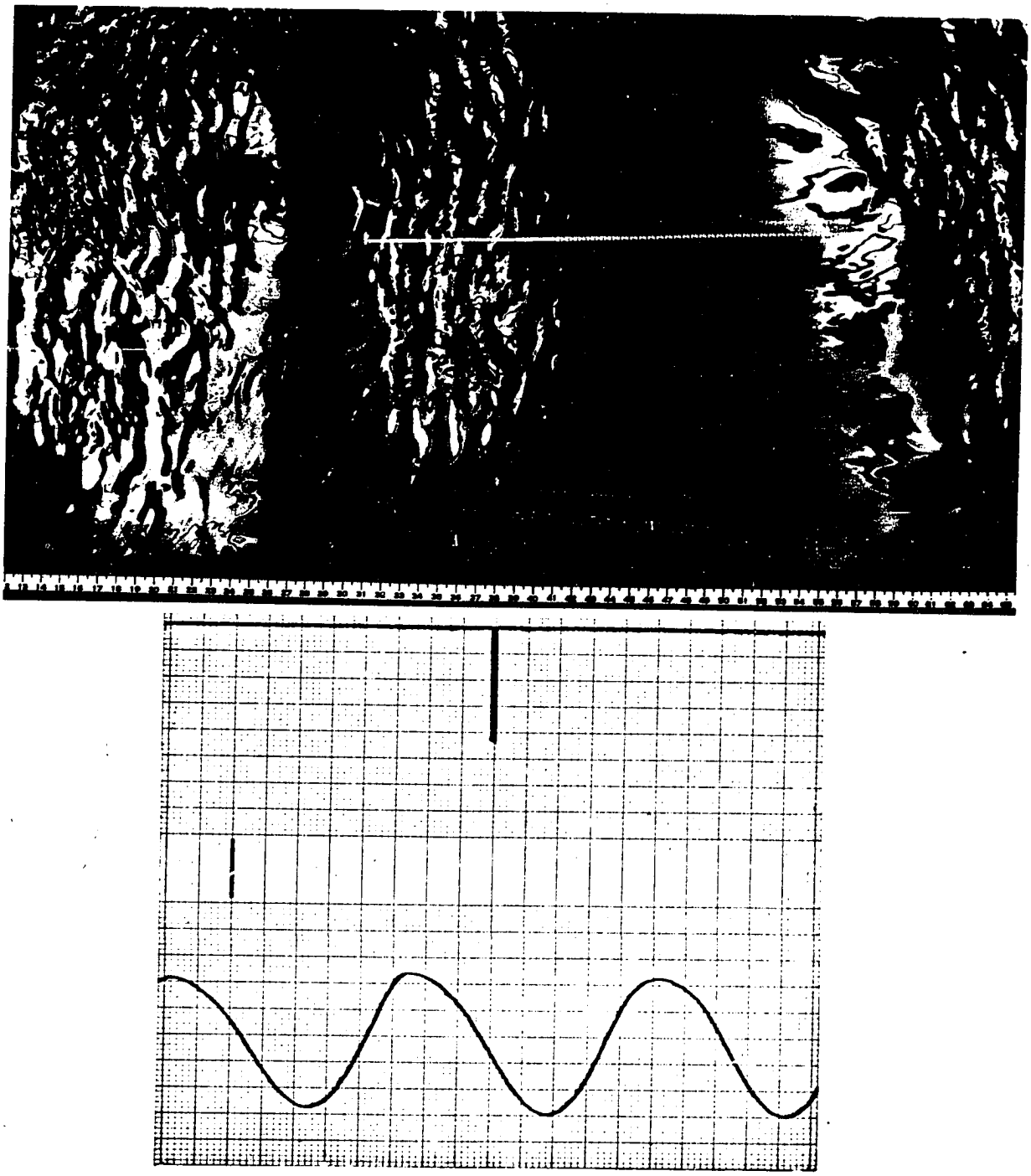

Plate 11. Surface structure with superposed 1.7 Hz mechanically-generated waves (slope $\sim$ 0.175) at the second fetch (7.32 m).

Reproduced with permission of the copyright owner. Further reproduction prohibited without permission.

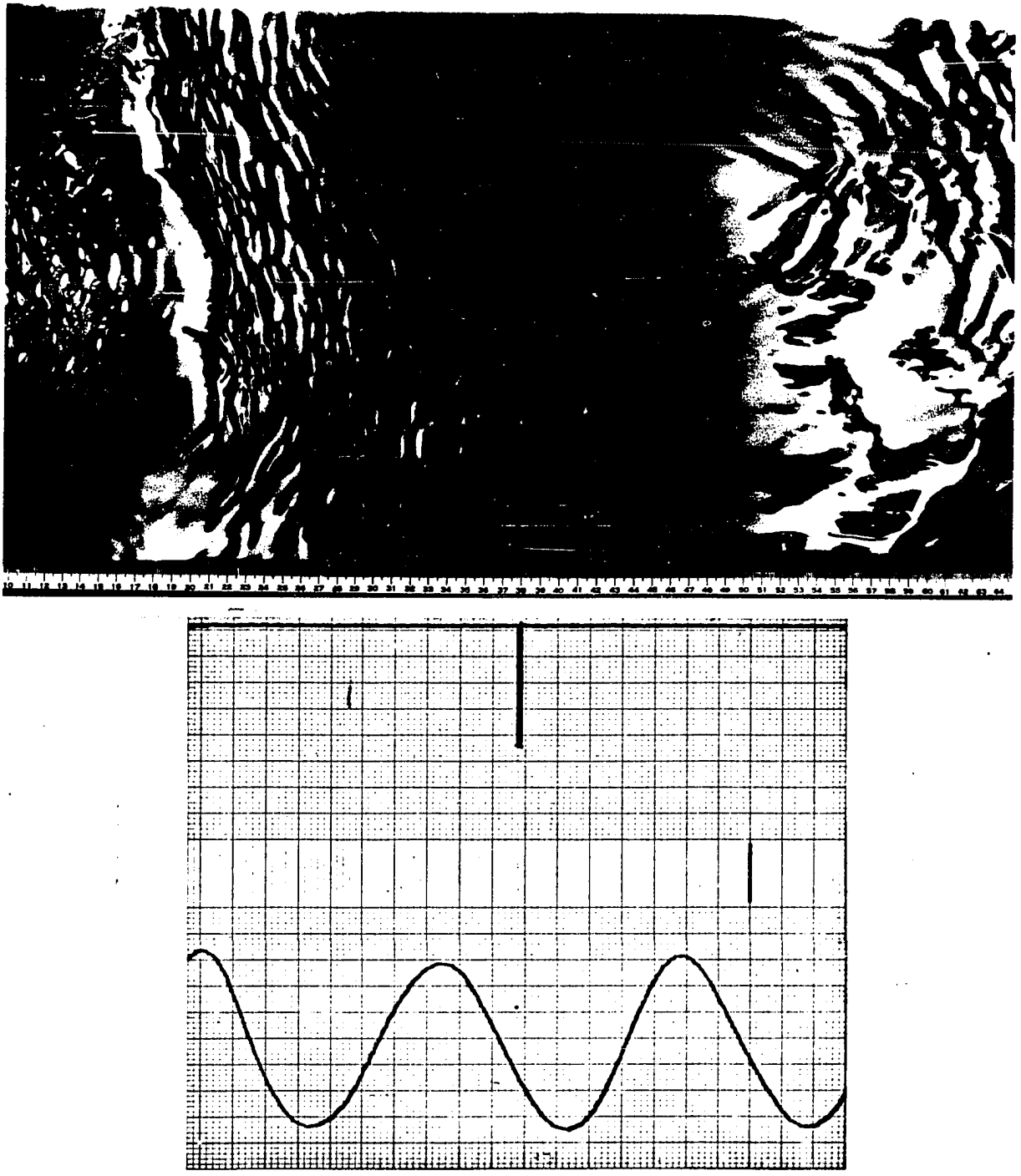

Plate 12. Surface structure with superposed 1.7 Hz mechanically-generated waves (slope $\sim$ 0.175) at the third fetch (10.36 m).

Reproduced with permission of the copyright owner. Further reproduction prohibited without permission.

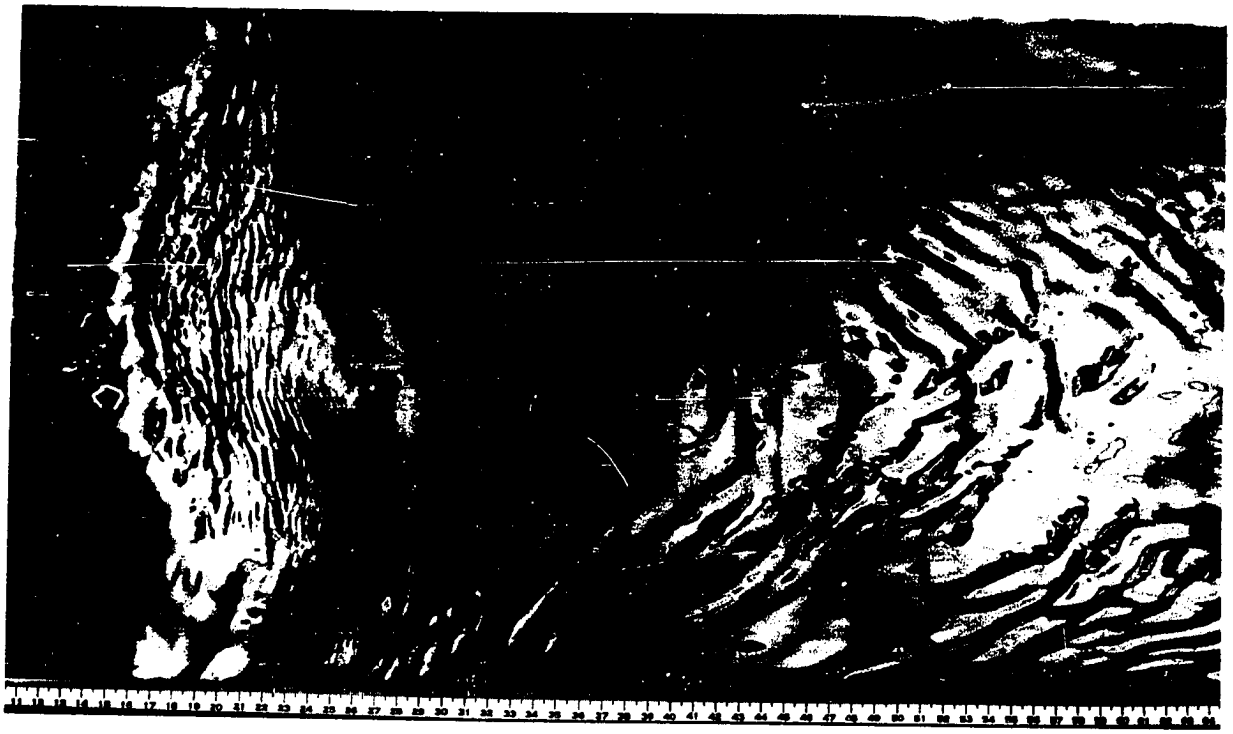

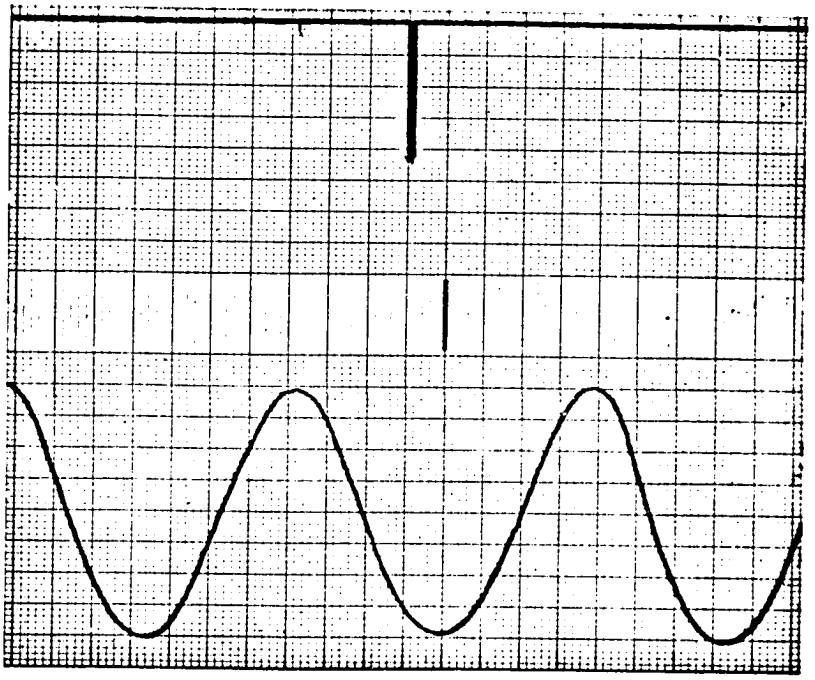

Plate 13. Surface structure with superposed 1.7 Hz mechanically-generated waves (slope $\sim$ 0.29) at the first fetch (4.27 m).

Reproduced with permission of the copyright owner. Further reproduction prohibited without permission.

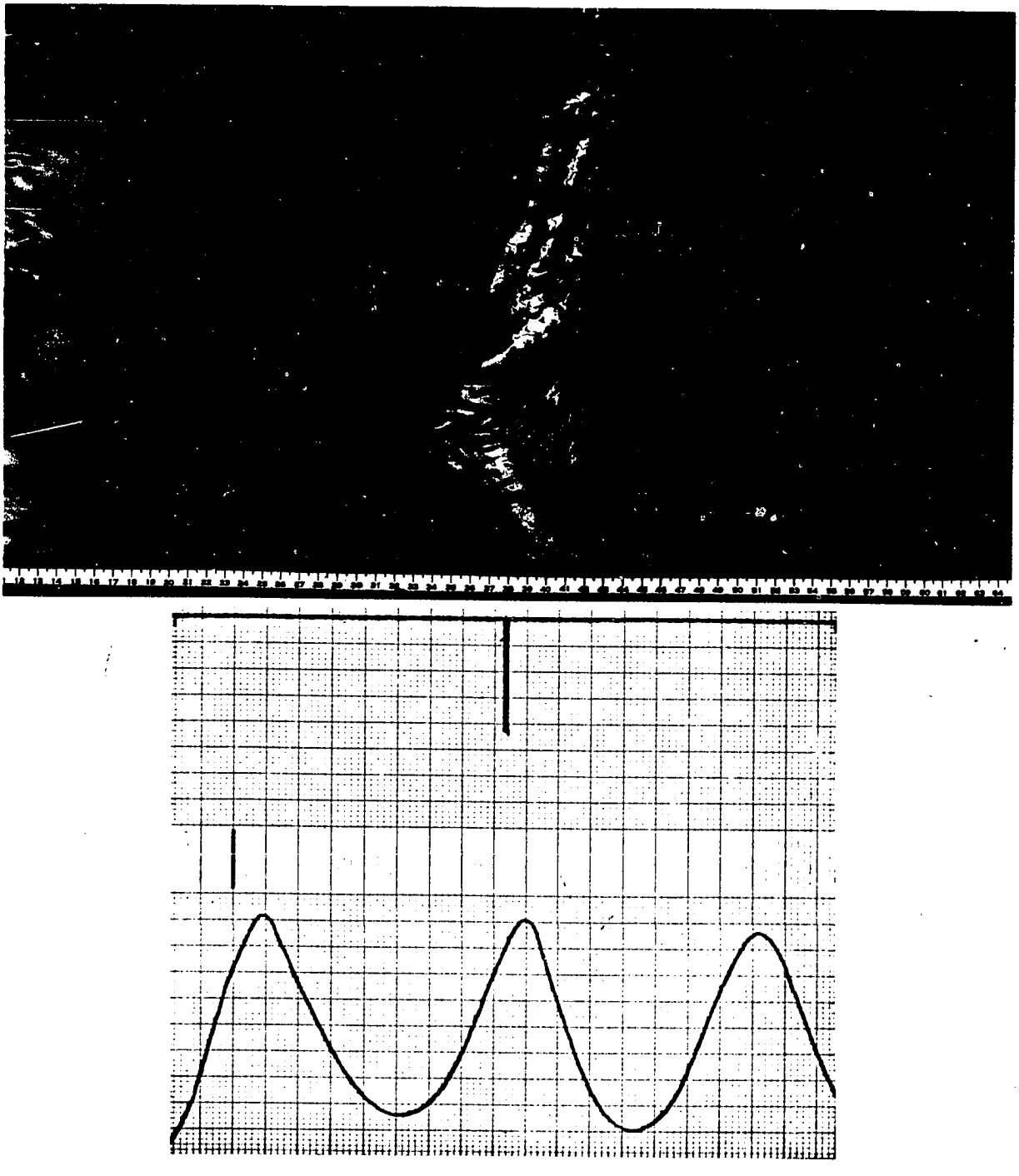

Plate 14. Surface structure with superposed 1.7 Hz mechanically-generated waves (slope $\sim$ 0.29) at the second fetch (7.32 m).

Reproduced with permission of the copyright owner. Further reproduction prohibited without permission.

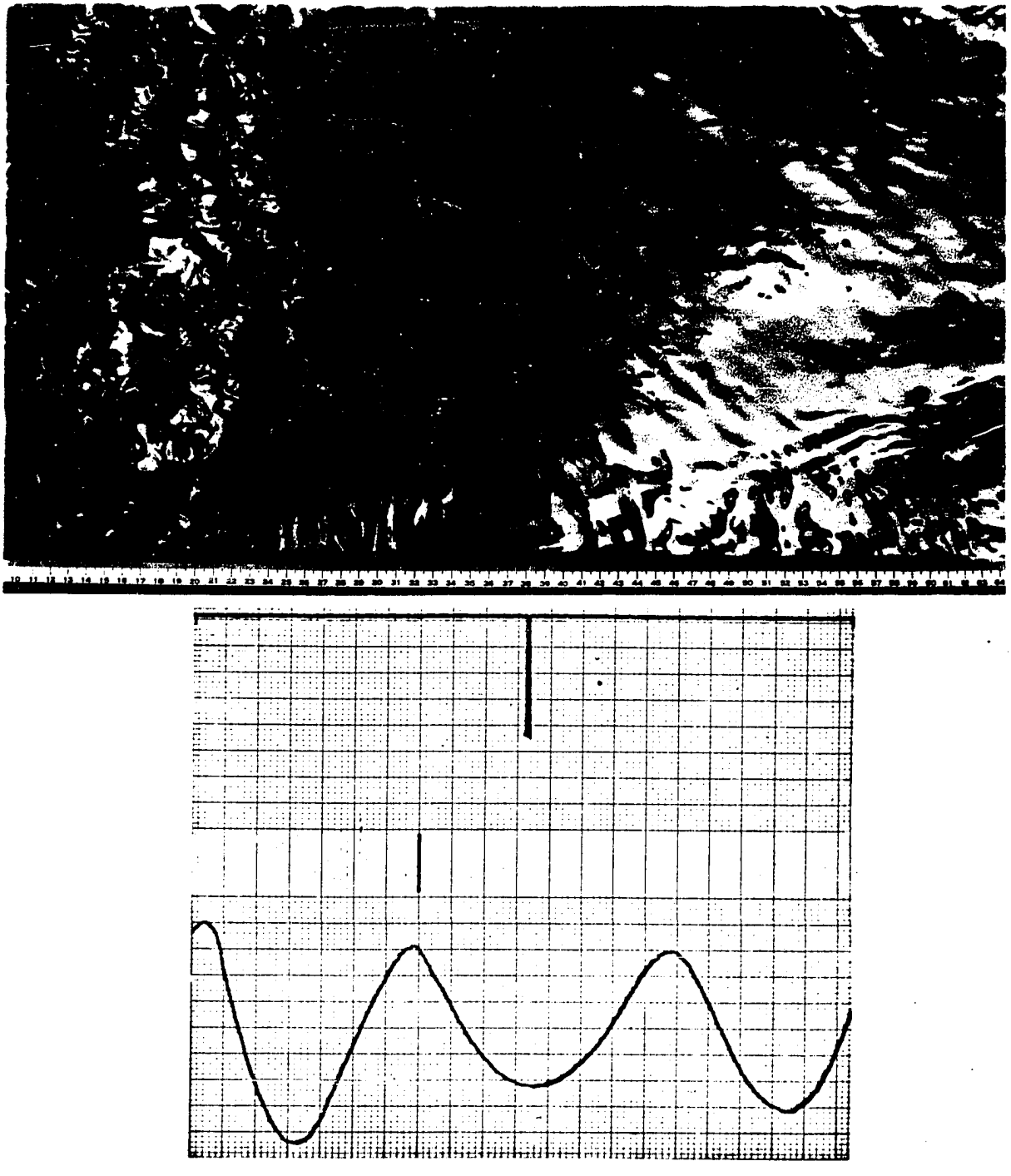

Plate 15. Surface structure with superposed 1.7 Hz mechanically-generated waves (slope $\sim$ 0.29) at the third fetch (10.36 m).

Reproduced with permission of the copyright owner. Further reproduction prohibited without permission.

VITA

The author was born January 3, 1945 in Sydney, Australia. He attended the Sydney Boys' High School and the University of Sydney. He graduated in 1965 with a Bachelor of Engineering degree with First Class Honors and was awarded the University Medal in Mechanical Engineering. In 1967 he received a Master of Engineering Science degree from the same university. He entered The Johns Hopkins University in September, 1967 in the Department of Mechanics where he also worked as a part-time Research Assistant on wind-wave generation experiments. In 1971, he transferred to the Department of Earth and Planetary Sciences where he completed his dissertation under the supervision of Professor O.M. Phillips.

Reproduced with permission of the copyright owner. Further reproduction prohibited without permission.